N° Ordre...../FS/UMBB/2024

**REPUBLIQUE ALGERIENNE DEMOCRATIQUE ET POPULAIRE**
**MINISTERE DE L'ENSEIGNEMENT SUPERIEUR ET DE LA RECHERCHE SCIENTIFIQUE**
**UNIVERSITE M'HAMED BOUGARA-BOUMERDES**


Faculté des **S**ciences

# Thèse de Doctorat

Présentée par

**Mr. NAAS Lazhari-ayoub**

En vue de l'obtention du Diplôme de Doctorat 3ème cycle (LMD)

Filière : **Physique**

Option : **Physique de la Matière Condensée**

---

## Elaboration et caractérisation des couches minces de $TiO_2$ dopées par l'azote pour application en photo-catalyse

---

Soutenue publiquement le 03/07/2024 devant le jury composé de :

| | | | | | |
|---|---|---|---|---|---|
| **Mme.** | **DOKHAN** | **Nahed** | **Professeur** | **UMBB** | **Présidente** |
| **Mr.** | **MAACHE** | **Mostefa** | **Professeur** | **Université de Djelfa** | **Examinateur** |
| **Mr.** | **MEGLALI** | **Omar** | **Professeur** | **Université de M'sila** | **Examinateur** |
| **Mme.** | **NEHAOUA** | **Nadia** | **MCA** | **UMBB** | **Examinatrice** |
| **Mr.** | **BOUAOUINA** | **Boudjemaa** | **MCA** | **UMBB** | **Directeur de thèse** |
| **Mr.** | **ABAIDIA** | **Saddik Elhak** | **Professeur** | **UMBB** | **Co-Directeur de thèse** |

Année Universitaire : **2023/2024**

Order N°...../FS/UMBB/2024

**DEMOCRATIC AND POPULAR REPUBLIC OF ALGERIA**
**MINISTRY OF HIGHER EDUCATION AND SCIENTIFIC RESEARCH**
**M'HAMED BOUGARA UNIVERSITY -BOUMERDES**


**F**aculty of **S**ciences

# Doctoral Thesis

Presented by

**Mr. NAAS Lazhari-ayoub**

In order to obtain the Doctorate Degree of the 3rd Cycle (LMD)

Field: **Physics**
Option: **Condensed Matter Physics**

---

## Elaboration and characterization of Nitrogen-doped $TiO_2$ thin films for photocatalysis application

---

Publicly defended on 03/07/2024 in front of the jury composed of:

| | | | | | |
|---|---|---|---|---|---|
| **Mme.** | **DOKHAN** | **Nahed** | **Professor** | **UMBB** | **President** |
| **Mr.** | **MAACHE** | **Mostefa** | **Professor** | **University of Djelfa** | **Examiner** |
| **Mr.** | **MEGLALI** | **Omar** | **Professor** | **University of M'sila** | **Examiner** |
| **Mme.** | **NEHAOUA** | **Nadia** | **MCA** | **UMBB** | **Examiner** |
| **Mr.** | **BOUAOUINA** | **Boudjemaa** | **MCA** | **UMBB** | **Thesis Supervisor** |
| **Mr.** | **ABAIDIA** | **Saddik Elhak** | **Professor** | **UMBB** | **Thesis Co-supervisor** |

Academic Year: **2023/2024**

# Dedication

*I dedicate this work to:*

*My dear parents, my grandmother, and my uncle. My brothers, and sister.*
*My Wife,*
*My Son,*
*All my family.*
*All my friends.*

*Everyone who has helped me to complete this thesis.*

*All the teachers who have teach me, because if we are here today, it is thanks to all of you, so a big thank you to you all.*

**Ayoub**

# Acknowledgement

الحمد والشكر لله الذي رزقني نعمة العلم و فضلني على كثير من مخلوقاته و الصلاة و السلام على سيدنا محمد (صلى الله عليه و سلم) خير و أفضل العلماء.

The present work was carried out within the laboratory "Laboratoire Revêtement, Matériaux, et Environnement" at the Faculty of Sciences of M'Hamad Bougara University of Boumerdes.

At the end of writing my thesis, I extend warm thanks to my thesis supervisor, Mr. Boudjemaa BOUAOUINA, for the attention he has given to my work, for his wise advice, and his attentive listening which have been decisive for the successful completion of this thesis. His energy and confidence have been motivating factors for me, and I have greatly honored and enjoyed working with him.

I warmly thank Mr. Saddik Elhak ABAIDIA, my thesis co-supervisor and the director of the laboratory "Laboratoire Revêtement, Matériaux, et Environnement", for the nonstop experimental and knowledge support and I have greatly honored and enjoyed working with him.

I also express my gratitude in advance to the esteemed members of the jury, Prof. MAACHE Mostefa, Prof. MEGLALI Omar, and Mme. NEHAOUA Nadia, and the esteemed president of the jury, Prof. DOKHAN Nahed, for their advice

and constructive criticism, and for taking the time to read this work and to travel all this distance.

I thank my dear father and say to him, "You are a true school of life, I never stop learning from you every day."

I thank my dear mother and say to her, "It is thanks to you that I am here today."

I thank my dear supportive wife and my son.

I also thank all my family and my friends.

# Abstract

This thesis work investigates the structural, optical, and photocatalytic properties of nitrogen-doped titanium dioxide ($TiO_2$) thin films synthesized via the sol–gel method. Nitrogen-doped $TiO_2$ thin films are deposited using three experimental approaches: adding nitrogen source precursor in the $TiO_2$ deposition solution, $N_2$ plasma treatment, and TiN layer coupling. X-ray diffraction analysis reveals exclusive crystallization in the anatase structure for both pure and nitrogen-doped $TiO_2$ thin layers. UV-visible analysis shows transparency in the visible region but opacity in the UV region for all thin films. Band gap energy calculations indicate a decrease upon nitrogen doping, confirming successful incorporation. Atomic force microscopy reveals nitrogen doping influences surface morphology and roughness. Nitrogen plasma surface treatment exhibits slight photocatalytic activity enhancement, while TiN layer coupling significantly improves photocatalytic activity. These findings underscore the potential of nitrogen-doped $TiO_2$ layers for enhanced photocatalytic efficiency, addressing environmental challenges posed by escalating pollution rates.



**Key-words:** $TiO_2$ thin films; sol-gel; plasma treatment; nitrogen doping; Photocatalysis.



# Résumé

Ce travail de thèse explore les propriétés structurales, optiques et photocatalytique des couches minces de dioxyde de titane ($TiO_2$) dopés à l'azote, synthétisés par la méthode sol–gel. Les couches minces de $TiO_2$ dopés à l'azote sont déposées selon trois approches expérimentales : L'ajout d'un précurseur de source d'azote dans la solution de dépôt de $TiO_2$, traitement au plasma $N_2$ et couplage une couche de TiN. L'analyse par diffraction des rayons X révèle une cristallisation exclusive dans la structure de l'anatase pour les couches minces de $TiO_2$, qu'elles soient pures ou dopées à l'azote. L'analyse UV-visible montre une transparence dans la région visible mais une opacité dans la région UV pour tous les couches minces. Les calculs de l'énergie de bande interdite indiquent une diminution lors du dopage à l'azote, confirmant une incorporation réussie dans la structure. La microscopie à force atomique révèle que le dopage à l'azote influence la morphologie de la surface et de la rugosité. Le traitement de la surface au plasma d'azote présente une légère amélioration dans l'activité photocatalytique, tandis que le couplage de la couche de TiN améliore significativement l'activité photocatalytique. Ces résultats mettent en évidence le potentiel

des couches de $TiO_2$ dopées à l'azote pour une efficacité photocatalytique accrue, permettant de relever les défis environnementaux liés à l'augmentation des taux de pollution.

**Mots-clés :** Couches minces de $TiO_2$ ; méthode sol-gel ; traitement au plasma ; dopage à l'azote ; photocatalyse.

# الملخص

**تستكشف هذه الأطروحة الخصائص البنيوية والبصرية والتحفيز الضوئي لأغشية رقيقة من ثاني أكسيد التيتانيوم (TiO2) المطعمة بالنيتروجين، والتي تم تحضيرها باستخدام طريقة السائل–هلام. تم ترسيب الأغشية الرقيقة من TiO2 المطعمة بالنيتروجين باستخدام ثلاثة أساليب تجريبية: إضافة مادة منتجة للنيتروجين في محلول الترسيب لـTiO2 ، ومعالجة بالبلازماN2 ، وربط طبقةTiN . أظهر تحليل الأشعة السينية تبلوراً حصرياً في الهيكل الأناتازي للأغشية الرقيقة منTiO2 ، سواء كانت نقية أم مطعمة بالنيتروجين. وأوضح التحليل المرئي – فوق البنفسجي شفافية في المنطقة المرئية وعتامية في منطقة الأشعة فوق البنفسجية لجميع الأفلام الرقيقة. وأظهرت حسابات طاقة الفجوة النطاقية انخفاضاً عند التطعيم بالنيتروجين، مما يؤكد نجاح عملية التطعيم .بيّن مجهر القوة الذرية أن التطعيم بالنيتروجين يؤثر على سطح الأغشية الرقيقة. وأظهرت معالجة البلازما النيتروجينية تحسناً طفيفاً في النشاط التحفيزي الضوئي، في حين أن ربط طبقة TiN ساهم بشكل كبير في تعزيز النشاط التحفيزي الضوئي .تسلط النتائج المحصلة الضوء على الإمكانيات الهائلة للأغشية المطعمة بالنيتروجين لتعزيز الكفاءة التحفيزية الضوئية، وبالتالي مواجهة التحديات البيئية المتزايدة المتعلقة بارتفاع معدلات التلوث.**

**<u>الكلمات الدالة:</u> أفلام رقيقة $TiO_2$؛ طريقة السائل–هلام؛ المعالجة بالبلازما؛ تطعيم النيتروجين؛ التحفيز الضوئي.**

# Table of contents

# List of Abbreviations

| Abbreviation | Definition |
|---|---|
| AFM | Atomic Force Microscopy |
| AOD | Advanced Oxidation Technique |
| CCD | charged-coupled device |
| DC | Direct current |
| DFT | density functional theory |
| DOS | density of states |
| EDX | Energy-dispersive X-ray |
| EPR | electron paramagnetic resonance |
| ESCA | Electron Spectroscopy for Chemical Analysis |
| FWHM | full width at half maxima of the peak |
| GLAD | Glancing angle deposition |
| HF | hydrogen fluoride |
| JCPDS | Joint Committee Power Diffraction Standards |
| MB | Methylene blue |
| pH | potential of hydrogen |
| PL | Photoluminescence |
| PVD | Physical vapor deposition |
| RMS | Root Mean Square |
| ROS | Reactive oxygen species |
| SEM | scanning electron microscope |
| TEOT | Tetraethyl–Orthotitanate |
| TPOT | Tetrapropyl–Orthotitanate |
| UV | Ultra violet |
| UV-VIS | Ultraviolet-visible |
| XPS | X-ray photoelectron spectroscopy |
| XRD | X-ray diffraction |

# List of figures

# List of tables

# General Introduction

Modern technology has been significantly impacted by the utilization of thin films, which are essential in advanced applications across numerous fields; $TiO_2$ material in thin film form has emerged as the most commonly employed material in photocatalytic applications thanks to its various advantageous properties, such as high oxidizing energy, non-toxicity, low-cost, stability under light exposure, and widespread availability [1-3], As a result of these characteristics, Titanium dioxide has found various applications such as photocatalyst in water purification, coatings for self-cleaning windows [4, 5], antimicrobial agents [6], solar energy conversion [7], catalysts for environmental remediation, photochromic [8], optoelectronics devices [9], textiles, ceramic membrane [10], gas-sensing devices [11, 12], and water electrolysis for hydrogen production [13, 14].

Despite these unique characteristics, $TiO_2$ exhibits several deficiencies regarding some photoactive applications, due to its critical limitation to absorb visible light due to its wide optical bandgap ($E_g$ = 3.2 eV). This wide optical bandgap causes $TiO_2$ to primarily absorbing solar light in the UV (ultraviolet) range, which constitutes only 8% of the entire solar spectrum, whereas visible light comprises up to 47%[15].

Numerous methods have been explored to decrease the optical bandgap energy, one of which involves doping nitrogen atoms into the lattice of $TiO_2$ host materials [15-18]. Nitrogen doping has been found to effectively improve visible light photocatalytic activity. The underlying hypothesis for the effect of nitrogen atoms doping is the introduction of N2p energy states slightly above the valence band, making the band gap narrows, thus increasing the $TiO_2$'s absorption of visible light; Extensive research has been conducted thus far, and several strategies have been developed to dope nitrogen atoms into the $TiO_2$ lattice, including doping using physical vapor deposition (PVD) [19], annealing in ammonia gas [15, 20], ion implantation [21, 22]. $TiO_2$ sol-gel coating with nitrogen-containing precursors [23], and plasma treatment techniques [15, 24].

The objective of this thesis work is the deposition of thin films of nitrogen doped titanium dioxide by the sol-gel deposition technique for the $TiO_2$ thin films and different methods for the nitrogen doping. The impact of the different approaches for nitrogen doping to the structural, morphological, optical and photocatalytic properties of the $TiO_2$ thin films is also investigated.

This thesis contains five chapters:

- The first chapter serves as a literature review, focusing on the deposition technique and the physical properties of titanium dioxide. It also explores general concepts related to nitrogen doping in titanium dioxide and provides an overview of the principles of photocatalysis.
- Chapter two provides detailed descriptions of the experimental procedures used to prepare the $TiO_2$ thin films, along with a detailed description of the various characterization techniques employed throughout the study.
- Chapter three focuses on the effect of the nitrogen doping via nitrogen precursor solution (chemical process) and its influence on the physical and photocatalytic properties of $TiO_2$.
- Chapter four investigates the impact of $N_2$ plasma treatment on the physical and photocatalytic properties of $TiO_2$.
- Chapter five explores the effects of coupling a sub-layer of TiN on the $TiO_2$ film and its impact on physical and photocatalytic properties.

This manuscript ends with a conclusion in which we summarize the main results obtained and discuss future perspectives.

# Chapter I:
# *State of the art*

## 1. Introduction

This first chapter collects the literature review of the physical properties of titanium dioxide material along with the nitrogen doped $TiO_2$ material as well as its advantages and an overview on the adopted preparation methods, and the photocatalysis description.

## 2. Titanium dioxide

In 1791, William Gregor discovered titanium (Ti) material, a silver-colored transition metal; It is the seventh most abundant metal and ninth abundant element in the earth's crust [25]. Due to its low density and high strength, titanium is a strong and light metal. Titanium cannot be found as a pure metal in nature because of its strong affinity to carbon, oxygen, and nitrogen, making it hard to get in the pure form. In the early 1900s, titanium dioxide was first discovered, and the manufacture of white titanium for use as a pigment (in anatase phase) was first reported in France in 1923, where then soon replaced in the early 1930s the lithopone and toxic lead-based pigments [26].

Titanium dioxide, also known as titania, is a white inorganic compound consisting of one titanium atom and two oxygen atoms. Its chemical formula is $TiO_2$, and titanium dioxide belongs to the family of metal oxides. $TiO_2$ is very interesting for its many applications, especially for its high oxidation power, high stability and resistance to corrosion, availability, low-cost production, and ability to degrade a vast range of pollutants; It can also both scatter and absorb UV rays [27, 28]. $TiO_2$ semiconductor has a significant band gap energy ($E_g$=3.2 eV). It is widely used in environmental applications as a photocatalyst for oxidation reactions of organic compounds, thermal decomposition reactions of alcohol, photocatalytic decomposition of water to generate hydrogen, photovoltaic cells, etc. [29].

The challenges with using $TiO_2$ in powder form include separation/filtration issues, difficulties in continuous flow systems, and particle aggregation, especially at high concentrations. To address these, there has been a shift towards producing $TiO_2$ thin films, although they generally exhibit lower photocatalytic activity compared to powders due to the surface vs. volume phenomenon [30, 31]. Structural changes between anatase and rutile phases, and microstrain, depend on $TiO_2$ morphology and substrate nature [32, 33]. Supporting substrates are crucial for stabilizing anatase at high temperatures (>800 °C) compared to powders, which may convert to rutile at lower temperatures (500-600 °C)[30].

## 2.1. Structural properties

Titanium dioxide ($TiO_2$) semiconductor is the most important photocatalytic material, it crystalizes in several crystalline structures depending on the processing temperature; the main and most common polymorphs are rutile and anatase. Anatase is commonly obtained at film deposition temperatures in the range 350-700 °C, while higher temperatures occur in the growth of rutile phase. These polymorphs exhibit different properties and, consequently, different photocatalytic performances.

### 2.1.1. Rutile phase

The rutile structure of $TiO_2$ is a thermodynamically stable phase that exhibits a very high refractive index and ultraviolet absorption; due to these properties, it has been widely applied in pigments and opacified materials.

The rutile phase crystallizes in a tetragonal structure with space group P42/mnm (136). The elementary cell of rutile is quadratic (a = b = 4.5937 Å and c = 2.9581 Å [34]), similar to the cell of the anatase phase, but it is quite elongated along the c axis. ($c_{anatase}$ = 9.514 Å), The unit cell of the rutile phase contains two Ti situated at (0,0,0) and (½,½,½) and four O atoms, where the O atoms form a distorted octahedron around every Ti atom. It is the densest phase of titanium dioxide and is stable at high pressures and temperatures. Figure (I.1) is a modular representation of the rutile $TiO_2$ phase.

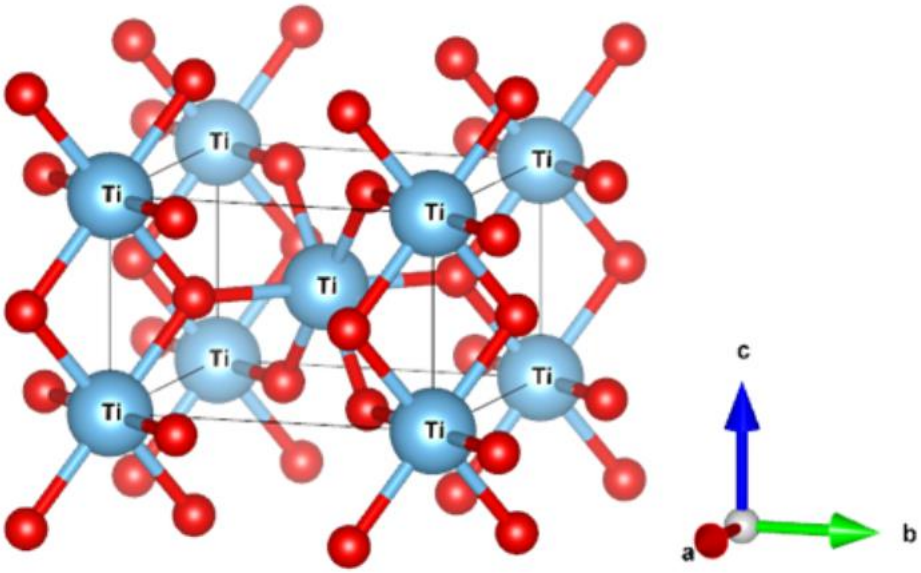


**Figure (I.1):** The rutile crystal structure [35].

### 2.1.2. Anatase phase

The anatase phase is more complex than that of the rutile phase. Anatase crystallizes in a quadratic system (space group I41/amd) whose lattice parameters are a= 3.7842 Å and c = 9.5146 Å [34]. The crystal structure comprises octahedrons linked together by edges, and these octahedra are elongated along the c-axis. The unit cell contains 4 Ti atoms located at (0,0,0), (½,½,½), (0,½,¼) and (-½,0,-¼) and 8 O atoms. This structure is formed at temperatures lower than those of the rutile phase formation. It crystallizes at around 400 °C and shares several properties with rutile, such as hardness and density. However, they differ in the arrangement and the distortion of the octahedra. (see figure (I.2)).

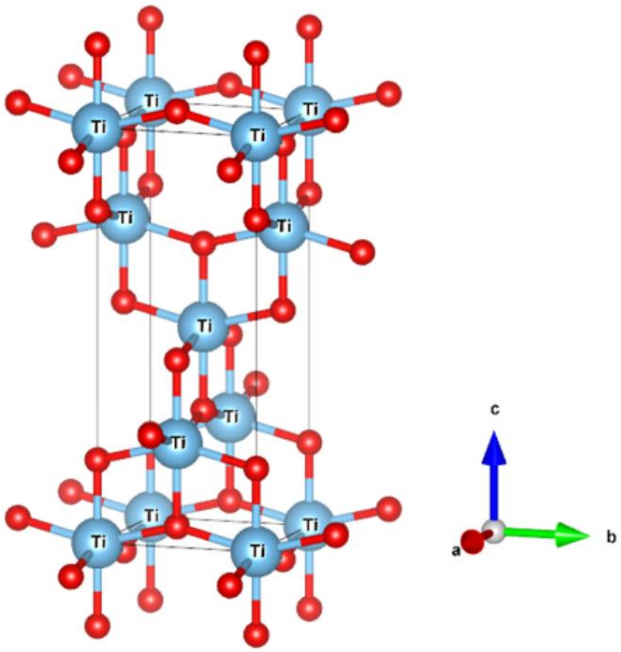


**Figure (I.2):** The Anatase Crystal Structure [35].

Table (I.1) summarizes the physical characteristics of the anatase and rutile phases of $TiO_2$ material.

**Table (I.1):**The main physical characteristics of anatase and rutile forms of $TiO_2$ [36].

| Property | Anatase | Rutile |
|---|---|---|
| Crystal structure | Tetragonal | Tetragonal |
| Atoms per unit cell | 4 | 2 |
| Space group | $I\frac{4}{a}md$ | $P\frac{4_2}{m}nm$ |
| Lattice parameters (nm) | a=0.3785; c=0.9514 | a=0.4594; c=0.29589 |
| Unit cell volume ($nm^3$) [a] | 0.1363 | 0.0624 |
| Density ($kg/m^3$) | 3894 | 4250 |
| Calculated indirect band gap (eV) | 3.23 ~ 3.59 | 3.02 ~3.24 |
| Experimental band gap (eV) | 3.2 | 3 |
| Refractive index | 2.54 ~2.49 | 2.79 ~2.903 |
| Solubility in HF | Soluble | Insoluble |
| Solubility in $H_2O$ | Insoluble | insoluble |
| Hardness (Mohs) | 5.5 ~6 | 6 ~6.5 |

### 2.1.3. Phases stability

Titanium dioxide is very stable thanks to the strong bonds between the tetravalent $Ti^{+4}$ cations and the bivalent $O^{-2}$ anions; therefore, it is chemically inert. When the stoichiometry of titanium oxide is changed from 0 to 2, Ti, $Ti_2O$, TiO, $Ti_2O_3$, $Ti_3O_5$, $Ti_nO2_{n-1}$, and $TiO_2$ are encountered (see figure (I.3)). No titanium oxide structure with a stoichiometry greater than two has been reported [34]. The rutile and anatase structures are only compatible with a stoichiometry greater than 1.95.

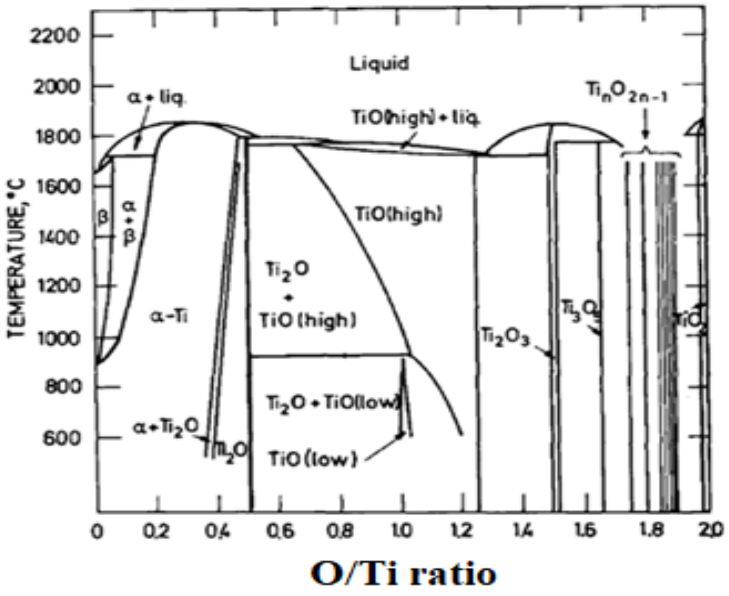


**Figure (I.3):** Titanium-Oxygen phase diagram [37].

The main difference between the properties of the anatase and rutile phases are:

- The crystallite size of the anatase phase is larger than that of the rutile phase.
- The light absorption of the anatase phase is lower than that of the rutile phase.
- The photocatalytic activity of the anatase phase is much higher than that of the rutile phase.

Hanaor et al. [36] grouped the main conditions that could promote or inhibit phase transformation (from anatase to rutile), including pressure, temperature, morphological effects, and doping elements.

Figure (I.4) shows the phase transition limits in $TiO_2$ powder as a function of temperature and working pressure. Over the last 50 years, various studies have been conducted to study anatase transition kinetics to rutile. However, different transition temperature values have been reported depending on the preparation technique, morphology, and structure of $TiO_2$ as deposited. For temperatures above 600 °C, the anatase structure changes to the rutile structure [38]. This kinetics strongly depends on the presence of impurities within the material. For example, the anatase phase completely disappears at approximately 530 °C, 680 °C, and 830 °C for powder samples containing vanadium, molybdenum, and tungsten, respectively [39].

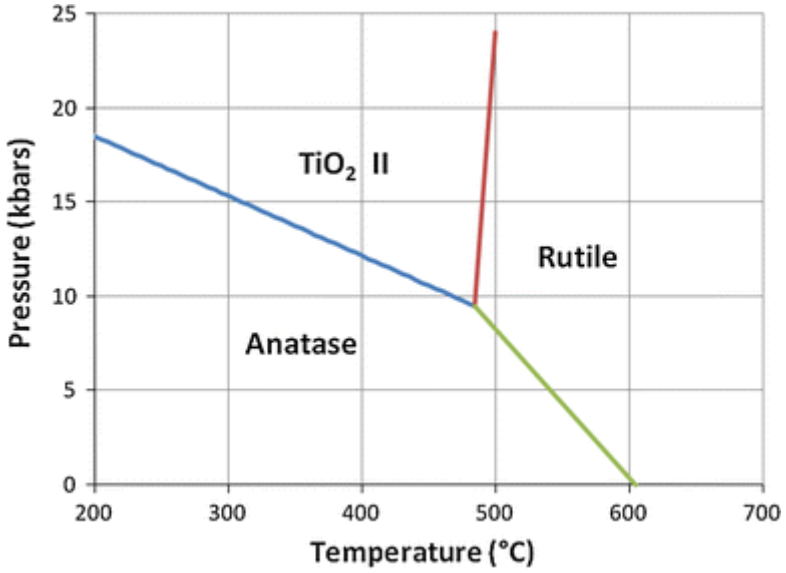


**Figure (I.4) :** Boundaries of phase transitions in $TiO_2$ vs annealing temperature and pressure [36].

The anatase phase transforms into a rutile phase at high temperatures. The transformation temperature relied on the preparation method as well as the thermal annealing and other mechanical processes to promote this transformation, such as ambient pressure, doping, porosity, etc. In many works, it has been reported that the rutile phase is more stable than anatase, which is confirmed by thermodynamic calculations [40, 41]. This variation in stability indicates that the transition from the anatase phase to the rutile phase is an irreversible process, along with the fact that the rutile $TiO_2$ phase can never transform into the anatase phase, beyond the structural properties, titanium dioxide also exhibits intriguing electrical characteristics.

### 2.2. Semiconductor properties

In contrast to the chemical properties of the titanium dioxide, the electrical properties are unstable, making it a modest semiconductor or a poor insulator. For many applications, it would be interesting to make the $TiO_2$ more insulating or conductive. Since Fujishima and Honda established in 1972 that a $TiO_2$ electrode under UV exposure could decompose water into hydrogen and oxygen [42], titanium dioxide can be considered either as a broad n-type semiconductor band gap or as an oxide with a narrow band gap (figure (I.5)).

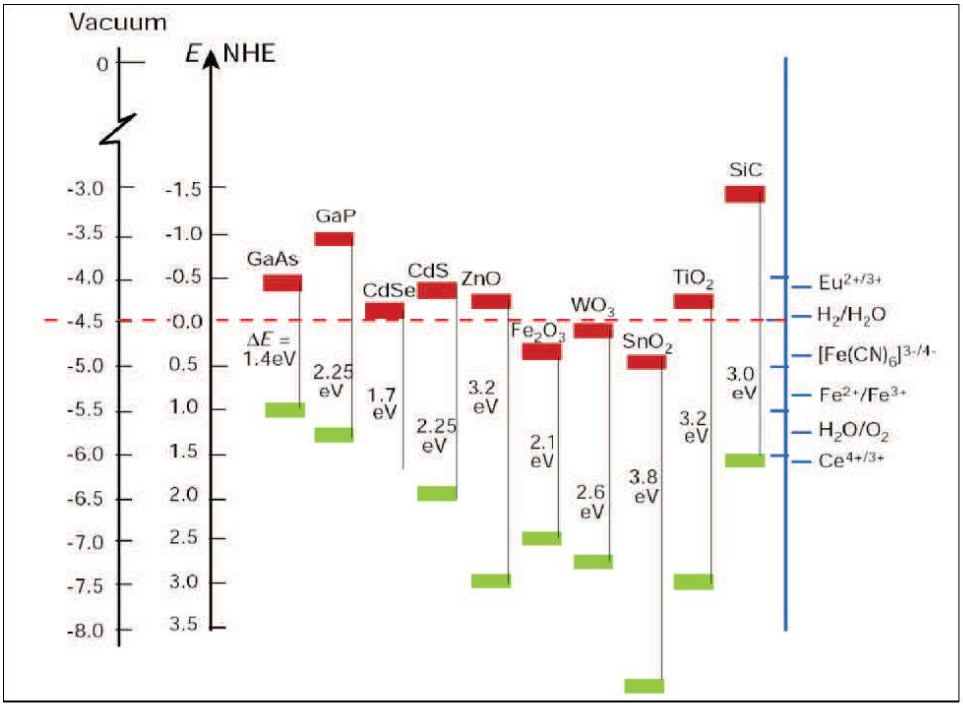


**Figure (I.5):** Band gap positions of several semiconductors in contact with aqueous electrolyte at pH = 1[43].

When a semiconductor receives a photon with energy *hv* greater than or equal to the width of its band gap, the photon will be absorbed. The electrons ($e^-$) of the valence band are thus excited and promoted into the conduction band, and vice versa for the holes ($h^+$) initially present in the valence band. This results in the creation of charge carriers in the form of photoelectrons and electronic holes according to the relationship:

$$TiO_2 + hv \rightarrow e^- + h^+ \quad \text{(I.1)}$$

For anatase, whose gap is ≈ 3.20 eV, this mechanism takes place at a wavelength λ less than or equal to 380 nm, therefore belonging to the UVA domain. The photo-induced properties of $TiO_2$ open the doors to several promising applications of $TiO_2$, among the methods to deposit $TiO_2$ with controlled properties there is the sol-gel process.

### 2.3. Sol-Gel Synthesis

The sol-gel process has been known since 1845 thanks to the work of J.J Ebelmen, who was the first to describe the synthesis of silica from a silicon alkoxide [44]. This process allows the production of various oxides in different formats (powders, thin films, fibers). This diversity in materials and shapes has made this process very attractive in vast technological fields. It also has the advantage of using mild chemical synthesis and the possibility of

controlling many final product parameters, such as homogeneity, purity, porosity, and particle size. Sol-gel constitutes a particularly well-suited method for doping since the dopants can be introduced throughout the synthesis during the different stages. This allows a more homogeneous distribution within the matrix than other methods. The sol-gel reaction is a succession of condensation hydrolysis reactions of precursors, mainly $M^n (OR)_n$ alkoxides, in which simple alkyl groups surround the metal atom. These mineral polymerization reactions lead to increasingly condensed species forming colloidal silica particles forming sols and then gels, hence the name of the "sol-gel" process [45]. The drying and densification of these gels lead to glasses or ceramics. This synthesis method represents a new approach for preparing glasses and ceramics [46]. Other authors define the sol-gel process as producing dispersed materials by growing oxo-polymers in a solution [47]. Two synthesis routes are distinguished according to the nature of the molecular precursors used [34]: organic and inorganic.

**Inorganic route:** the precursor used is a metallic salt (chlorides, nitrates, oxychlorides) dissolved in an aqueous solution, and this leads to successive hydrolysis, followed by precipitation by condensation thanks to the formation of polymeric structures by oxo bond. Their main disadvantage is that they require an additional step to eliminate inorganic anions after a sol-gel reaction. This route is inexpensive but difficult to control, so it is still very little used at the expense of precursors using organic ligands. However, it is the preferred route for obtaining ceramic materials.

**Organic or polymeric route:** precipitation occurs by mixing an organometallic precursor with water in an organic solution, which leads to a succession of reactions (hydrolysis-condensation). This route is relatively expensive but allows fairly easy particle size control [34]. Among the precursors with organic ligands, the most frequently used in sol-gel chemistry are metal alkoxides whose generic formula is $M^n (OR)_n$, where M designates a metal atom of valence n (n = 4 for M = Ti), R an alkyl radical ($-C_xH_{2x+1}$) and OR an alkoxy group. This type of precursor, more precisely tetraethyl-ortho-titanate (of formula $Ti(OC_3H_7)_4$) and/or tetrapropyl-ortho-titanate (of formula $(CH_3CH_2CH_2O)_4Ti$), will be used in this work to produce thin layers of $TiO_2$. The sol-gel reaction occurs in two stages: synthesizing the "sol" and forming the "gel."

### 2.3.1. Sol

A sol is a suspension of colloidal particles in a liquid. The hydrolysis of molecular precursors obtains it: water is added to a solubilized alkoxide; the alkoxide is then hydrolyzed, forming colloidal $TiO_2$ particles (diameter from 1 to 1000 nm) [34]. If these particles are composed of reticulated chains of the M-O-M type, the sol is called "polymeric sol." In contrast, a sol made of three-dimensional oxide particles is called "particulate sol." The chemistry of sol-gel involves two types of reactions: hydrolysis and condensation. Although described successively below, these two mechanisms co-occur in the solution. Hydrolysis constitutes the step of initiating the condensation of alkoxides at room temperature. Metal alkoxides first react more or less quickly with the water contained in the solution. During this reaction, a hydroxyl group will bond to a metal atom via the hydrolysis reaction presented in the equation:

$$M^n(OR)_n + xH_2O \rightarrow M(OR)_{n-x}(OH)_x + xROH \quad \text{(I.2)}$$

if ($x = 1$):

$$M^n(OR)_n + H_2O \rightarrow (OH) - M(OR)_{n-1} + ROH \quad \text{(I.3)}$$

where ROH designates the parent alcohol of the alkoxide precursor.

The valence of titanium in alkoxide form is equal to four, which corresponds to its highest degree of oxidation. The metal then tends to increase its coordination in order to reach its maximum value which is 6. To do this, titanium uses its vacant states and accepts the non-bonding doublets of oxygen atoms. It is this phenomenon that makes titanium alkoxides very reactive with respect to hydrolysis. The mechanism is shown in figure (I.6).

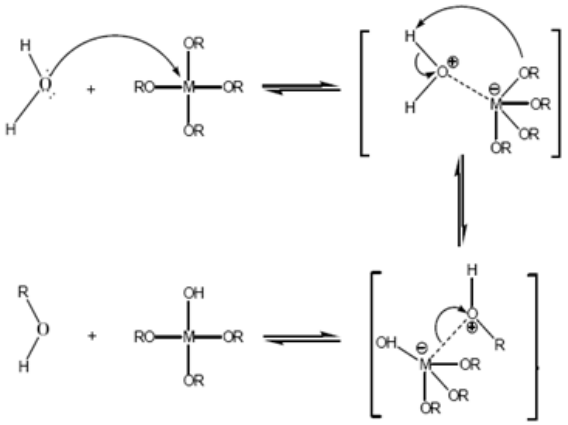

**Figure (I.6):** Mechanism of metal alkoxides hydrolysis [34].

### 2.3.2. Gel

The condensation stage of the sol allows a gel to be formed. This is the step of forming the three-dimensional structure schematized in figure (I.7).

$$M - OH + RO - M \rightarrow M - O - M + ROH \quad \text{(I.4)}$$

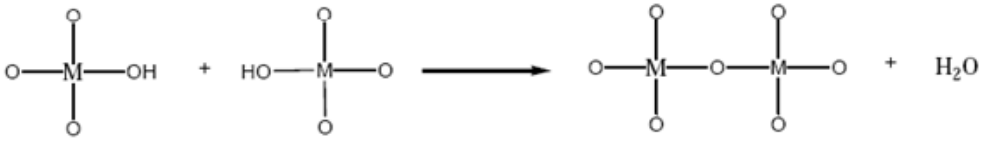


**Figure (I.7):** Mechanism of metal hydrolysate condensation [34].

The -OH groups produced during hydrolysis are good nucleophiles. They will, during condensation, lead to the creation of an amorphous oxide network made up of M-O-M chains (Ti-O-Ti in the case of $TiO_2$) with groups of alkoxy hydrolyzed or not at the end of the chain. A gel is obtained when hydrolysis and condensation reactions are sufficiently advanced. The transformation of the solution into a solid polymer network is then called the sol-gel transition.

The gelation reaction can occur in situ in a liquid solution. The structure of the final gel will depend on the relative rate of hydrolysis/condensation reactions. The gel can be a self-supporting material, called a monolith when its dimensions exceed a few tens of micrometers or a coating deposited in the form of thin layers on a support. After gelation, the polymeric oxide network is formed. The solvent's total evaporation leads to the wet gel's transformation into a dry gel called xerogel. The total solvent removal is accompanied by the forming of new bonds between the different branches of the polymeric oxide network (branching). The drying conditions of the gel will, in turn, condition the structure and properties of the xerogel. For example, drying the gel under ambient conditions will cause a reduction in volume by a factor of 5-10 under the action of capillary forces due to the withdrawal of the liquid phase, thus reducing its volume porosity. This gel deformation will also promote the branching of the polymer network initially obtained, thus increasing its rigidity [34]. In the case of thin films, the gelling and drying stages are incredibly rapid due to the small quantity of liquid deposited (typically a few seconds) and generally inseparable. After the deposition of a liquid film, the evaporation of the solvent is very fast and increases the re-concentration of the reactive species. Consequently, drying the gels in thin layers is also a critical step. Indeed,

under ambient drying conditions, the rapid evaporation of the solvent causes the accelerated formation of intense capillary stresses within the film. The intensity of these stresses can be greater than 100 MPa [34]. In addition, the presence of the substrate harms the homogenization of these constraints in the thickness of the film because the solvent can only evaporate from the external face in contact with the air. This, therefore, results in a stress gradient that mechanically weakens the xerogel film. In addition, the adhesion of the film to the substrate partly opposes the relaxation of the stresses present in the film. These different aspects mean that inorganic xerogel films with too great thickness (more significant than a few 100 nanometers) will tend to crack. One way to overcome this drawback is to implement multilayer deposition protocols.

### 2.3.3. Crystallization by gel annealing or thermal treatment

Although the sol-gel process makes it possible to obtain solid materials at room temperature, it is often necessary to resort to heat treatment of the dry gel obtained to improve its properties. Depending on the functionalities sought, this heat treatment will occur at a higher temperature and will cause new structural transformations of the oxide network. This step allows:

- The elimination of the last traces of solvent.
- The decomposition of anions (alkoxide groups) to form oxides.
- The crystallization of $TiO_2$.

In order to accelerate the elimination of carbonaceous species, air is injected into the furnace during annealing.

### 2.3.4. Advantages of the sol-gel process

Although the development of oxide materials is possible by several synthesis methods, the sol-gel method is an interesting choice for several reasons. This process makes it possible to produce monoliths, films, fibers, and powders of uniform size (figure (I.8) below). It also allows precise control of stoichiometry [47, 48]. In addition, it is generally known that the properties of the layers strongly depend on the preparation method, and the advantages of the sol-gel process at this level are numerous: excellent homogeneity due to the dispersion of the precursors in solution, easy control thickness, and an ability to produce complex shaped coatings. This method also makes introducing dopants from organometallic precursors or inorganic salts possible. Finally, it should be noted that this technique has been well-known

in the laboratory for around 30 years, especially for developing materials such as $ZrO_2$ zirconia [49].

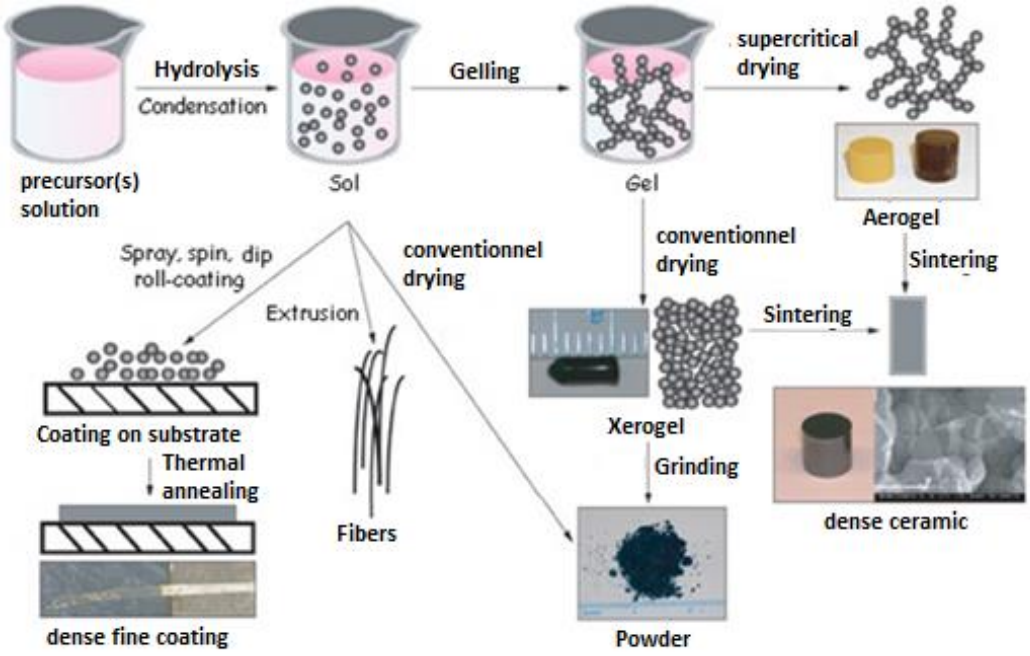


**Figure (I.8):** Various forms of materials derived from the sol-gel process [34].

### 3. Different studies on nitrogen doping of the $TiO_2$ lattice

In nonmetal doping, the $TiO_2$ photo-catalyst has a central issue, which is the photocatalytic activity under visible light, which is very low when compared to ultraviolet light [29, 50, 51]. Several methods exist for a charge balance if an anion is substituted with a higher valence anion. The three methods are:

1. Host-cations may oxidize to a higher charge state,
2. Anion vacancies form that effectively remove negative charges from the crystal,
3. Cation interstitials form that introduce additional positive charges in the crystal.

The first method is impossible in the stoichiometry of $TiO_2$ material since the Ti ion is already in its maximum valent 4+ charge state. In sub-stoichiometric $TiO_2$ material, $Ti^{3+}$ sites can be oxidized by introducing higher valent anions. The result is then identical to the method 2. The higher valence of the N-dopants relative to the host O-anions could be compensated by the formation of O vacancies and Ti-interstitials [52]. Oxygen atom vacancies, in the absence of N dopants, can cause a decrease of $Ti^{4+}$ to $Ti^{3+}$ and the occupation of Ti-3d states.

Asahi et al.[53] reported theoretical outcomes from substituting N, F, C, P, or S for O atoms in the $TiO_2$ lattice. Results of the calculation of the density of states (DOS) for anatase $TiO_2$ material suggest that substitutional type doping using N atoms is effective due to combining nitrogen 2p states with oxygen 2p states, causing a significant decrease in the width of the overall band gap energy.

### 3.1. Rutile and anatase N-doped $TiO_2$ photo-activity

The origin of the variation in photoactivity between anatase and rutile $TiO_2$ due to substitutional nitrogen doping was investigated using state-of-the-art density functional theory (DFT) calculations by Di Valentin et al [54]. The study revealed both similarities and differences in the electronic structure of anatase and rutile. A key difference is the contraction of the valence band width W(O2p) in rutile upon nitrogen doping. In both polymorphs, there are N2p localized states above the top of the O2p valence band. In the anatase $TiO_2$ phase, these states cause a redshift of the absorption band edge towards the visible region. However, in the rutile phase, the contraction upon nitrogen doping resulted in a lowering of the valence band maximum ($E_v$) by 0.43 eV compared to the undoped case (see $E_4$ in Fig. (I.9)). The highest nitrogen-induced level is 0.38 eV above $E_v$ (see $E_3$ in Fig. (I.9)), making the N2p localized states slightly lower in energy (by 0.05 eV) than $E_v$ in pure rutile resulting in an overall rise of the optical transition energy and band gap increase (see figure (I.9)).

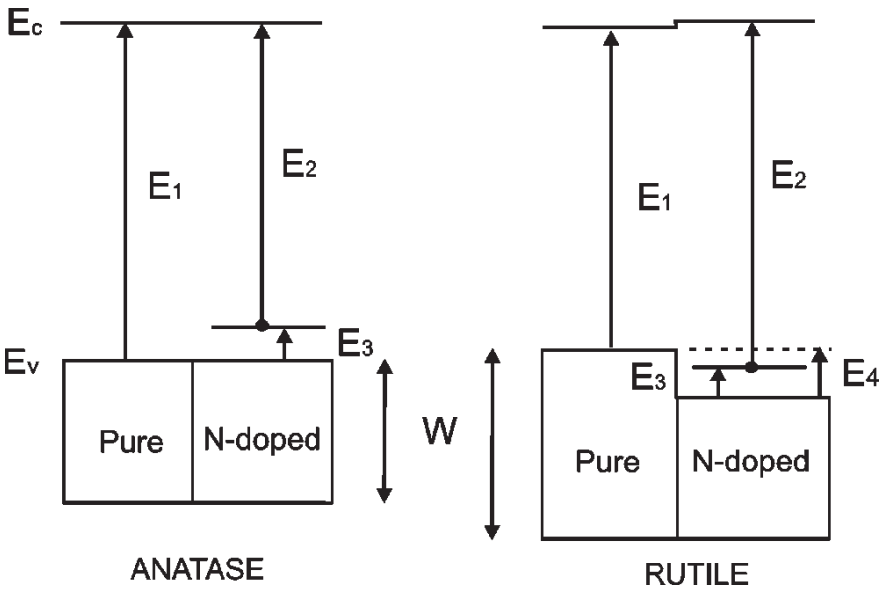


**Figure (I.9):** Schematic presentation of band structure in N doped anatase and rutile $TiO_2$ phases [54].

The modification mechanism of Nitrogen-doped $TiO_2$ has three different significant opinions about [55] (can be generalized for nonmetals doping):

1. Band gap energy narrowing.
2. New impurity energy levels.
3. New oxygen vacancies.

Band gap energy narrowing has been studied by Asahi et al.[53], revealing that N2p states hybridize with O2p states in the anatase nitrogen-doped $TiO_2$ because their energies are almost equal. Thus, the band gap energy of N-$TiO_2$ is narrowed, leading to the ability of the semiconductor to absorb visible light. Impurity energy levels were studied by Irie et al. [56], and it was revealed that oxygen sites substituted by N atom (in $TiO_2$) form isolated impurity energy levels on top of the valence band. Irradiation with ultraviolet light excites electrons in the valence band and the impurity energy levels. However, visible light irradiation only excites electrons in the impurity energy levels [57]. $TiO_2$ doping with substitutional N could have empty acceptor states above the valence state. In contrast, $TiO_2$ doping with interstitial N has isolated impurity states in the mid-band gap (about 0.7eV at the top of the valence band). N2p states primarily hybridize these impurity energy levels, and O2p states [58]. Lastly, O vacancies were studied by Ihara et al. [59]. They stated that oxygen-deficient sites created in the grain boundaries are essential to promote visible light activity. N doping in parts of oxygen-deficient sites is necessary for re-oxidation as blockers.

### 3.2. Nitrogen sites and efficiency in the $TiO_2$ lattice

Nitrogen atoms can occupy substitutional sites (N–Ti–O and Ti–O–N) or interstitial sites ($\pi^*$ character NO) in the $TiO_2$ lattice. Figure (I.10) shows the structures of three kinds of nitrogen centers:

- Substitutional defects, $N_s$, in which an N atom replaces an O atom.
- In the interstitial defects, $N_i$, the N atom is located in an interstitial place, and the O atom is also displaced from its original site.
- Substitutional-interstitial defects, $N_{si}$, in which the N atom occupies the same position as in the case of the $N_s$ defect, and the O atom occupies an interstitial place [57].

The change in the dopant states for substitutional versus interstitial N impurities in the anatase $TiO_2$ was studied both theoretically using DFT (density functional theory) calculations and experimentally, especially using electron paramagnetic resonance (EPR) spectroscopy, XPS, and photoluminescence measurements [50, 60]. The differing

experimental conditions and preparation methods drastically influence the nature of the measured XPS signals.

The study of Asahi et al. [53] revealed that the films exhibit N1s XPS peaks at 396, 400, and 402 eV binding energies. The authors of this study claim that the N species responsible for the overall band gap energy narrowing effect exhibit the 396 eV N1s binding energy. Similar N-doped powders that did not show the 396 eV XPS feature also did not show improved photocatalytic activity [53]. This peak is assigned to substitutionally bonded Nitrogen- the active dopant in that material. They suggested that substitutional type doping using N is effective because of the mixing of N2p states with O2p states, causing a considerable decrease in the width of the overall band gap energy. However, they reported that interstitial doping kind and a mixture of both substitutional and interstitial kinds were both found to be inefficient. Furthermore, in the work of Sangwook et al. [61], it is revealed that N atoms in substitutional sites improve the photocatalytic activity of $TiO_2$ under visible light more effectively than N atoms in interstitial sites.

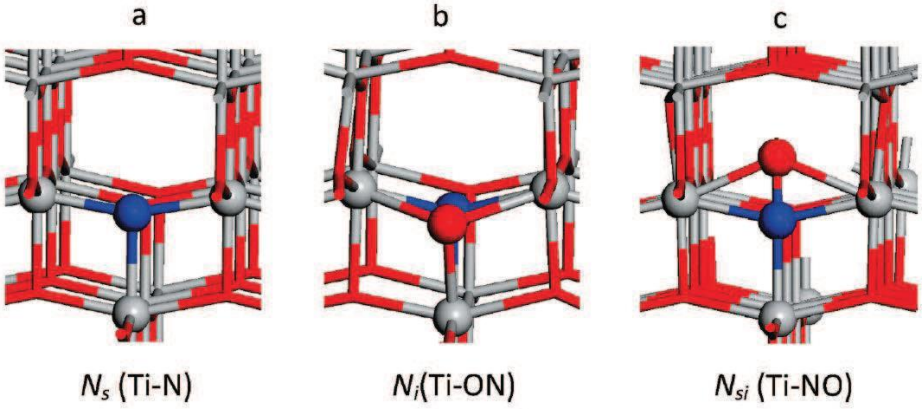


**Figure (I.10):** Structures of the three Kinds of N centers (a) substitutional $N_s$ (b) interstitial $N_i$ and (c) substitutional-interstitial, $N_{si}$ [58].

In contrast, Peng et al. [31] found that the synergetic effect of interstitial and substitutional nitrogen of N-doped $TiO_2$ can give the best photocatalytic activity. Similar results were also concludes by Dong et al. [62]. In O vacancies, Lee et al. [63] showed that interstitial doping states involving N–Ti–O or Ti–N–O bonds are more efficient for photocatalytic activity than the substitutional N doping states. Also, Shen et al. [64] found that the interstitial nitrogen presence is favorable to increase the hydrophilicity of N-doped $TiO_2$.

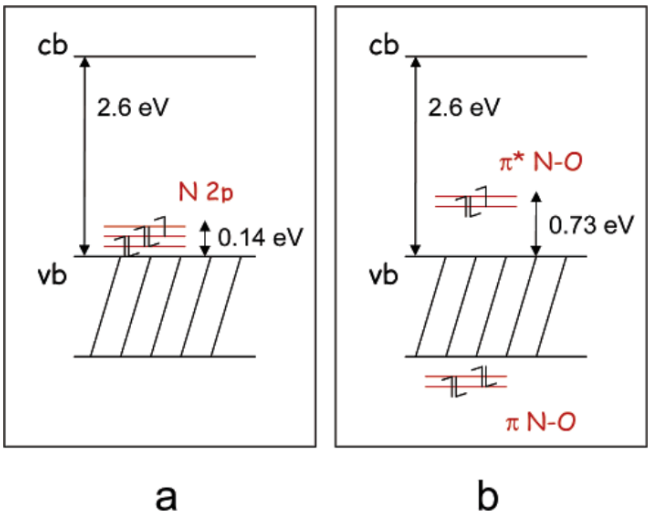


**Figure (I.11):** Electronic structure computed for (a) substitutional and (b) interstitial doping models [60].

For substitutional kind N, these states are located at 0.14 eV at the top of the valence band, and for interstitial kind N species (referred to as N-O), the localized states are determined to lie at 0.73 eV at the top of the valence band [62, 65] (figure (I.11)). Also, these calculations have proven a significant decrease in the energy formation for O vacancies due to additional N atoms in the lattice. This indicates that O vacancies are induced mainly by N doping in the $TiO_2$ [60].

Most N-doped $TiO_2$ manifested visible light absorption in the wavelength range of 400-600 nm, attributed to the presence of isolated N2p states at the top of the valence band at lower N concentration (less than 2%) that could be doped into the $TiO_2$ lattice [29, 66]. A shift towards visible light regions in the absorption spectra could be accomplished in the case of higher N doping concentration (up to 17%) with the N substitutional sites [58, 65].

### 3.3. Nitrogen-doped $TiO_2$ phase

Because the N atom is only 7% smaller than the O atom, substituting N in the O sub-lattice is possible. Hence, N is unlikely to destabilize the $TiO_2$ lattice, and so it would be an inhibitor of the phase transformation from the anatase phase to the rutile phase during any post-thermal treatment (figure (I.4)); however, it could frequently generate O vacancies in the $TiO_2$ lattice. It is worth mentioning that it is possible to thermal nitride $TiO_2$ and fabricate nitrogen-doped $TiO_2$ only at high pressure (10 to 100 bar) and temperature (more than 900 °C) under $N_2$ or ammonia atmosphere [67]. These modifications significantly impact the photocatalytic properties of $TiO_2$.

## 4. Photocatalysis

The research on the photocatalysis field has received growing interest recently because it has seen extensive studies in the recent decades, since 1972 when Honda and Fujishima discovered the decomposition of water into oxygen and hydrogen using electrodes of $TiO_2$ (rutile phase) irradiated under UV rays [42]; since this discovery, the photocatalytic properties of $TiO_2$ have been used for multiple applications such as converting solar energy into chemical energy, photo-killing and elimination the bacteria [68], as well the elimination of the pollutants in the air and water [69, 70].

Titanium dioxide $TiO_2$ material has been the most prominent photocatalytic material due to its non-toxicity, relative abundance, optical properties, and stability in aqueous solutions. However, it can only reach a certain level of photocatalytic efficiency due to its fast electron-hole pair recombination time and its large band gap energy, which only absorbs UV light [58].

### 4.1. Photocatalysis and Catalyst

Photocatalysis is an advanced oxidation technique (AOD) that allows the mineralization of organic pollutants into $CO_2$, $H_2O$, and corresponding mineral acids. It is defined as the speed acceleration of a chemical reaction under the action of light in the presence of a semiconductor called a catalyst [71-73] without being consumed at the end of the reaction. Photocatalysis includes irradiating the semiconductor (catalyst) with photons of energy equal to or greater than the catalyst's band gap. The photo-catalytic activity describes the acceleration of a catalytic reaction by light and is associated with the reaction rate. Heterogeneous photocatalysis includes photo-reactions at the catalyst surface:

a) if the initial photo-excitation occurs on an adsorbed molecule, which then interacts with the catalyst, the process is called a photo-sensitized reaction.

b) if the initial photo-excitation occurs on the catalyst (photo-excited catalyst), which then acts on an adsorbed molecule, it is called a photo-catalyzed reaction.

### 4.2. Heterogeneous photocatalysis mechanism

When the light (photons of energy equal to or greater than the band gap of the catalyst) arrives at the surface of the catalyst, an electron (reduction site) is electronically excited from

the valence band to the conduction band, leaving behind a positively charged hole (oxidation site), both the electron and hole are used to induce the chemical reactions at the surface of the semiconductor material, the electron reacts with oxygen and forms superoxides, hydroperoxides and hydrogen peroxides which decompose into hydroxyls by the following reactions [74]:

$$O_2 + e^- \rightarrow O_2^{\bullet -} \quad \text{(I.5)}$$

$$O_2^{\bullet -} + H^+ \rightarrow HO_2^{\bullet -} \quad \text{(I.6)}$$

$$2HO_2^{\bullet} \rightarrow O_2 + H_2O_2 \quad \text{(I.7)}$$

$$H_2O_2 + e^- \rightarrow HO^{\bullet} + OH^- \quad \text{(I.8)}$$

$$H_2O_2 + O_2^{\bullet -} \rightarrow HO^{\bullet} + OH^- + O_2 \quad \text{(I.9)}$$

The holes react with reductants and form very powerful oxidizing radicals $OH^{\bullet}$, which are able to oxidize organic molecules (pollutants) and to mineralize completely $CO_2$ and $H_2O$ (destruction of pollutants) by the following reactions:

$$H_2O + h^+ \rightarrow HO^{\bullet} + H^+ \quad \text{(I.10)}$$

$$OH^- + h^+ \rightarrow HO^{\bullet} \quad \text{(I.11)}$$

$$Polluant + h^+ \rightarrow Polluant^{\bullet} \rightarrow R^{\bullet} + CO_2 \quad \text{(I.12)}$$

$$HO^{\bullet} + Polluant \rightarrow H_2O + CO_2 \quad \text{(I.13)}$$

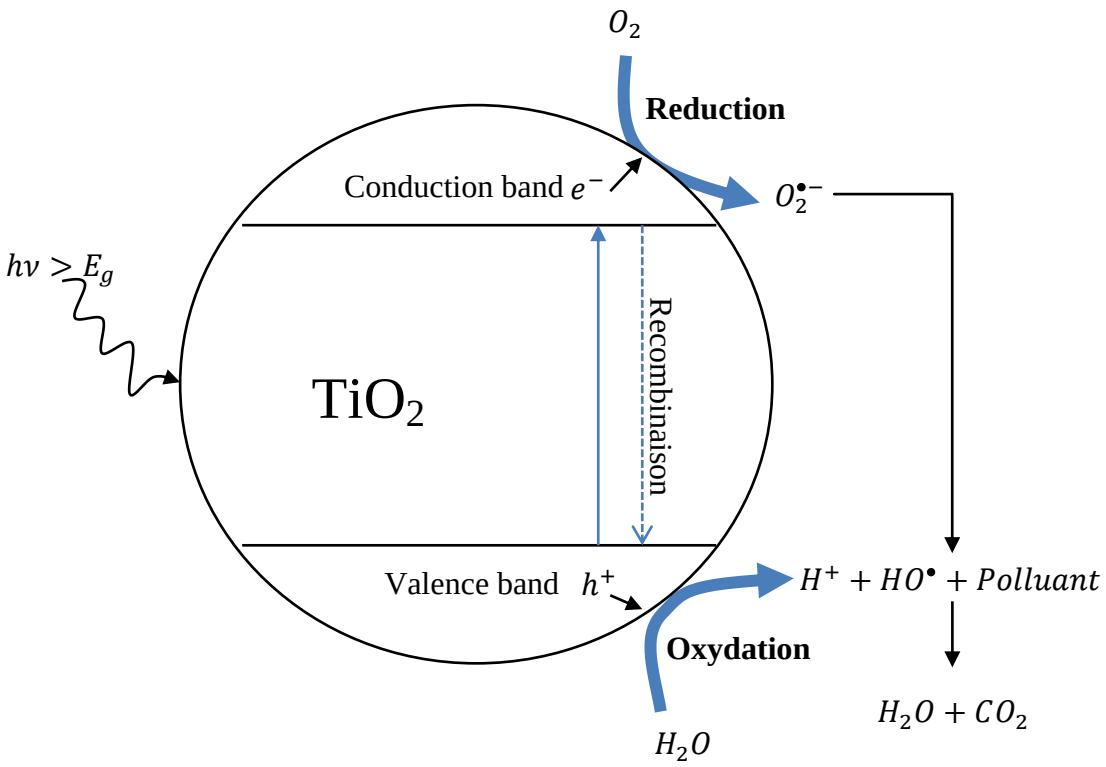


**Figure (I.12):** Schematic diagram for heterogeneous photo-catalysis principal. [74]

Heterogeneous photo-catalysis is a complex process that can be divided into the following steps:

1. Transfer of reactive molecules dispersed in the solution or gas phase to the catalyst surface: the diffusion of the molecules towards the surface is due to the concentration gradient at the solid/fluid interface.
2. Adsorption of reactive molecules on the catalyst's surface can be classified into two families: physisorption involving Van der Waals-type bonds and chemisorption involving essential binding energies.
3. Reaction on the surface of the adsorbed phase is the most essential step in which the photocatalytic reaction resides.
4. Desorption of products: active sites must be regenerated after the release of $CO_2$ and $H_2O$.
5. Elimination of products from the fluid/catalyst interface.

The lifetime of the pairs ($e^-/h^+$) is very short. In the absence of acceptor and electron donor, the recombination of the charges can occur in the bulk of the material or on its surface generating heat according to the reaction [75]:

$$\text{catalyst} + e^- + h^+ \rightarrow \text{catalyst} + \text{energy} \qquad \text{(I.14)}$$

This recombination of the pair $e^-/h^+$ can be avoided by the confining of charges via electronic states associated with irregularities on the surface or in the mass of the catalyst which may appear during its preparation, for effective confining, the catalyst's velocity must be greater than the recombination rate of the $e^-/h^+$ pair [74, 76]. In the case of $TiO_2$ as catalyst, the electrons can be confined by $Ti^{4+}$ cations, thus forming $Ti^{3+}$ sites [74, 77]. Also in many photocatalytic reactions, oxygen confines electrons and leads to the formation of $O_2^{\bullet-}$superoxide anions [74, 78] .

## 5. Conclusion

In this chapter, we had an overview about titanium dioxide ($TiO_2$) material. particularly focusing on its structural, semiconductor properties, and sol-gel synthesis method. We also discussed how nitrogen doping impacts the $TiO_2$ lattice. Finally, we explored photocatalysis and its principle.

# Chapter II:
# *Experimental Procedures and Characterization Techniques*

## 1. Introduction

In this chapter, we will essentially present the different experimental techniques used in this thesis to deposit $TiO_2$ thin films and N doped $TiO_2$ thin films. As well as the different characterization techniques used in this work for determining the structural, optical, electrical, chemical properties of the deposited films. The measurement of the photocatalytic activity is also presented.

## 2. The choice of substrate

The selection of the deposition substrate type is a very important phase because it affects the physical properties of the deposited film. Therefore, it is necessary to unify the substrate type across the deposition process to ensure a good correlation between the results. Nevertheless, some analysis techniques require a specific type of substrate. In our experiments, we used two different types of substrates: silicon wafers Si (100) and commercial glass slides. However, we chose commercial glass slides as our main deposition substrate because of these factors:

- The $TiO_2$ interface film/glass has minimal stress due to its thermal compatibility.
- The transparency of the commercial glass slides works well for films when conducting optical characterization in the visible spectrum.
- Financially inexpensive.

The structural and morphological characterizations were conducted using silicon wafers, and the optical characterization and photocatalytic tests were performed using commercial glass slides.

## 3. Cleaning of substrates

The cleanness level of the substrate's surface is a very critical standard for depositing high-quality ideal thin films with unaffected properties by the contamination of the surface; to ensure high degree of the substrate cleanness, the deposition substrates were subjected to a cleaning protocol composed of multiple cleaning stages ensuring the elimination of all kinds of impurities from organic compounds such as grease or resins to inorganic particles like dust to establish the best integrity possible prior the deposition process. Our adopted substrate cleaning protocol is illustrated in figure (II.1), and its stages are outlined below:

1- Initial immersion in a detergent solution to remove any organic residues and particles.
2- Rinse the substrates with deionized water to remove any detergent remnants.
3- A second immersion in an Acetone at an ultrasonic bath to dissolve any residual organic substances for 5 minutes.
4- A second rinse with deionized water to remove any remaining Acetone.
5- Another immersion in Ethanol at an ultrasonic bath to secure more refinement to the surface for 5 minutes.
6- A final rinse with deionized water to ensure a high degree of cleanliness.

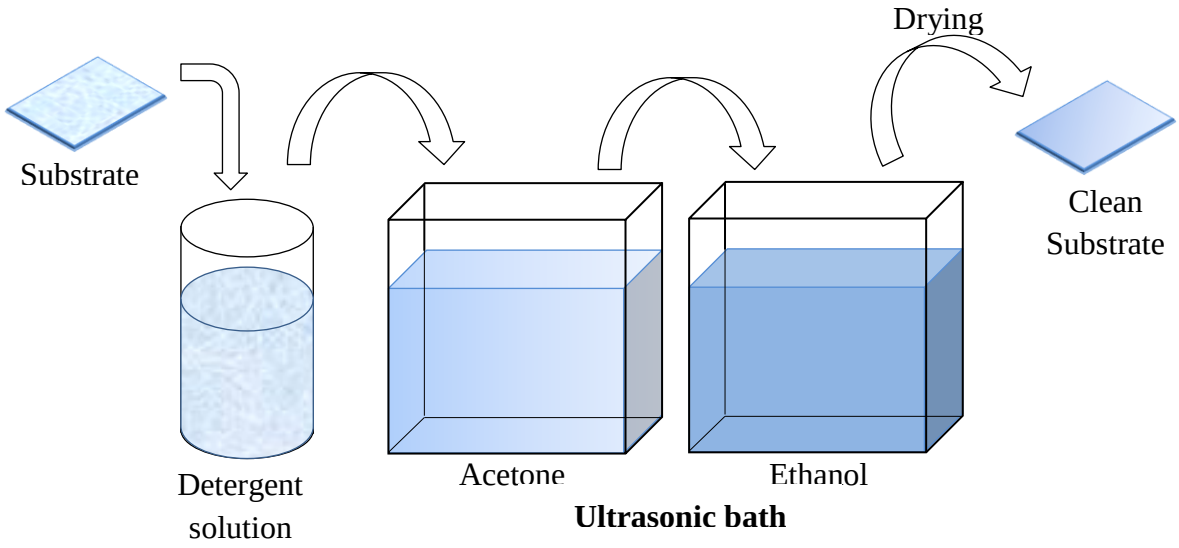


**Figure (II.1):** Protocol for substrate cleaning.

## 4. Thin Film Deposition Processes

Our chosen $TiO_2$ thin film deposition technique throughout all of our experiments is the sol-gel process, using both dip-coating and spin-coating methods. Moreover, our approaches to dope the nitrogen atoms into the $TiO_2$ were by using nitrogen precursor in the deposition solution, by treating the $TiO_2$ thin films with nitrogen plasma, and by coupling a GLAD deposited TiN sub-layer with $TiO_2$ film. All the deposition techniques and doping methods will be explored.

### 4.1. Preparation of the deposition solution

In this thesis, we have used a similar recipe in all of the experiments to produce the $TiO_2$ deposition solution [79]. As the deposition solution is based on the starting solution, we used:

- ✓ As an alkoxide (or precursor) for $TiO_2$ source, Tetraethyl–Orthotitanate ($(C_2H_5O)_4Ti$; TEOT) and Tetrapropyl–Orthotitanate ($Ti(OC_3H_7)_4$ ;TPOT).
- ✓ As a catalyst: Nitric acid ($HNO_3$).
- ✓ A (radical) solvent: Ethanol ($C_2H_6O$).
- ✓ Deionized water: to mediate polymerization reactions.

We prepared two solutions namely (A) and (B), in which solution (A) containing ethanol, water and Nitric acid is stirred for 10 min. Then, a solution (B), which contains the alkoxide and ethanol, is added to the solution (A), and the resulting mixture is stirred for 60 min. Afterward, a transparent solution of yellowish color and slightly viscous is obtained and remains stable for weeks. The quantity and concentration of the reactants used to prepare our solutions are optimized after several tests to obtain homogeneous, transparent, thin layers with good adhesion [79].

### 4.2. Spin-coating technique

The spin-coating technique is performed by placing a few drops of the deposition solution on the center of the substrate and spinning it at high speed to spread out the solution on the surface by centrifugal force. Spinning is maintained for a certain time until the desired thickness of the layer is reached. This coating technique can be divided into 4 stages, which are illustrated schematically in figure (II.2):

1) The dropping of the deposition solution.

2) Rotating the substrate.

3) The solution spreads uniformly on the surface, allowing the ejection of excess solution in the form of droplets.

4) Evaporation of the volatile solvent and formation of the thin film.

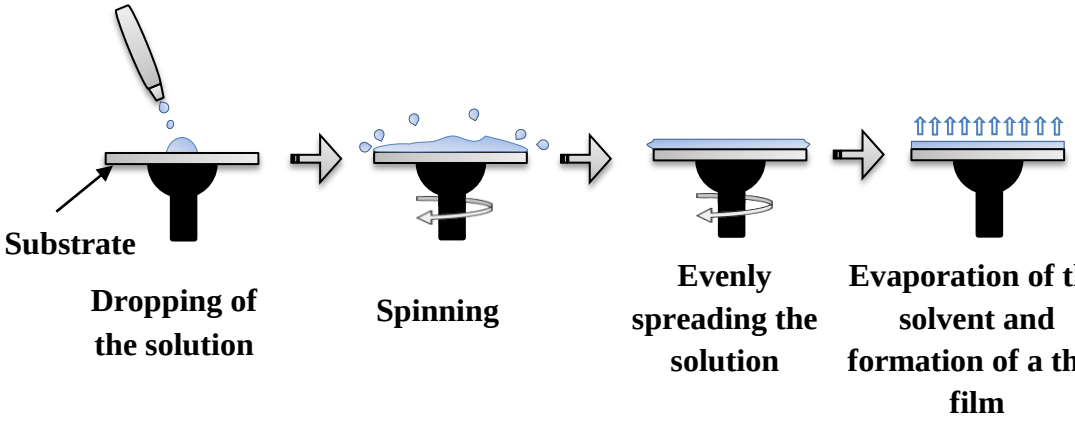


**Figure (II.2):** Schema of Spin-coating technique stages.

### 4.3. Dip-coating technique

The dip-coating deposition technique is performed by dipping the substrate into a beaker filled with the deposition solution and then withdrawing the substrate; during this process, the liquid starts to flow from it, and then the liquid drains, leaving an even film on the substrate; these two processes must be under controlled and stable conditions to ensure the optimal statue of the film's surface and thickness, the principle of this technique is illustrated in figure II.3.

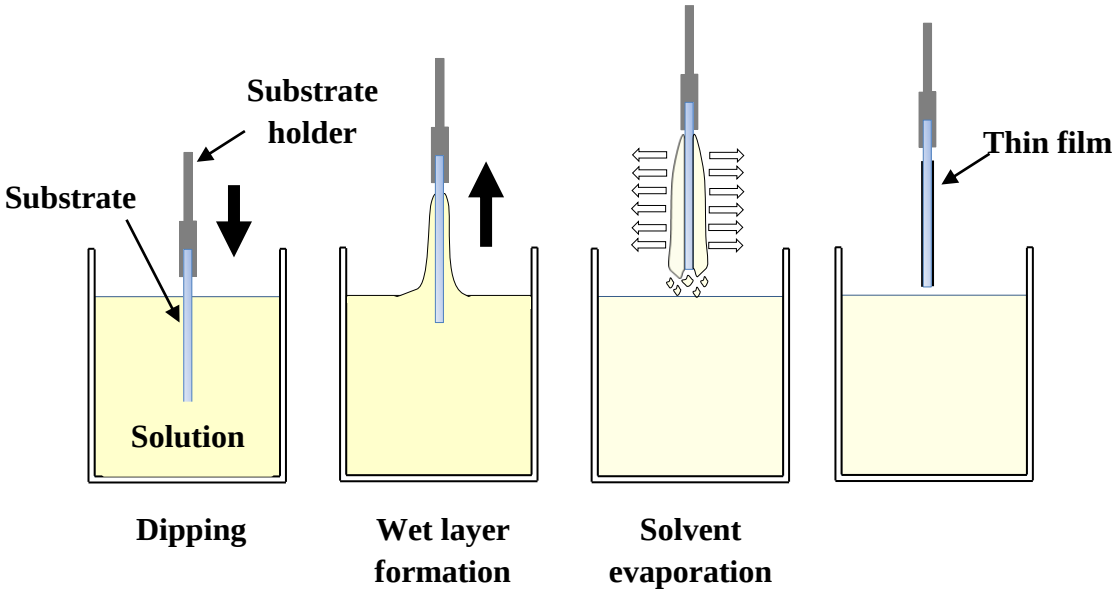


**Figure (II.3):** Schema of dip-coating technique stages.

### 4.4. Plasma treatment process

The plasma treatment system is performed by using a vacuum system to evacuate a small chamber connected to a DC power supply. Nitrogen gas is then introduced into the chamber and polarized, causing it to ionize and become nitrogen plasma, which is composed of positive nitrogen ions. The sample to be treated is placed in the negative slot of the power supply system in the chamber, which facilitates the penetration of the positive ions into the sample. The experimental setup is illustrated in figure (II.4).

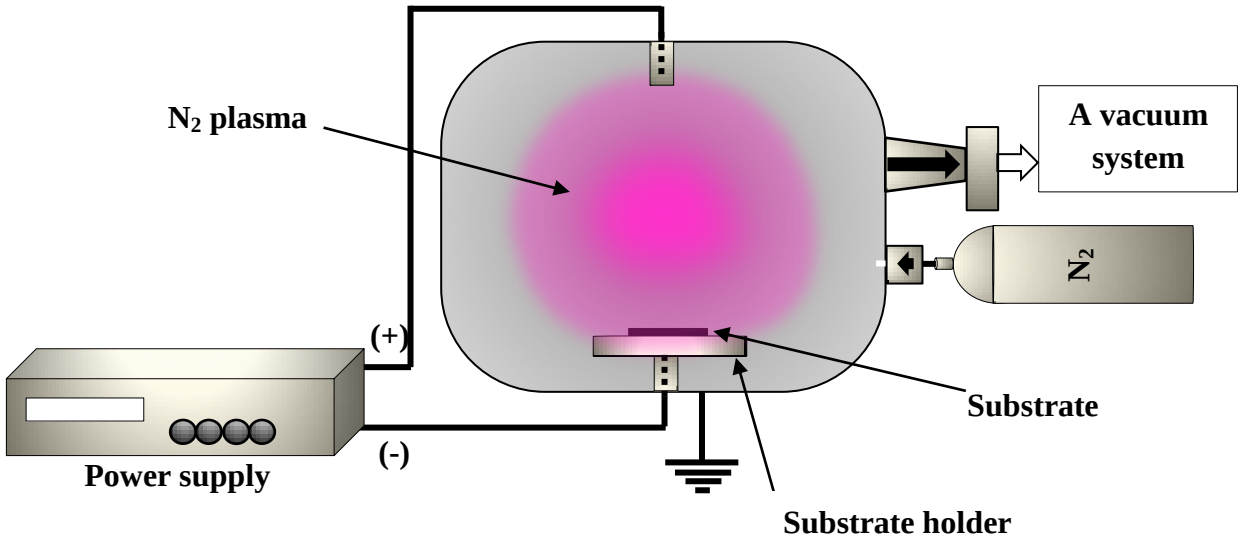


**Figure (II.4):** The plasma treatment system.

### 4.5. Magnetron sputtering technique

The magnetron sputtering technique is the most widely used in industry and scientific research for the deposition of thin films. This technique consists of placing a solid form target on a magnetron. Then, the sputtering chamber is evacuated and filled with an inert gas.

The application of a DC polarization between two electrodes contacted by an inert gas can achieve an electric discharge. A plasma is created, and its ions are accelerated to the negatively biased cathode (target). These energetic particles (ions) impinge on the target, causing transferring of its kinetic energy to the target atoms. If the energy gained by the target surface atoms exceeds their displacement energy, a collision cascade in the bulk of the target may be initiated. Finally, some atoms are ejected and transported in a gas state through the plasma until arriving at the substrate, forming a thin film. The glancing angle deposition technique (GLAD) consists of rotating the substrate holder.

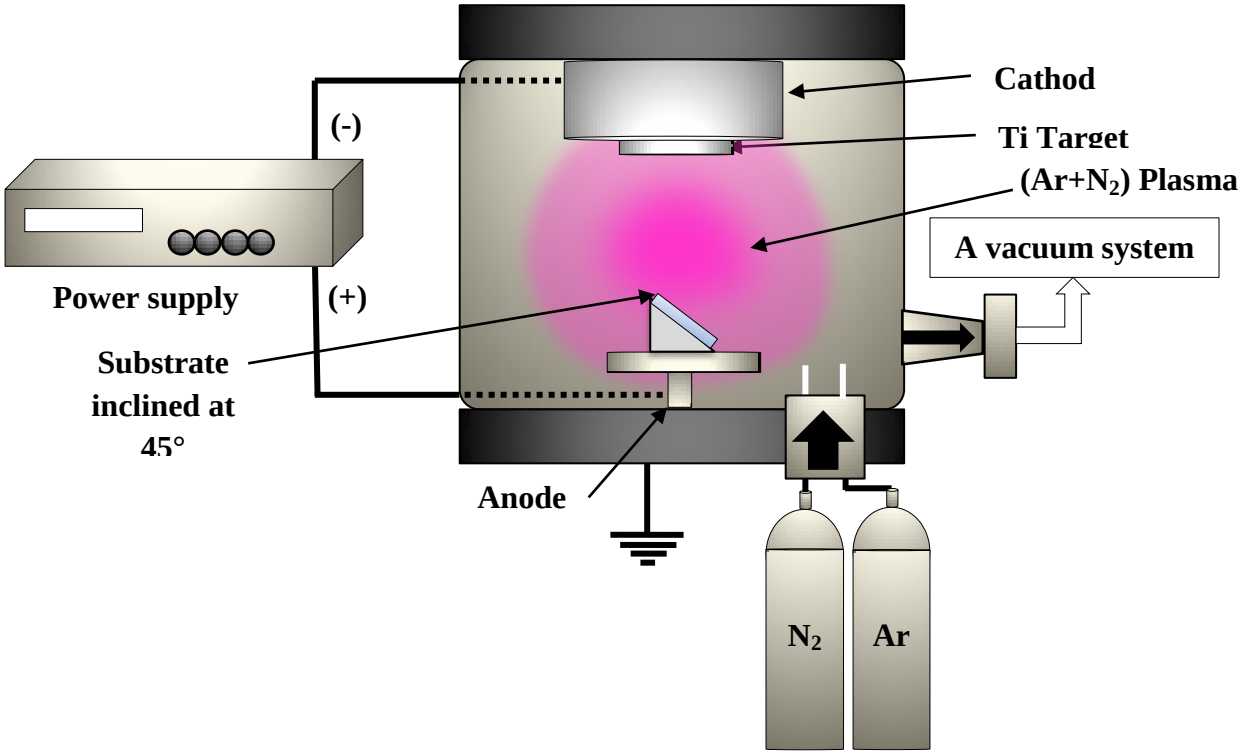


**Figure (II.5):** Schema of magnetron sputtering technique system.

### 4.6. Thermal annealing

The role of thermal annealing is very important process. It emphasizes the following points:

- Cause crystallization of the film.
- Harden the layer and remove residues of the precursors used in the starting solution.
- Eliminate organic groups such as alkyls (-OR-).
- Responsible for the appearance of mechanical stresses in the deposited thin film.
- Accelerates the closing of pores (this contraction is accompanied by a reduction in volume “thickness”).

The annealing stage is the final stage for obtaining the desired material.

## 5. Characterization techniques

### 5.1. X-ray diffraction (XRD)

X-ray diffraction technique (XRD) is a simple, non-destructive technique used to identify the crystal phases, determine the lattice parameters, and estimate the crystallite size of bulk and thin films. When a beam of X-rays interacts with a material, the electrons gravitating around the atoms begin to oscillate at the frequency of the incident beam, causing the emission of an electromagnetic wave with a frequency identical to that of the exciting wave. The waves from the electron clouds of the different atoms interfere destructively in most directions in space. However, as the atoms in crystalline materials are arranged periodically, there are certain conditions under which the waves will interfere constructively and produce an intense beam. These conditions are given by Bragg's law:

$$n\lambda = 2\, d_{hkl} \sin\theta \qquad \text{(II.1)}$$

Where $n$ is an integer representing the diffraction order, $\lambda$ is the incident X-ray wavelength, $d_{hkl}$ is the interplanar spacing of the crystal planes with Miller indices (hkl), and $\theta$ is the angle between the incident X-ray beam and the sample surface (see figure (II-6)). When the X-rays are diffracted by different planes, constructive interference occurs, resulting in a peak in the diffraction pattern; the peak's characteristics, position, and intensity can be collected and used to identify the crystal structure and phase of the material and calculate the lattice parameters and crystallite size.

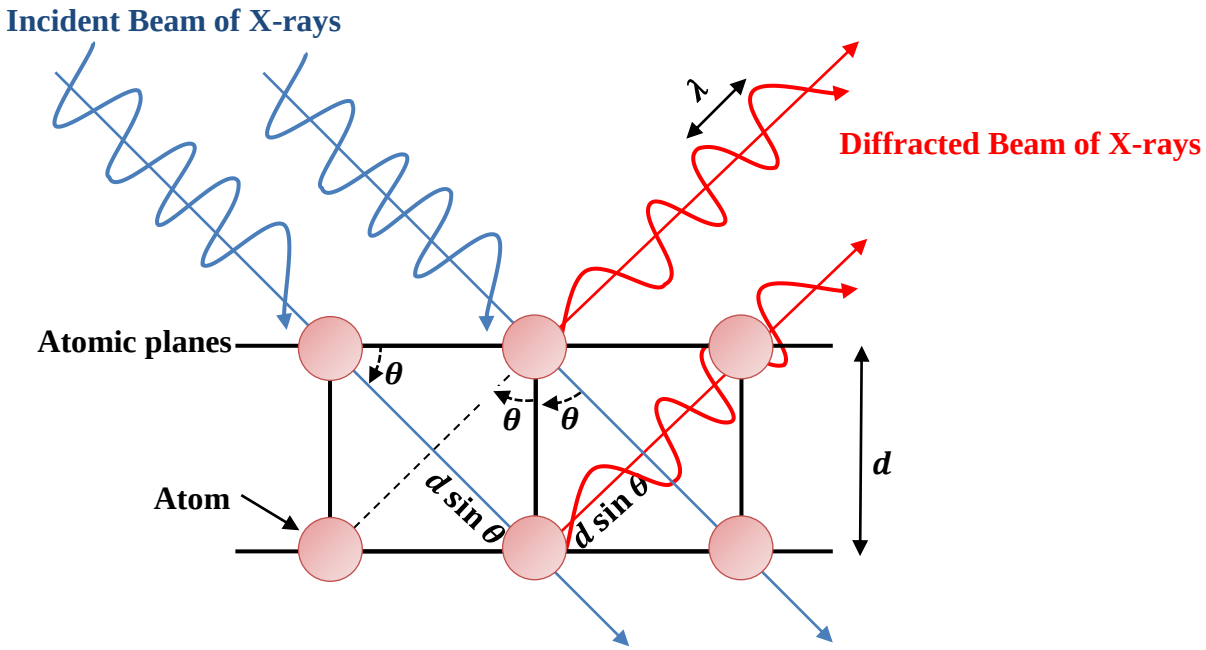


**Figure (II.6):** Representation of Bragg conditions in a crystal.

The X-ray diffraction has three main components:

- an X-ray source that generates a monochromatic beam of X-rays.
- a sample holder.
- a detector to measure the intensity of the diffracted X-rays as a function of the diffraction angle.

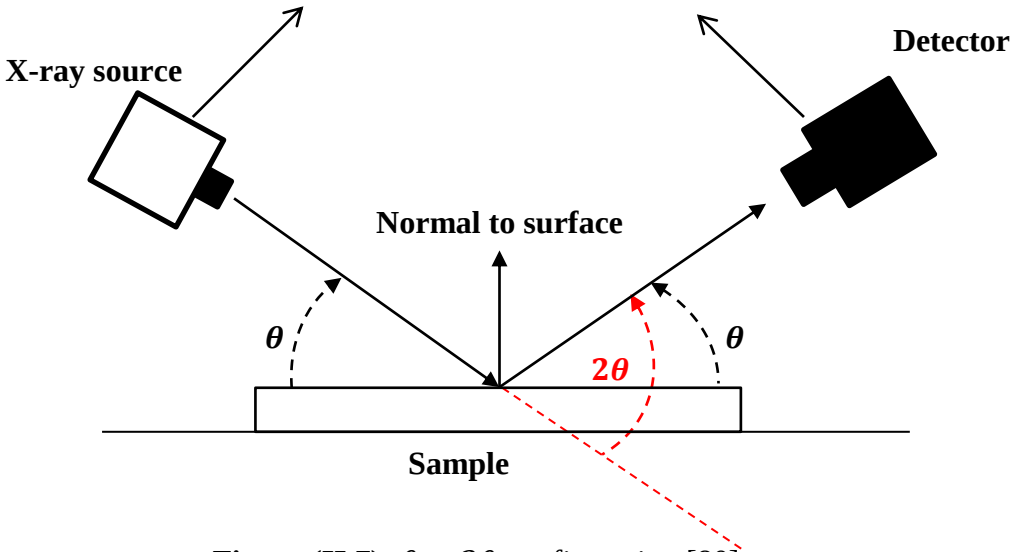


**Figure (II.7):** $\theta = 2\theta$ configuration [80].

The XRD measurement system has two main configurations:

- The normal $\theta = 2\theta$ (Bragg-Brentano) (Figure (II.7)): This configuration is suitable for powder samples and bulk materials; this configuration is based on the simultaneous moving of the sample and the detector at equal opposite angles while keeping the incidence angle constant.
- The grazing-incidence $\omega$ - $2\theta$ (Seeman-Bohlin) (Figure (II.8)): This configuration is suitable for thin films and surface layers; this configuration involves the detector scanning the desired angular range, the X-ray source is kept fixed, while the incidence angle is varied by the rotation of the detector.

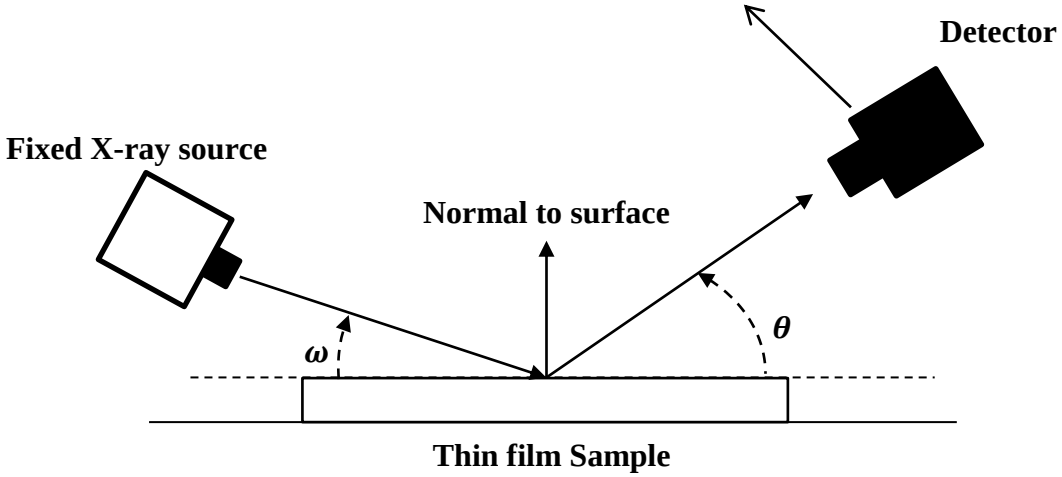


**Figure (II.8):** Grazing-incidence $\omega$ - $2\theta$ (Seeman-Bohlin) configuration [80].

In order to identify the material, the obtained diffracted patterns from X-ray diffraction analysis are compared with Joint Committee Power Diffraction Standards (JCPDS) data.

The used X-ray diffraction instrument in our thesis experiments is the Malvern EMPYREAN PANalytical Diffractometer equipped with Cu-Kα X-rays tube (1.5406Å).

### 5.2. Atomic Force Microscopy (AFM)

Atomic Force Microscopy (AFM) is a widely used technique to characterize materials at the Nano-scale level. It offers exceptional resolution and can reach the atomic level, allowing for the visualization of atomic structures, facilitating the analysis of morphological and mechanical properties. The main elements of an AFM are the optical detection device consisting of a laser diode and a photodetector, the AFM lever-tip assembly, the piezoelectric tube, and the feedback electronics. The atomic force microscope allows the topography of any surface to be observed in different conditions: in air, under a controlled atmosphere or in liquid. The principle of the AFM technique is schematically illustrated in figure (II.9).

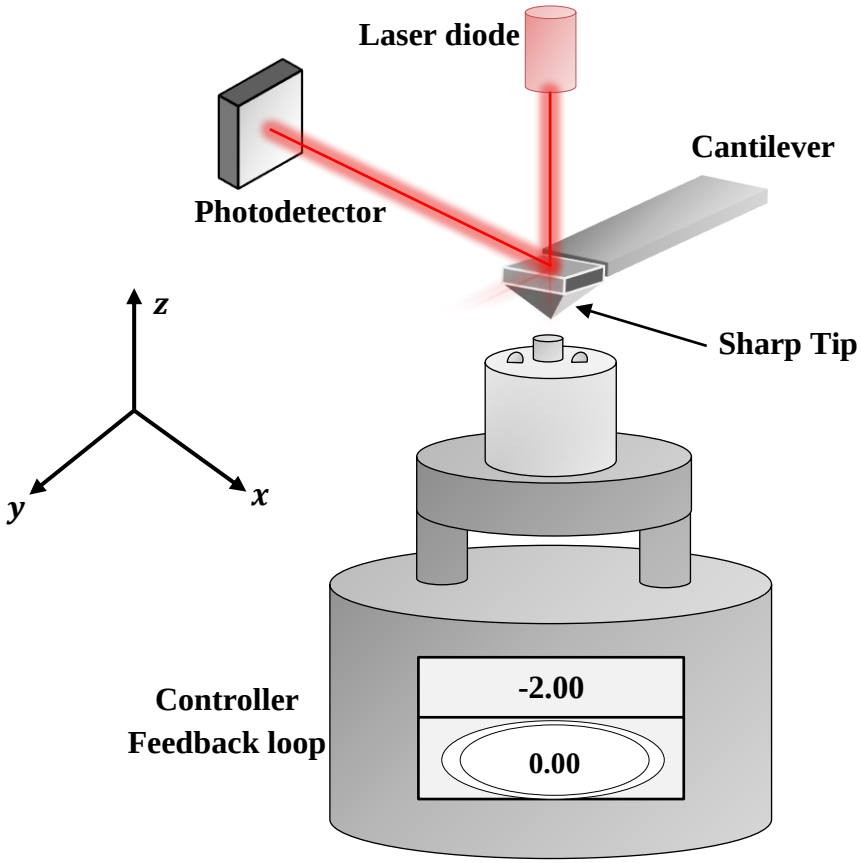


**Figure (II.9):** Principle of the atomic force microscopy [80].

The operation of the atomic force microscope is based on the detection of the attractive or repulsive forces in the range of $10^{-9}$-$10^{-5}$ N exerted between an AFM tip integrated into a lever and the surface of a sample. The very fine tip (2-30 nm radius) is brought into contact or held a few nanometers from the surface of the sample. When the tip approaches the surface, a negative deflection of the cantilever appears, indicating an attractive force due to the surface (van der Waals force). After the approach, the cantilever undergoes a jump on contact and then a positive deflection, which indicates a repulsive force due to the mechanical contact of the tip with the surface. The deflection of a laser visualizes the movements of the cantilever, reflected on the rear surface of the cantilever [81, 82].

A piezoelectric transducer is used to allow scanning of the sample surface. It makes it possible to measure the roughness of the surface, to determine their microstructures up to a resolution close to the atomic scale (in contact mode), the AFM also makes it possible to measure forces of the order of the piconewton (10−12 N). The force of interaction between the atoms on the tip and those on the surface is kept constant during scanning via a feedback loop. The feedback loop controls the tip-sample position so as to maintain this interaction

constant at the value of the set force. Recording the movements (in the X, Y and Z directions) of the piezoelectric tube then provides 3D topographic information of the surface. This measurement allows us to determine the surface roughness or as often expressed as the Root Mean Square (RMS) roughness, using the following formula [34]:

$$RMS = \sum_{i=1}^{n} \sqrt{\frac{(Z_i - Z_m)^2}{n-1}} \tag{II.2}$$

Where $Z_m$ is the average height value over the analyzed surface, $Z_i$ is the current height value, and $n$ is the number of measurement points.

AFM operates in different modes, such as contact mode, resonant mode (tapping), and non-contact mode. AFM imaging was conducted in "contact" mode using an Asylum Research MFP 3D AFM equipped with silicon nitride tips (AC240TS) with a curvature radius of approximately 10 nm, a resonance frequency of 70 KHz, and a spring constant of 2N/m. These measurements were carried out at the Ferhat Abbas University of Setif 1.

### 5.3. UV-Visible Spectroscopy

Ultraviolet-visible spectroscopy is a spectroscopy technique that involves photons whose wavelengths are in the ultraviolet (200nm-400nm), visible (400nm-750nm), or near-infrared (750nm-1400nm) range. UV-Visible spectroscopy is a very interesting technique for being accurate, quick, and non-destructive and does not require any sample preparation; and can determine the optical properties of a material. The optical absorption of a material reflects its energy bands. A photon of energy absorbed by the material induces electronic transitions between different states. Thus, for each photon absorbed, a transfer of energy is carried out from the incident light beam to the absorbing medium.

This technique is commonly used quantitatively to determine the concentrations of an absorbing species in the sample by using the Beer-Lambert law. The principle of UV-VIS Spectroscopy declares that when a beam of monochromatic light passes through a homogeneous medium of an absorbing substance, the rate of decrease in intensity of radiation through an absorbing substance is directly proportional to the incident radiation intensity and the substance concentration, the expression of Beer-Lambert law is [83]:

$$I(x) = I_0 \exp(-\alpha\, d) \tag{II.3}$$

where $\alpha$ represents the absorption coefficient, $d$ is the thickness of the film, $I_0$ is the intensity of the incident beam, and $I$ represent the intensity of the transmitted beam.

The absorption coefficient $\alpha$ can be determined using the following formula:

$$\alpha = \frac{1}{d} \ln \frac{100}{T(\%)} \tag{II.4}$$

where $T(\%)$ represents the transmittance, which is the quantity of transmitted light and can be directly measured by:

$$T(\%) = \frac{I}{I_0} \times 100 \tag{II.5}$$

The characterizations by UV-Visible spectrometry in transmission and reflection were performed at LRME using JENWAY 6715UV/Vis spectrophotometer, and at LPMC using a Perkin Elmer Lambda 950 spectrophotometer. The spectrophotometer works as follows: A monochromator prism located between the light source and the sample allowed for the selection and variation of the irradiation wavelength. A semi-reflecting mirror then splits the monochromatic beam into two identical beams, with one passing through the sample and the other serving as a reference. Two photodetectors located downstream to the sample and the reference quantified the transmitted light intensity for each beam. The ratio between the intensity received by the detector downstream to the sample and that received by the detector downstream to the reference led to the optical transmission of the sample (T) and to the optical reflection of the sample (T), The principle of the spectrophotometer is illustrated in figure (II.10).

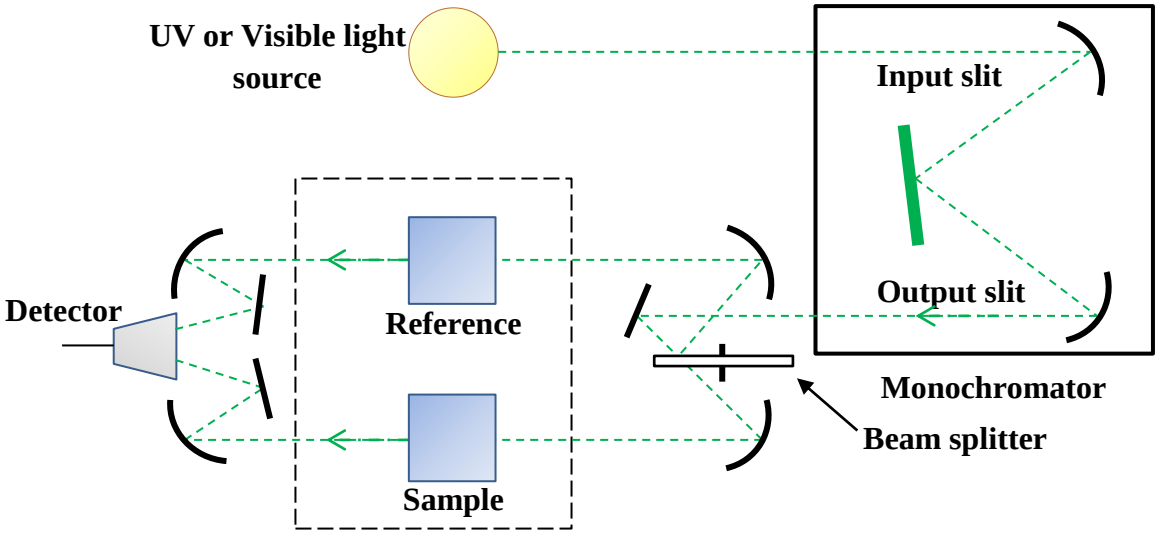


**Figure (II.10):** Elements of a spectrophotometer.

In the case of transparent thin layers, the transmission was expressed as a percentage normalized to the reference. The spectra presented in this manuscript were obtained with a scanning speed of 1200 nm/min and an acquisition resolution of 2 nm per measurement step. For the analysis of solutions, 2 to 3 milliliters were taken and poured into a 1 cm quartz cuvette. The use of quartz allowed for obtaining spectra unaffected by cuvette absorption across the entire studied spectral range. The spectra of thin layers deposited on transparent substrates were calibrated using an empty sample holder. The acquisitions made on the thin layers were performed in a spectral range from 200 to 1100 nm. By analyzing the interferences obtained from the transmission spectra, it is possible to determine various parameters including the thickness of the film, optical gap, porosity**,** and the refractive index.

### 5.4. Photoluminescence spectroscopy

Photoluminescence spectroscopy is a simple, versatile, contactless, and non-destructive method for examining the electronic structure of materials and nanostructures. PL is originated from the semiconductor's absorption/emission activity between different electronic energy levels. It happens when an electron returns from an electronic excited state to an electronic ground state, losing its excess energy in the form of a photon in a process called photo-excitation. The experimental setup of a PL instrument includes an emission monochromator, a detector, and an optical excitation source (such as a laser or a xenon lamp); the optical excitation source provides excitation photons of known energy, then these photons are directed onto the sample by an excitation monochromator. During the excitation process, the sample emits photons, which are collected by an emission monochromator and directed to the detector. The spectrometer disperses these emitted photons based on their energy, allowing their detection and analysis. A typical PL setup is illustrated in figure (II.11).

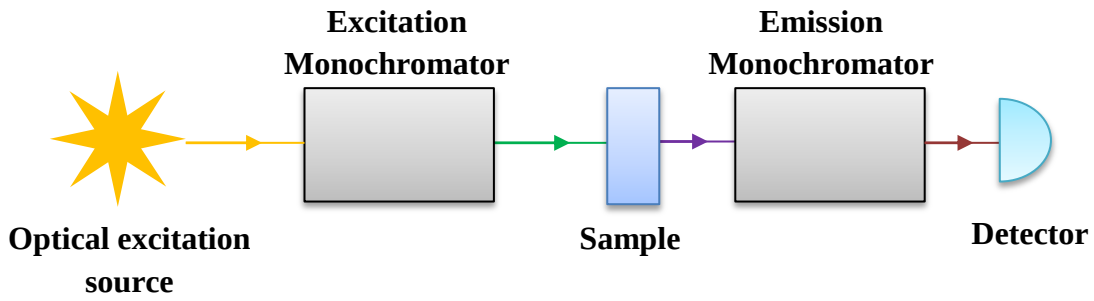


**Figure (II.11):** Schematic diagram of a Photoluminescence setup.

The electronic and optical properties, such as bandgap energy, emission wavelength, and radiative lifetimes can be extracted using data analysis parameters provided by PL spectra from the emission intensity, peak position, and peak width. The PL analysis was performed using a Perkin Elmer LS55 spectrofluorimeter equipped with a Xenon lamp.

### 5.5. Contact angle

The super-hydrophilic nature of the films was examined by assessing the contact angle of water drops of a constant volume (~ 3 µL) and an electrical conductivity of $\delta = 16 \times 10^{-6}$ S.cm deposited on the surface of the sample, before the photocatalytic activity tests. The principal of angle measurement is based on the analysis of an image coming from a CCD camera, which is a magnified and precise image of the drop without aberration. The software ImagJ can then analyze the digitized image of the drop and determine its geometric characteristics. ImageJ software measures the contact angle θ, which is the angle between the surface of the solid and the tangent to the surface of the liquid. Contact angle measurements are executed under ambient atmosphere at temperature. Figure (II.12) shows the possible different profiles of the contact angle of a water drop on the surface of a film.

A water contact angle greater than 90° specifies a hydrophobic surface whose affinity with water is low, i.e., a surface on which water tends to be repelled. Such a surface has low surface tension and lacks active chemical bonds to create hydrogen bonds with water. A surface with increased hydrophobicity has a very high contact angle. Such a surface whose contact angle is greater than 150° is commonly called super-hydrophobic. On the other hand, a contact angle less than 90° describes a hydrophilic surface whose molecular attractions between the surface and the water allow the drop to spread. Hydrophilic surfaces have a strong affinity with water, allow the creation of hydrogen bonds with water, and have high surface energy. A surface whose contact angle is less than 5° is described to be super-hydrophilic.

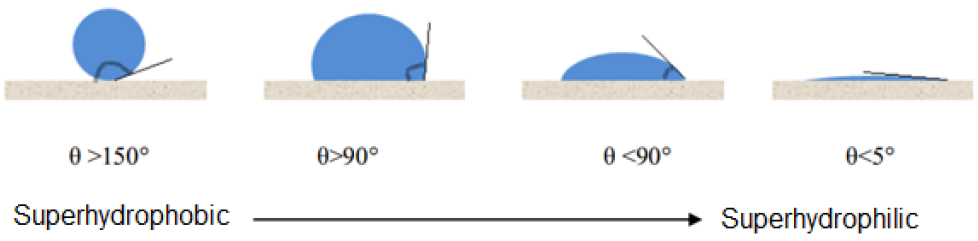


**Figure (II.12):** Contact angle of a water droplet with the surface of a solid.

### 5.6. Energy-dispersive X-ray spectroscopy

The quantitative analysis of the chemical composition of $TiO_2$ thin film samples was estimated by Energy-dispersive X-ray spectrometry (EDX), which is used in conjunction with SEM. This technique employs an incident electron beam to irradiate the studied sample. The sample emits the secondary and backscattered electrons, which leads the atoms to be ionized during this irradiation, leaving holes in the electron shells and making the atoms in a non-stable state; in order for these atoms to stabilize, electrons from outer shells will be in the inner shells, however, in order the outer shells to be at a higher energy state must some energy be lost by the atom in the form of X-rays. These X-rays emitted from the atoms are characteristic in wavelength and energy, allowing the measurement of the elemental composition of the sample. The EDX analysis were conducted at the "Centre de Recherche en Technologie des Semi-conducteurs pour l'Énergétique" in Algiers using the QUATTRO S (FEG-ESEM) scanning electron microscope equipped with a Dual EDS (60 $mm^2$) / µ-XRF coupling.

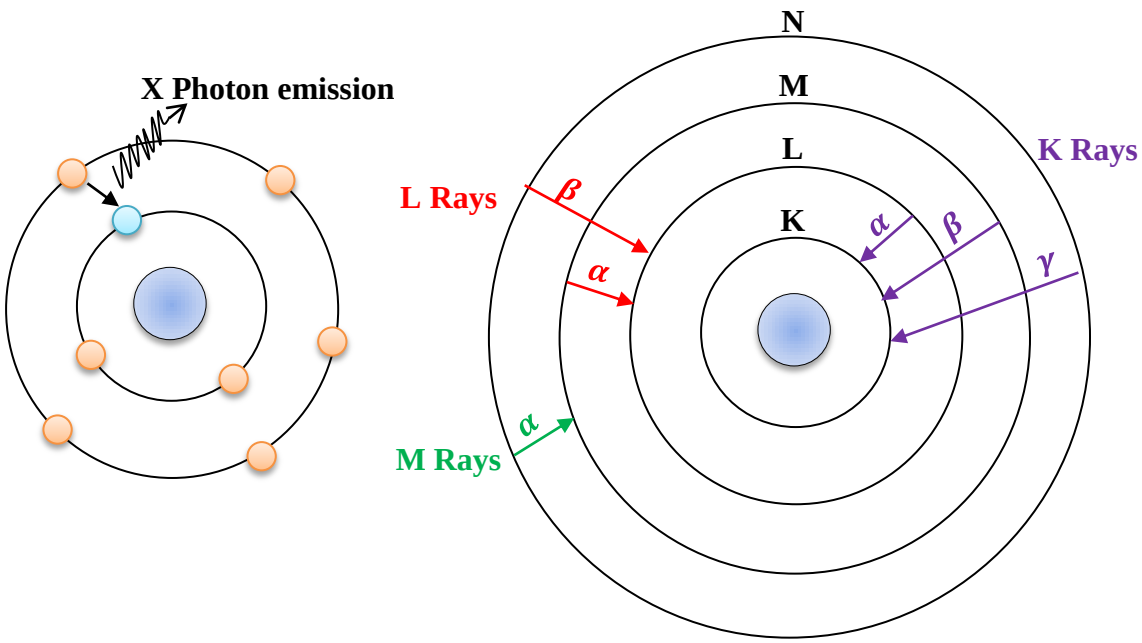


**Figure (II.13):** Principle of X-ray fluorescence of an ionized atom (a) and nomenclature of different X-ray emission lines (b) [34].

### 5.7. Four-probe measurement

The four-point probe technique is an electrical measurement method used to determine the resistivity or sheet resistance of materials, especially thin films. This method involves using four collinear probes: two outer probes for current injection and two inner probes for voltage measurement. The probes are equally spaced on the surface of the material. Current flows through the outer probes, while the voltage is measured between the inner probes, ensuring minimal influence from contact resistance, as shown in figure (II.14).

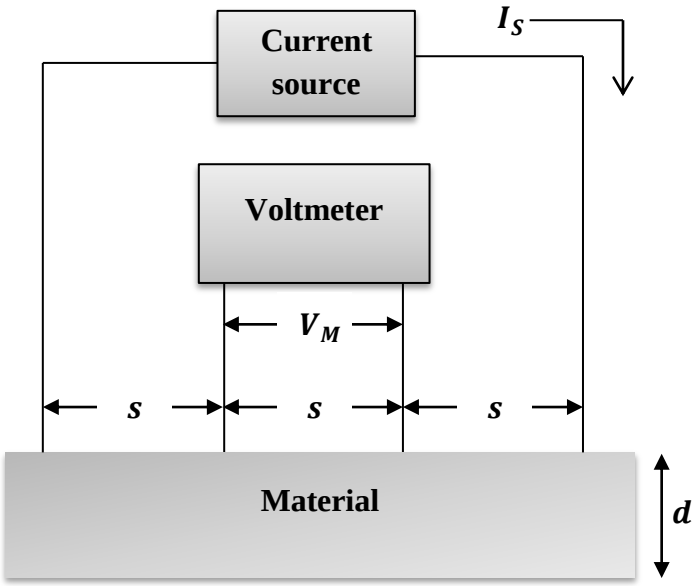


**Figure (II.14):** Four probes measurement principle.

The process involves:

- **Setup**:
  - Current is supplied through the outer probes.
  - Voltage is measured between the inner probes using an electrometer voltmeter.
- **Calculation**:
  - The sheet resistance ($R$) for thin films is calculated using:

$$R = 4.53\frac{V}{I} \tag{II.6}$$

Where $V$ is the measured voltage and $I$ is the supplied current.

### 5.8. X-ray photoelectron spectroscopy

The most widely used surface analysis technique is X-ray Photoelectron Spectroscopy (XPS), known as Electron Spectroscopy for Chemical Analysis (ESCA); this technique can be applied to a wide range of materials and supply quantitative and chemical state information from the analyzed material's surface. The average XPS measurement depth surface analysis is approximately 5 nm. Typically, XPS works by exciting the surface of a studied sample using mono-energetic Al $k_{\alpha}$ X-rays, causing the emission of photoelectrons from the surface of the sample. The energy of these emitted photoelectrons is measured using an electron energy analyzer. The intensity of a photoelectron peak and the binding energy can determine the quantity of a detected element, elemental identity, and chemical state.

The typical analysis depth of XPS surface analysis is less than 5 nm, making it better suited for the compositional analysis of thin microscale and ultra-thin layers sample features.

## 6. Photocatalytic test

### 6.1. Methylene blue

Methylene blue is an organic compound whose chemical formula is bis − (dimethylamino) −3.7 phenazathionium chloride. It is marginally soluble in alcohol and soluble in water (figure II.15);

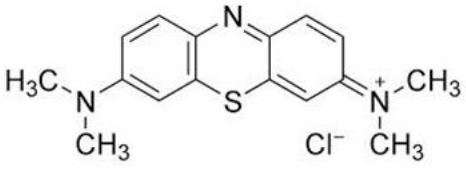


**Figure (II.15):** Molecular structure of methylene blue [34].

It is sold in pharmacies and drugstores and used in various areas:

- It serves as a colored redox indicator: its oxidized form is blue, while reduced, it is colorless.

- It is used as a histological stain—Methylene blue dyes tissue collagen blue.

- In medicine, it is frequently used as a marker to test the permeability of a structure (for example, of the uterine tubes during hysterosalpingography) to specify the path of a fistula.

- Methyl blue is sometimes used to soothe urinary infections.

- It can be used as an antiseptic in aquariums. Methylene blue is a model molecule in the Japanese standardization test proposal for self-cleaning glasses. Some characteristics are presented in the following table (II.1):

**Table (II.1):** Characteristics of Methylene Blue.

| | Raw formula | Molar Mass (g/mol) | Solubility in water (20 °C, g/L) | Fusion Temperature (°C) |
|---|---|---|---|---|
| **Methylene blue** | $C_{16}H_{18}ClSN_3S$, $xH_2O$ | 319,85 | 50 | 190 |

### 6.2. Photochemical reactor

The used photochemical reactor is designed and built in Coating, materials and environment laboratory (LRME). It consists of an open box, a magnetic stirrer, and a beaker that contains 32 mL of the colored solution. One sample measuring 2 cm x 3 cm is immersed in the polluted solution and oriented so that the side on which the thin film is positioned toward the UV lamp or the sunlight spectrum. (Figure II.16).

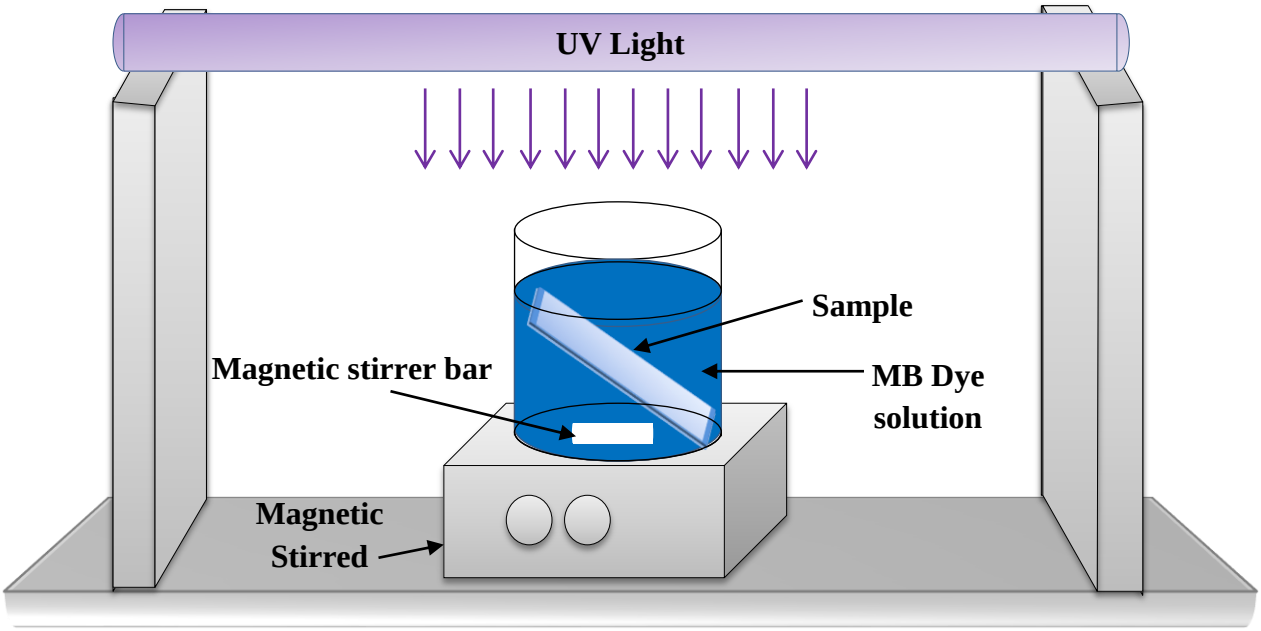


**Figure (II.16):** Experimental setup of the photochemical reactor.

The irradiation system uses the solar spectrum Philips germicidal lamp (G15T8, 15W), mainly emitting at 253 nm. The distance between the lamp and the beaker is 6.5 cm. For all photocatalytic and dye adsorption experiments, the suspension is stirred mechanically without any supply of air or oxygen. Under these conditions, dissolved oxygen is transferred from the air to the surface of the reactor, which is sufficient so that there is no deficit inside the reactor itself.

### 6.3. Measuring degradation kinetics

The concentration was determined by measuring the absorbance (optical density) of the MB solution during well-defined time intervals. The kinetics curves were drawn by measuring the absorption on samples of 3 mL of solution, using a pipette, every hour of testing. The absorbance is determined by the Beer-Lambert law. Consider a monochromatic radiation of fixed wavelength passing through a sample of thickness l cm (figure II.17).

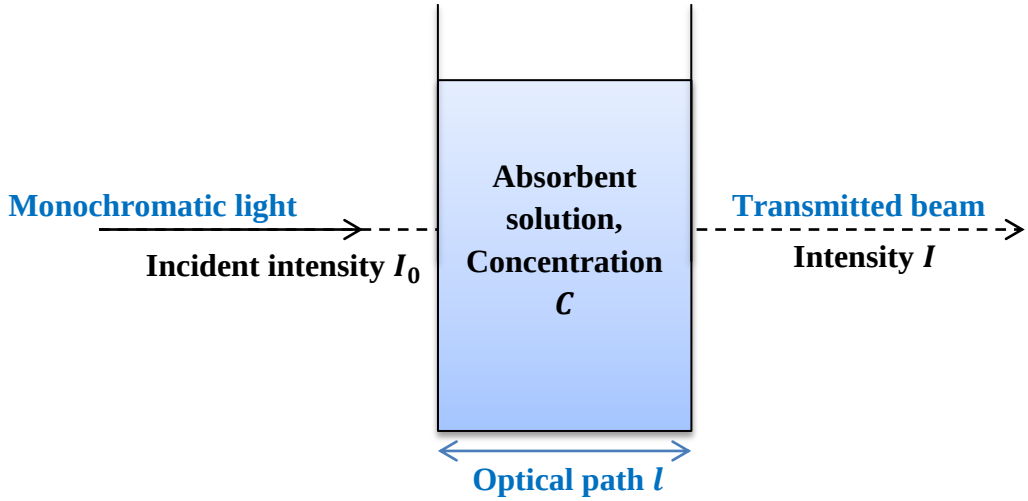


**Figure (II.17):** Light absorption.

Part of this radiation will be absorbed by the sample and part will be transmitted. According to Bouguer, Lambert and Beer the relationships that exist between $I_0$ and I; the intensity of monochromatic light passing through a medium where it is absorbed decreases exponentially [34]:

$$I = I_0 \exp -klC \qquad \text{(II.7)}$$

Where :

$I_0$: is the intensity of the incident light.

$I$: is the intensity after passing through the tank containing the solution (transmitted intensity).

$l$: is the distance crossed by the light (thickness of the tank) (in cm).

$C$: is the concentration of the solution in mol/L

$k$: is a characteristic constant of the solution.

This equation can be rewritten:

$$\log\frac{I_0}{I} = \frac{klC}{2.3} = \varepsilon lC \tag{II.8}$$

where $\log\frac{I_0}{I}$ is called absorbance (A) and $\frac{I_0}{I} = T$ is the transmission (%) We then obtain the relationship known as the Beer-Lambert law:

$$A = -\log T = \varepsilon lC \tag{II.9}$$

where A the absorbance and $\varepsilon$ the molar absorption coefficient in L.mol$^{-1}$.cm$^{-1}$.

## 7. Conclusion

This chapter provides a description of the different techniques used for the deposition of $TiO_2$ thin films and N-doped $TiO_2$ thin films and of the physical and chemical characterization techniques used in this work to determine the physical properties of the deposited thin films.

# Chapter III:
# *Nitrogen doping of $TiO_2$ films using a precursor*

## 1. Introduction

Due to its numerous advantageous properties, $TiO_2$ material has emerged as the most commonly utilized material in photocatalytic applications; these properties include its high oxidizing energy, affordability, non-toxicity, stability under light irradiation, and widespread availability [1-3]. Despite these advantageous features, $TiO_2$ has a critical limitation in absorbing visible light because of its wide optical gap ($E_g$ = 3.2 eV). Multiple methods have been employed to reduce the optical gap, one of which involves incorporating nitrogen atoms into the lattice of $TiO_2$ host materials [15-18]. Several strategies have been adopted to incorporate nitrogen atoms into the $TiO_2$ lattice, including depositing $TiO_2$ thin films using a sol-gel coating technique with nitrogen-containing precursors [23]. Therefore, it is interesting to investigate further the effect of nitrogen precursor concentration on the photocatalytic activity of $TiO_2$ thin films.

This chapter describes the preparation of Nitrogen-doped $TiO_2$ (anatase) thin films using the dip-coating sol-gel technique. The effect of variation of Nitrogen precursor concentration on the $TiO_2$ thin films on the structural, optical, electrical, and chemical composition properties, along with photocatalytic activity before and after Nitrogen introduction, was studied.

## 2. Samples preparation

The N-doped $TiO_2$ solution was prepared using the procedure outlined in Chapter II. Nitrogen atoms were introduced by adding Ammonium acetate ($C_2H_7NO_2$) as the nitrogen source to the $TiO_2$ solution and stirring until complete dissolution of ammonium acetate, resulting in a yellow transparent sol. The concentration of N was varied at different ratios (y= ($[N^{-3}]/[Ti^{4+}]$) equals 3, 8, and 12% molar ratio). Commercial glass and silicon wafer substrates were dipped in the prepared sols and withdrawn at a constant dip-coating speed of 1 mm/s; in order to increase the films' thickness, the process was repeated four times. After each deposition, the samples were dried for 10 minutes at 100 °C to evaporate solvents. Finally, the obtained films were annealed at 450 °C for 1 hour in an $N_2$ environment to increase film homogeneity and crystallization. The following Flowchart (figure III.1) describes the complete experimental procedure of preparing N-doped $TiO_2$ films.

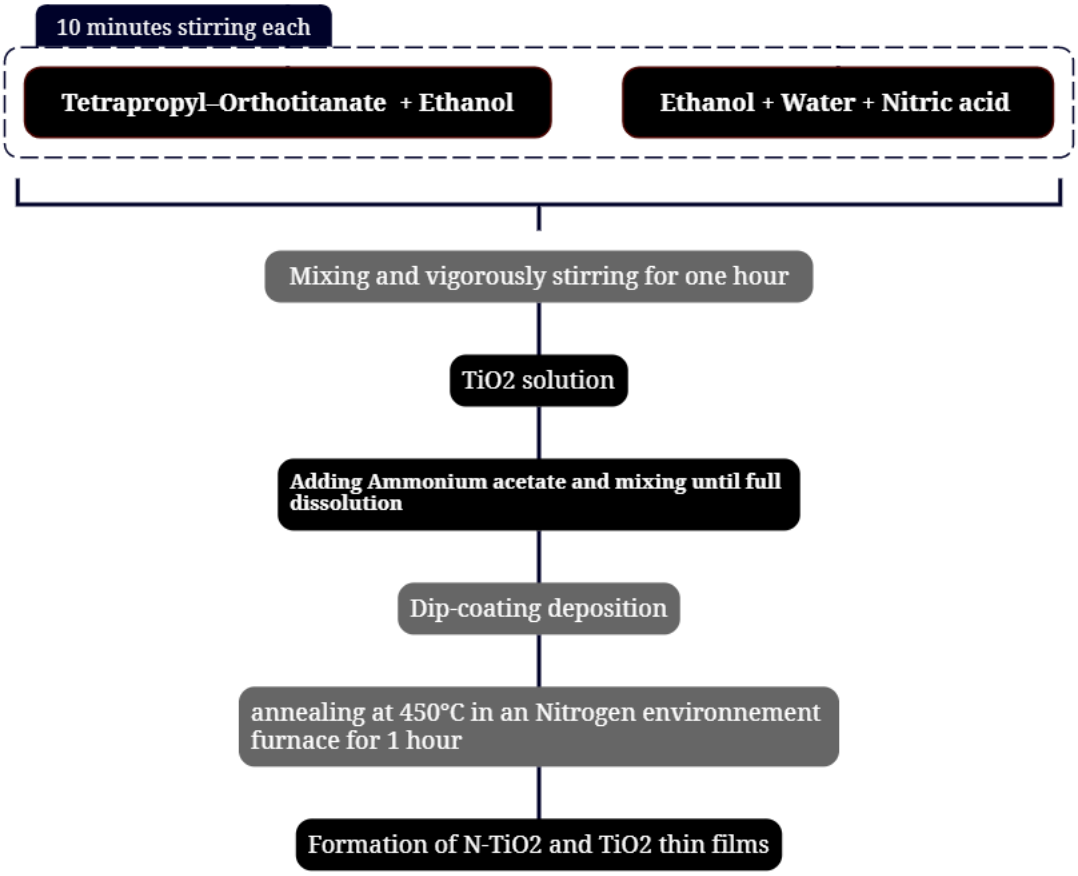


**Figure (III.1):** Flowchart of the experimental procedure of preparing N-doped $TiO_2$ films.

## 3. Characterization of the Samples

### 3.1. Structural properties

Figure (III.2) illustrates the XRD patterns of pure $TiO_2$ and N-doped $TiO_2$ thin films deposited on silicon wafer substrates at different nitrogen doping concentrations. XRD patterns show that pure $TiO_2$ and N-doped $TiO_2$ films crystallize in the anatase structure phase only, all the diffraction 2θ peaks were observed at 25.32°, 37.90°, 48.00°, 54.04°, and 62.82° corresponding to (101), (004), (200), (105), and (204) reflections respectively, which accords the JCPDS Card No.21–1272[84]; This indicates the polycrystalline nature of the prepared $TiO_2$ samples. Moreover, no additional peaks belonging to N species or its related oxides were observed, confirming the successful dissolution of the ammonium acetate into the $TiO_2$ solution to form $(Ti,N)O_2$ solution.

The crystallite size, dislocation density, microstrain, and lattice parameters (a and c) are determined based on the tetragonal structure of the $TiO_2$ anatase phase in the space group I41/amd (141).

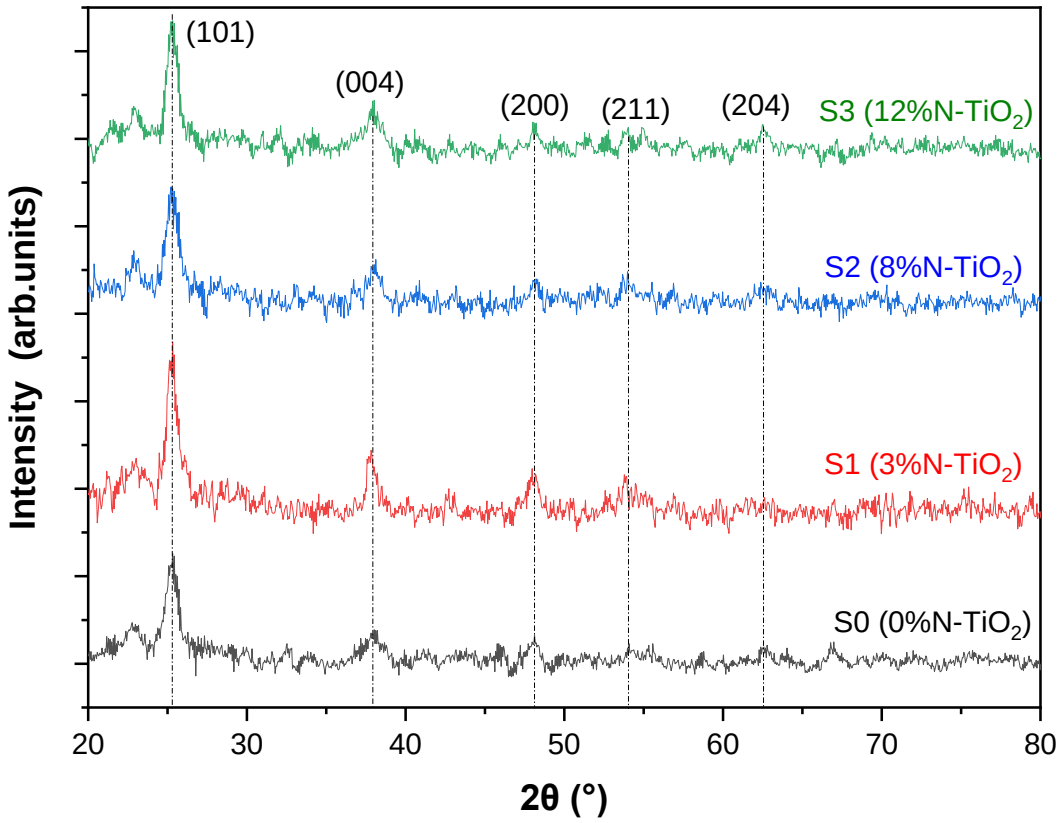


**Figure (III.2):** XRD patterns of $TiO_2$ and N-$TiO_2$ thin films deposited onto silicon wafers substrates with various N concentrations.

The crystallite size of the deposited samples is estimated using the full width at half maxima of the peak (FWHM) of the most intense diffraction lines (see figure (III.3)). It can be estimated using Scherrer's formula as follows [85]:

$$D = \frac{0.9\lambda}{\beta \cos\theta} \qquad \text{(III.1)}$$

Where $D$ represents the crystallite size (nm), $\lambda$ represents the wavelength of X-ray (nm), $\beta$ stands for the full width at half maxima of the peak (FWHM) in radians and $\theta$ is the Bragg's angle (rd.).

This calculation method generally gives lower values than the real values due to the defects and internal stresses in the deposited thin films [86].

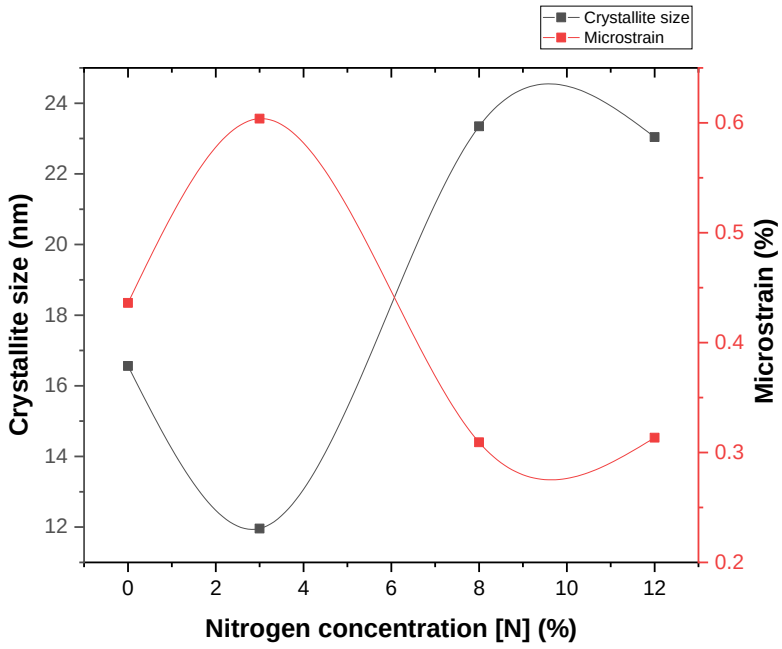


**Figure (III.3):** Crystallite size and microstrain of $TiO_2$ and N-$TiO_2$ thin films deposited onto silicon wafers substrates with various N concentrations.

We notice two patterns of variation in the crystallite size values. In the first pattern, we notice a decrease in the crystallite size when the nitrogen precursor concentration is 3% (S1), which may result from replacing larger radius lead Ti ions with smaller radius N ions. In the second pattern, we notice a considerable increase in the crystallite size when the nitrogen precursor concentration is greater than 3% (S2 and S3 samples). The increase in the crystallite size indicates an increase in nucleation sites caused by the rise of the deposited material. Also, to form large grains, the tiny grains are absorbed by large grains (coalescence step) [87, 88].

The Microstrain values of the $TiO_2$ and N-$TiO_2$ thin films are calculated by using the formula [89]:

$$\varepsilon = \frac{\beta}{4\tan\theta} \qquad \text{(III.2)}$$

Where $\beta$ is the full width at half of the maximum intensity, $\varepsilon$ is the uniform microstrain and $\theta$ is the Bragg's angle (rd.). The variation of the microstrain is illustrated in figure (III.3).

The Tetragonal system lattice parameter values can be calculated using the $(hkl)$ parameters and the interplanar spacing $d$ using the following formula [90].

$$\frac{1}{d^2} = \frac{h^2 + k^2}{a^2} + \frac{l^2}{c^2} \qquad \text{(III.3)}$$

The dislocation density δ can be obtained using the crystallite size D values according to the following formula [91]:

$$\delta = \frac{1}{D^2} \qquad \text{(III.4)}$$

The experimental lattice parameters c/a ratio of Anatase $TiO_2$ and N-$TiO_2$ thin films were determined using the equation III.3. table (III.1) shows the dislocation density and proportion of experimental lattice parameters c/a as a function of various N concentrations. It can be seen that the experimental lattice parameters' c/a ratio ranges between 2.5 and 2.53, which is in agreement with the theoretical lattice parameters' c/a proportion, which equals 2.48 [92]. It can be seen that the dislocation density decreases when increasing the nitrogen precursor concentration except in the S1 sample (3%N-$TiO_2$ sample), indicating a simultaneous movement of interstitial atoms from grain boundaries to crystallites.

Table (III.1) summarizes the crystallite size, dislocation density, microstrain, and lattice parameters (a and c) of the deposited $TiO_2$ and N-$TiO_2$ thin films.

**Table (III.1):** the crystallite size, dislocation density, microstrain, and lattice parameters (a and c) of the deposited $TiO_2$ and N-$TiO_2$ thin films.

| Samples | Crystallite size (nm) | Microstrain (%) | Dislocation density ($10^{-3}$/nm²) | Lattice parameter a (Å) | Lattice parameter c (Å) | Experimental (c/a) |
|---|---|---|---|---|---|---|
| **S0** | 16.56 | 0.436 | 3.65 | 3.773 | 9.4852 | 2.514 |
| **S1** | 11.96 | 0.604 | 6.99 | 3.791 | 9.5081 | 2.508 |
| **S2** | 23.35 | 0.309 | 1.83 | 3.743 | 9.4777 | 2.532 |
| **S3** | 23.04 | 0.313 | 1.88 | 3.757 | 9.4875 | 2.525 |

### 3.2. Optical properties

#### 3.2.1. Transmission spectra

Transmission measurements were conducted to investigate the optical properties of the deposited $TiO_2$ and N-$TiO_2$ thin films. The $TiO_2$ transmission spectra (T) as a function of different nitrogen precursor concentrations are displayed in figure (III.4), and it reveals that all deposited films have a medium transmission (30%-80%) in the visible region and a broad cut-off toward short wavelengths which correspond to the absorption edge of $TiO_2$ films. The

anatase $TiO_2$ thin film transmission spectrum shows interference fringes, which designate a smooth homogenate film surface and a thickness uniformity with tiny scattering loss. It can be observed that when nitrogen precursor concentration increases, the transmission decreases. This decrease is attributed to the nitrogen doping causing defects in the $TiO_2$ lattice, which leads to an increment of photon scattering and, thus, transmission reduction.

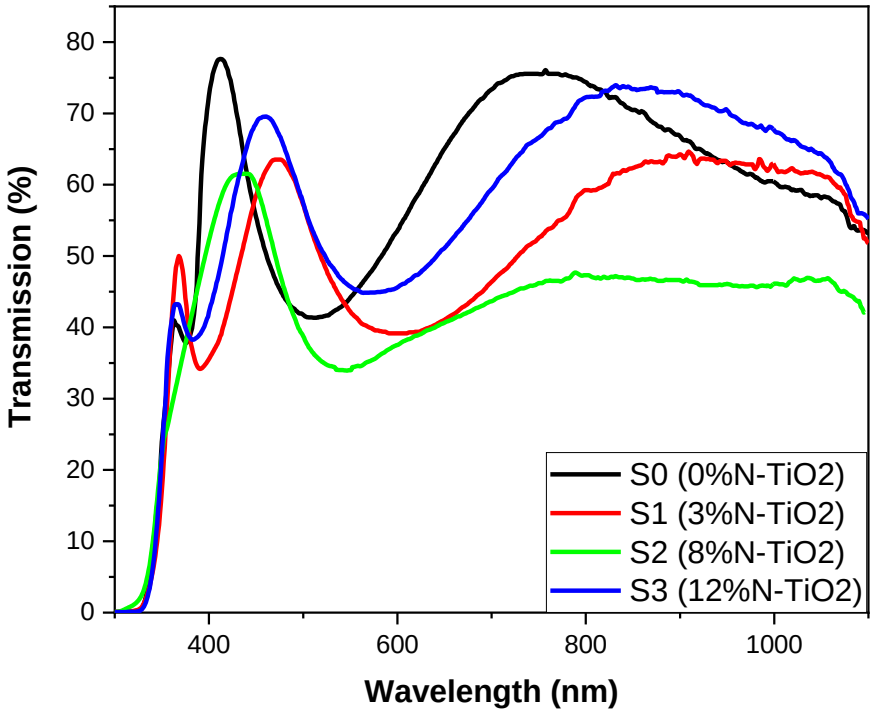


**Figure (III.4): T**ransmission spectra of pure and N doped $TiO_2$ films.

### 3.2.2. Optical Bandgap Energy

In high-energy absorption, electronic transitions occur between wide states of band to band. This phenomenon is commonly described by the Tauc law [93]:

$$(\alpha h\nu)^m = A(h\nu - E_g) \quad \text{(III.5)}$$

Where $h\nu$ represents the photon energy, $E_g$ is the optical gap, $m$ and $A$ are constants. The value of $m$ characterizes the optical type of transition and can take the values 2, 1/2 (2 for allowed direct transitions or 1/2 for allowed indirect transitions). In order to determine the nature of the transition from the films produced in this study, we will plot the curves $(\alpha h\nu)^m = f(h\nu)$. This will allow us to determine the $E_g$value [94]. The absorption edge

correlates with the valence band's electronic excitation at the conduction band and regulates the direct optical band gap value. Many experimental results and calculations on the anatase $TiO_2$ band structure assume that it has a direct band gap; however, the results of several other papers assume that it has an indirect band gap [95]. We evaluated the optical band gap energy of our pure and N-doped $TiO_2$ films using indirect transitions where their bandgap energies were calculated by the extrapolation of the linear portion of the $(\alpha h\nu)^{1/2}$ versus incident $h\nu$ photon energy curves.

Figure (III.5) show the curve of $(\alpha h\nu)^{1/2}$ versus incident $h\nu$ photon energy, and the extrapolation of its linear portions, and figure (III.6) shows the obtained indirect bandgap energies values of $TiO_2$ thin films versus different nitrogen precursor concentrations; we notice the indirect bandgap energies values is closer to the theoretical value (3.2 eV) of the anatase $TiO_2$.

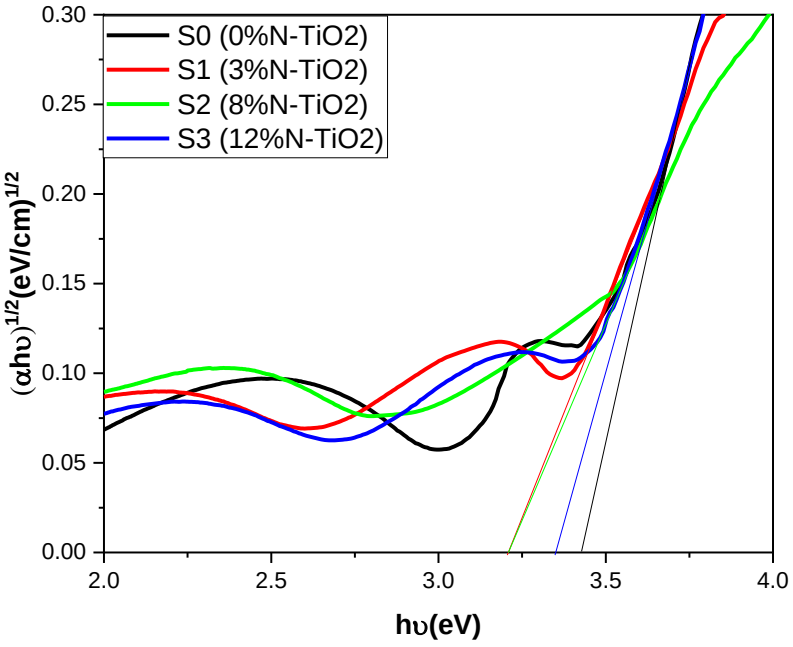


**Figure (III.5):** $(\alpha h\nu)^{1/2}$ versus $h\nu$ of $TiO_2$ thin films as a function of different nitrogen precursor concentrations and the extrapolation of its linear portions.

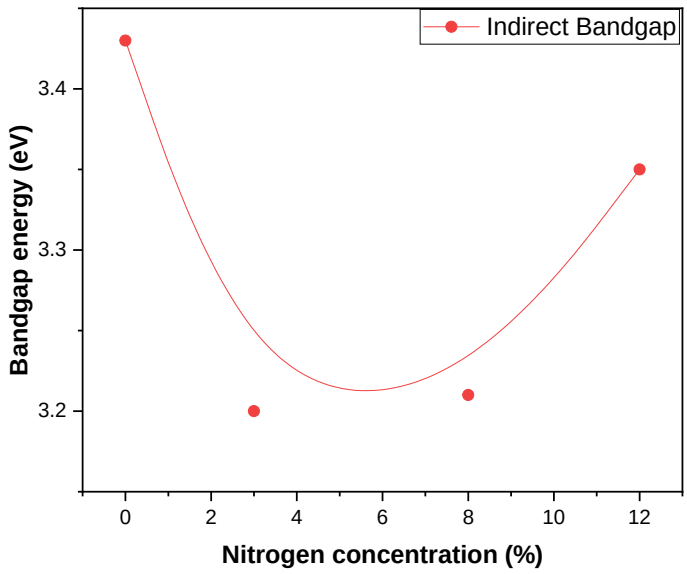


**Figure (III.6):** Indirect band gap energies values of $TiO_2$ thin films as a function of different nitrogen precursor concentrations.

It is shown that the values of the indirect optical bandgap energies of the $TiO_2$ thin films decreased after the increase of nitrogen precursor concentration, indicating successful nitrogen incorporation into the $TiO_2$ lattice. As expected after the nitrogen doping, the $TiO_2$ optical bandgap decreases, confirming the various studies that have reduced the optical bandgap energies and involved nitrogen atoms incorporation into the $TiO_2$ lattice host materials [15-18]. The underlying hypothesis for the effect of nitrogen atoms is the introduction of N2p energy states slightly above the valence band, narrowing the band gap and increasing $TiO_2$'s absorption of visible light.

### 3.2.3. Thickness, Refractive Index *n*, and Extinction Coefficient *k*

The thickness of the film can be determined using the Swanepoel method, which involves utilizing the following relation [96]:

$$d = \frac{\lambda_1 \lambda_2}{2(\lambda_1 n_2 - \lambda_2 n_1)} \tag{III.6}$$

Where $n_1$ and $n_2$ represent the refractive index of the film for the wavelengths $\lambda_1$ and $\lambda_2$, respectively, and can be calculated using the following relation [97]:

$$n = \left(N + (N^2 + s^2)^{\frac{1}{2}}\right)^{\frac{1}{2}} \tag{III.7}$$

Where $s$ represents the refractive index of the substrate, and $N$ can be obtained using the following relation [97]:

$$N = \frac{2s(T_{max} - T_{min})}{T_{max} \times T_{min}} + \frac{s^2 + 1}{2} \quad \text{(III.8)}$$

Given that $T_{min}$ is the minimum transmittance corresponding to $\lambda$ and $T_{max}$ is the maximum transmittance within the range of $T_{min}(1)$ and $T_{min}(2)$.

The thickness of the deposited $TiO_2$ and N-$TiO_2$ thin films was estimated using the envelope method [96] and equation (III.6). Its variation as a function of the nitrogen precursor concentration is depicted in table (III.2) and figure (III.7).

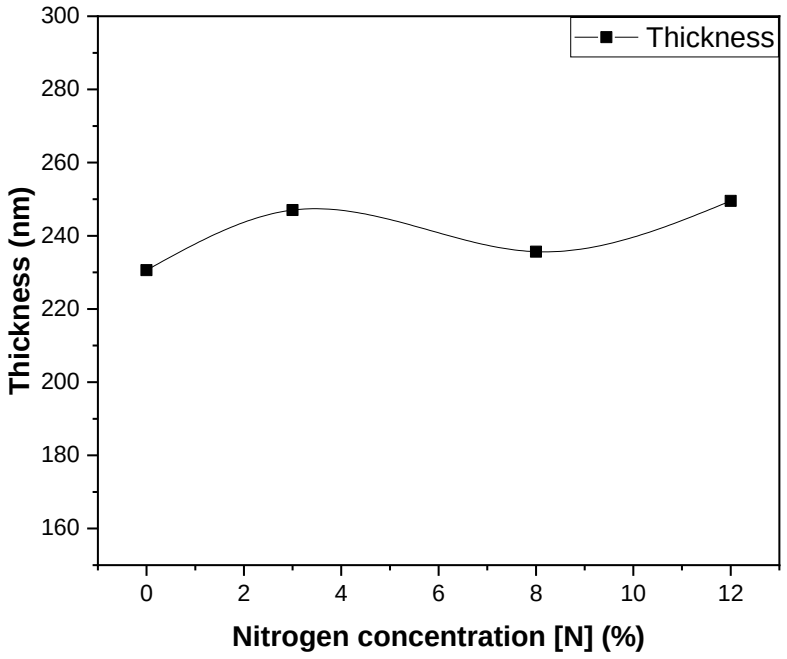


**Figure (III.7):** Thickness values of $TiO_2$ thin films as a function of different nitrogen precursor concentrations.

The film thickness ranges from 230 nm to 250 nm. As the nitrogen precursor concentration increases, the thickness also slightly increases. This slight increase can be attributed to the additional nitrogen atoms introduced during doping, as well as the increase in crystallite size, which is confirmed by X-ray diffraction analysis. However, it's important to note that the S1 sample (3%N) is an exception; despite being doped, it has the smallest crystallite size and a higher thickness compared to the undoped $TiO_2$ sample.

**Table (III.2):** Thickness values of $TiO_2$ thin films as a function of different nitrogen precursor concentrations.

| **Nitrogen precursor concentrations in $TiO_2$ films (%)** | **0** | **3** | **8** | **12** |
|---|---|---|---|---|
| Thickness (nm) | 230.62 | 247.03 | 235.66 | 249.54 |

The refractive index $n$ can be determined using equation III.7 [97], and the extinction coefficient $k$ can be calculated using the following formula [98]:

$$k = \frac{\alpha\lambda}{4\pi} \qquad \text{(III.9)}$$

The extinction coefficient and refractive index values of the pure and N-doped $TiO_2$ films were determined using equations (III.8) and (III.9). Figures (III.8) and (III.9) show the variation of the refractive index (n) and the extinction coefficient (k) as a function of wavelength, ranging from 375 nm to 800 nm. Both the refractive index and extinction coefficient decrease with increasing wavelength and then stabilize around 625 nm. This behavior is consistent with literature [99, 100]. Additionally, it can be observed that increasing the nitrogen precursor concentration has slight effect on the refractive index, which remains nearly constant. The refractive index values are lower than 2.5, the typical value of the $TiO_2$ anatase phase [100]**.**

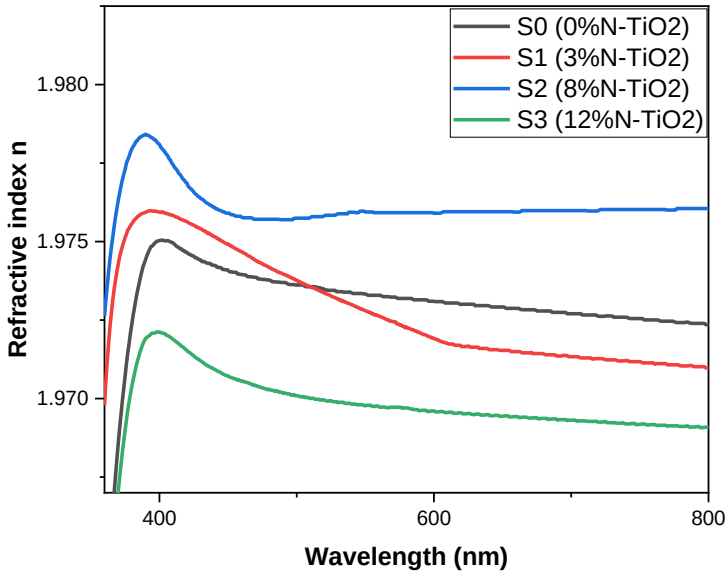


**Figure (III.8):** Variation of the refractive index ($n$) versus wavelength of nitrogen doped $TiO_2$ thin films for different concentrations.

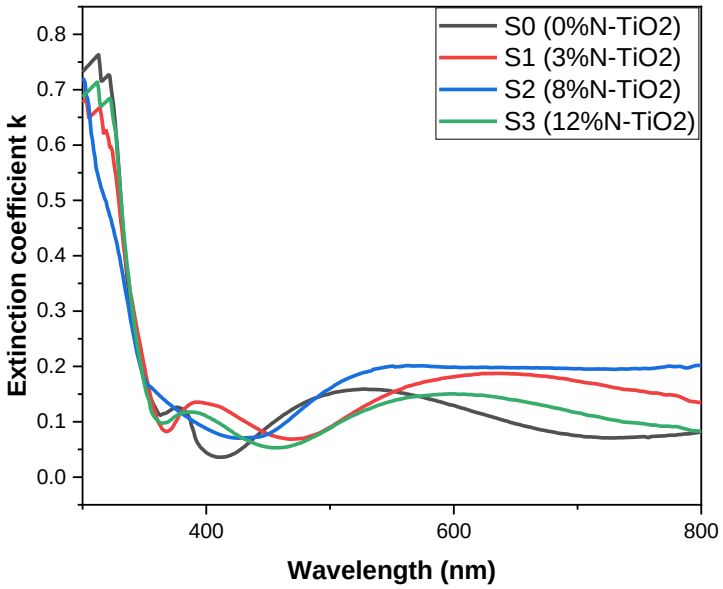


**Figure (III.9):** Variation of the extinction coefficient ($k$) versus wavelength of nitrogen doped $TiO_2$ thin films for different concentrations.

### 3.3.Electrical properties

The average sheet resistivity of $TiO_2$ thin films as a function of different nitrogen precursor concentrations is determined by using four-point probe electrical characterization technique, the average sheet resistivity was calculated using the following equation:

$$R = 4.53\frac{V}{I} \tag{III.10}$$

Figure (III.10) shows the variation of average sheet resistivity with different nitrogen precursor concentrations. As the nitrogen precursor concentration increases, there is a noticeable decrease in average sheet resistivity. This indicates that the conductivity of the deposited films improves with higher nitrogen concentrations. This result shows the potential of nitrogen doping via solution processing to enhance the electrical properties of $TiO_2$ thin films.

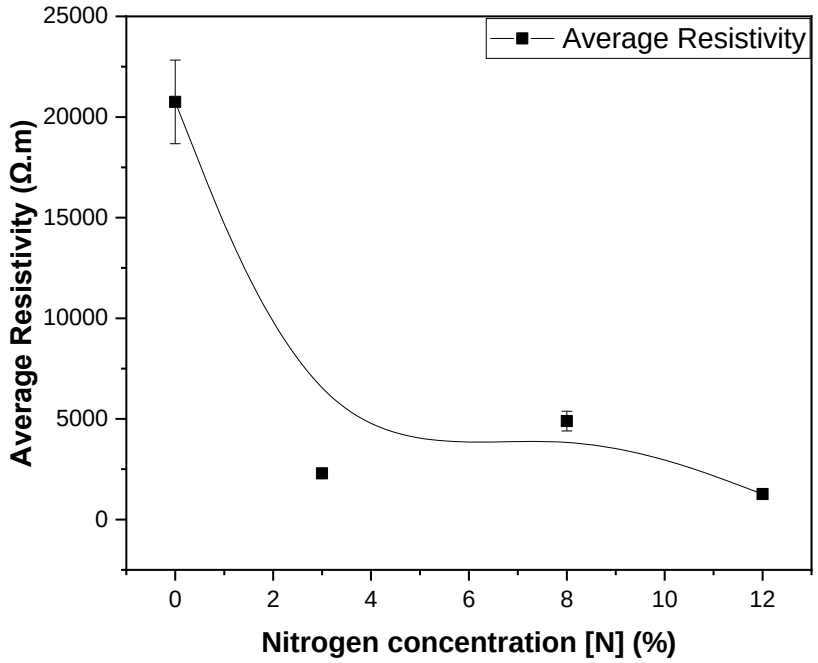


**Figure (III.10):** Average sheet resistivity of $TiO_2$ thin films as a function of different nitrogen precursor concentrations.

### 3.4. X-Ray Photoelectron Spectroscopy Analysis

The chemical composition of $TiO_2$ thin films as a function of different nitrogen precursor concentrations is determined by X-ray photoelectron spectroscopy surface analysis (XPS);

Figure (III.11) shows the survey XPS spectra of the deposited $TiO_2$ film samples in the whole binding energy region.

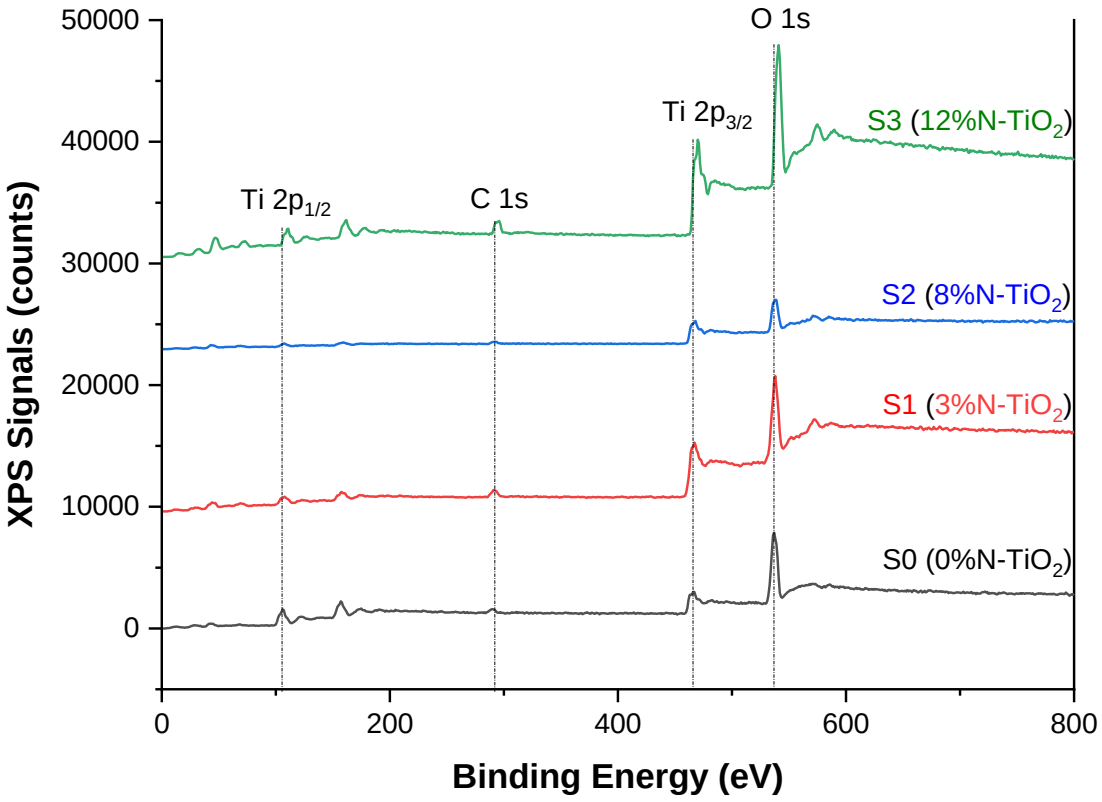


**Figure (III.11):** XPS survey scan spectra of $TiO_2$ thin films as a function of different nitrogen precursor concentrations.

We notice that pure and nitrogen-doped $TiO_2$ film samples exhibited the characteristic peaks of the $TiO_2$: a C 1s located at 291 eV bonding energy, O 1s peak located and 535 eV binding energy assigned to O-Ti-O bonds which is reported to be the typical oxide peak in Titanium dioxide [101, 102], and a Ti $2p_{1/2}$ peak a Ti $2p_{3/2}$ peak at binding energies equals 105 eV and 466 eV, respectively, which is in agreement with the reported values for anatase $TiO_2$ [101, 103]. This shows that the Ti was in an oxidized state of $Ti^{4+}$ in all samples (O-Ti-O bonds of anatase) [104, 105]. This outcome is confirmed by the binding energy distance between the peaks of Ti $2p_{3/2}$ and O 1s, which was about 71 eV; this distance remained constant when varying the Nitrogen precursor concentration in the $TiO_2$ lattice. However, in sample S3 (12%N- $TiO_2$), all its peaks Ti 2p, O 1s, and C 1s shifted towards slightly higher binding energies; this indicates a change in the chemical environment for the titanium when nitrogen precursor concentration reached 12%. This shift could be attributed to many causes, such as a

partial decrease of the titanium cations linked with the formation of oxygen vacancies in the structure and the Titanium bonding to lower electronegative species when compared to oxygen, such as the Ti-N bonds formation within the $TiO_2$ lattice, or a change in the electronic affinity of the 12% nitrogen-doped $TiO_2$ film. The N 1s peak, which corresponds to interstitial N (at 402 eV) or substitutional N (at 396–398 eV) or any Nitrogen corresponding peaks were not detected on the surface of any nitrogen-doped $TiO_2$ sample, indicating the hypothesis of the unsuccessful nitrogen doping into the $TiO_2$ lattice, or the nitrogen diffusion into the $TiO_2$ film since the XPS surface analysis maximum depth detection is 5 nm.

## 4. Photocatalytic Activity

The effect of Nitrogen doping on the deposited $TiO_2$ film's photocatalytic performance has been evaluated under the previously mentioned experimental conditions in Chapter II: Section 6. Figure (III.12) displays the variation of the MB dye solution concentration degradation D (%) under irradiation of pure and N-doped $TiO_2$ films, which was evaluated by the following equation:

$$D(\%) = \frac{C_0 - C}{C_0} \times 100 \qquad \text{(III.11)}$$

where $C_0$ is the initial concentration before irradiation at $t$ = 0 min, and C is the concentration after a certain irradiation time.

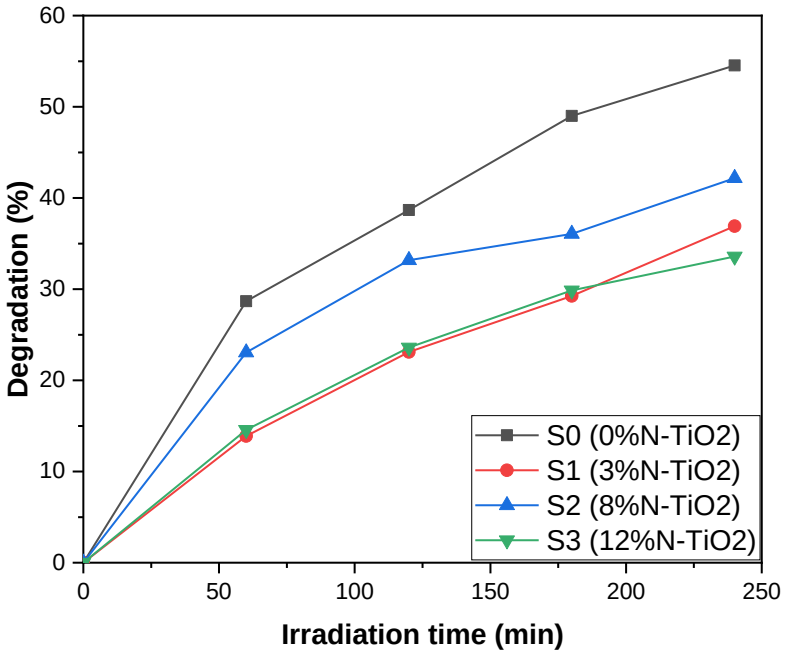


**Figure (III.12):** Degradation of Methylene blue dye as a function of the UV-light exposure time for different concentration of N-$TiO_2$ films.

The reaction rate constant of pure and Nitrogen-doped $TiO_2$ films has been determined based on the well-known pseudo-first order reaction equation [106]:

$$-\ln\frac{C}{C_0} = k_{app}t \qquad \text{(III.12)}$$

Figure (III.13) displays -ln($C/C_0$) *versus* time plots. The corresponding reaction rate constant $k_{app}$ values are summarized in table III.3.

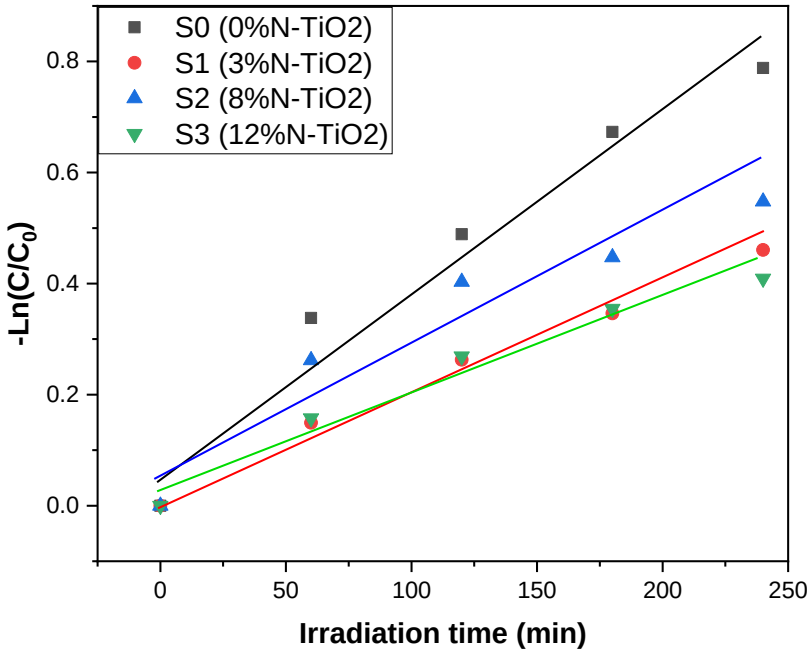


**Figure (III.13):** Corresponding plots for reaction rate constant $k_{app}$ of N-doped $TiO_2$ films.

It can be seen that the undoped $TiO_2$ thin film (S0) is more efficient in neutralizing MB dye solution compared to other N-doped $TiO_2$ samples, indicating that Nitrogen doping induces a negative influence on the photocatalytic activity of the deposited $TiO_2$ films. One explanation for such discrepancies is the unsuccessful nitrogen doping into the $TiO_2$ lattice, as confirmed by the XPS analysis, which showed no sign of nitrogen energy peaks. However, this is not a definite explanation, taking into account that XPS analysis mostly analyses only certain depths of the film's surface. Another explanation to be worth considering is that N-doped $TiO_2$ thin films in this experiment were deposited onto soda lime glass (SLG), as Wanatabe et al.[107] found that when annealing, an amount of sodium (Na) atoms diffuses into $TiO_2$ film from SLG during the deposition process. As a result, electron-hole recombination centers are formed. Moreover, the oxygen vacancy can be occupied by the presence of a Na atom with a single electron in its outer shell created by $N^{3-}$ doping (positive charge deficiency when replacing $Ti^{4+}$) which can induce the electron-hole recombination centers, hence inducing a drastic decrease in the photocatalytic degradation rate of MB dye as shown by the photocatalytic results.

**Table (III.3):** Corresponding reaction rate constant values $k_{app}$ of N-doped $TiO_2$ films.

| **Nitrogen precursor concentrations in $TiO_2$ films (%)** | **0** | **3** | **8** | **12** |
|---|---|---|---|---|
| **$k_{app}$ ($10^{-3}$ $min^{-1}$)** | **3.34** | **2.07** | **2.4** | **1.75** |

## 5. Conclusion

In this chapter, transparent $TiO_2$ thin films doped with different percentages of N precursor were successfully prepared and investigated using the dip-coating sol-gel process. X-ray diffraction analysis confirmed the $TiO_2$ anatase phase, with an increase in crystallite size as nitrogen precursor concentration increased. UV-visible analysis indicated a decrease in band gap energy with increasing nitrogen precursor concentration. Moreover, increasing nitrogen precursor concentration contributed to enhancing the electrical properties. Furthermore, XPS surface analysis revealed no signs of nitrogen corresponding peaks, indicating the unsuccessful nitrogen incorporation in the $TiO_2$ lattice. Also, we found that increasing nitrogen precursor concentration has a negative effect on photocatalytic activity, which is attributed to the use of a soda lime glass substrate, causing Na ions to diffuse to the deposited film, in light of these results, further additional experimental approaches are required to address this deficiency, in which we will explore in the next chapters.

# Chapter IV:
# *$N_2$ Plasma Treatment Effects on $TiO_2$ Films*

## 1. Introduction

In the previous chapter, we tried doping nitrogen atoms into the $TiO_2$ lattice by using a nitrogen source precursor in the $TiO_2$ solution, however we did not get the expected results, as shown by the XPS surface analysis, and by the drastic reduction in the photocatalytic activity. In this chapter, we tried a different approach to introduce the nitrogen atoms into the $TiO_2$ lattice, $TiO_2$ thin films were elaborated by the sol-gel spin-coating technique, then subjected to $N_2$ plasma to modify the film's surface and to introduce nitrogen atoms into the $TiO_2$ films. The structural, morphological, optical, photoluminescence, contact angle, and electrical properties of $TiO_2$ as a function of the nitrogen plasma treatment pressure were examined. The effect of nitrogen gas pressure on the methylene blue's visible light photocatalytic degradation was also investigated.

## 2. Samples preparation

The process of preparing the $TiO_2$ deposition solution, is mentioned in details in Chapter II. The $TiO_2$ thin film deposition was accomplished using spin-coating; the spinning speed was around 3000 rpm for 30 seconds. Subsequently, the deposited samples were heated at 100 °C for a few minutes to remove residual organic materials and remnant solvents. Finally, the deposited films were annealed at 450 °C for 1 hour to improve the film's homogeneity and crystallization.

The deposited $TiO_2$ thin films were treated with $N_2$ plasma at three different conditions of gas pressures. A vacuum system ensures a based pressure of $2.10^{-5}$ mbar by evacuating the treatment chamber. The $N_2$ gas was introduced into the treatment chamber by corresponding working pressures P1=$1.2\times10^{-2}$ mbar, P2=$1.9\times10^{-2}$ mbar, and P3=$2.5\times10^{-2}$ mbar. The discharge's power density was fixed at 6 W/cm$^2$, and the treatment took 30 minutes. The complete protocol describing the experimental procedure is in figure (IV.1)

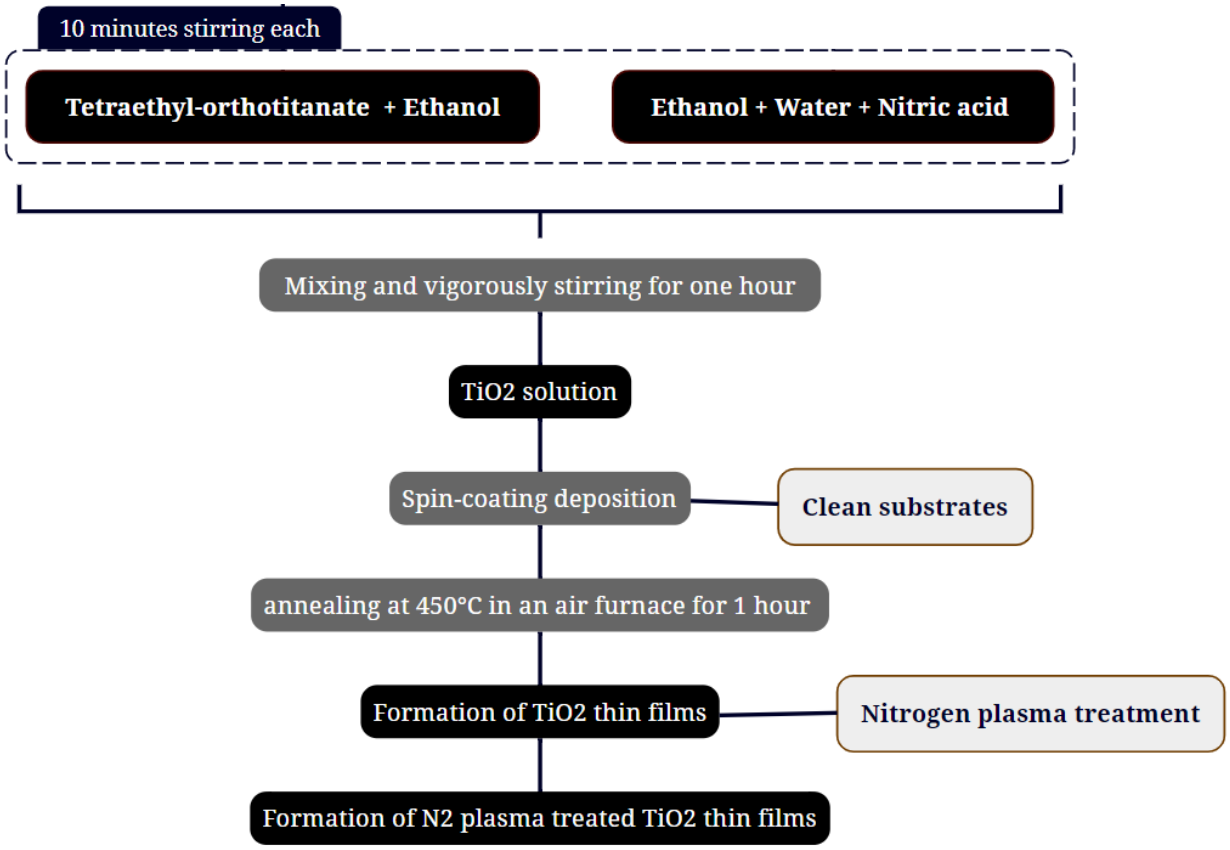


**Figure (IV.1):** Flowchart of the experimental procedure of preparing $TiO_2$ thin film and $N_2$ plasma-treated $TiO_2$ films.

## 3. Characterization of the Samples

### 3.1. Structural properties

Figure (IV.2) shows the X-ray diffraction patterns of the deposited pure $TiO_2$ and $TiO_2$ treated with $N_2$ plasma thin films at different working pressures. Multiple reflections, corresponding to (101), (004), (200), (105) and (211) planes are identified at $2\theta$=25.6°, 38.3°, 48.8° 54.9° and 62.5°, respectively; which accords the standard reference code (01-021-1272) PDF database, which assigns the films to the $TiO_2$ anatase phase in tetragonal structure, certifies of the formation of polycrystalline films. The $TiO_2$ anatase phase in a tetragonal structure is known to have high photocatalytic activity and is widely used in various applications [108].

The crystallite size, microstrain, dislocation density, and lattice parameters (a and c) are calculated based on the tetragonal structure space group I41/amd (141) of the $TiO_2$ anatase phase.

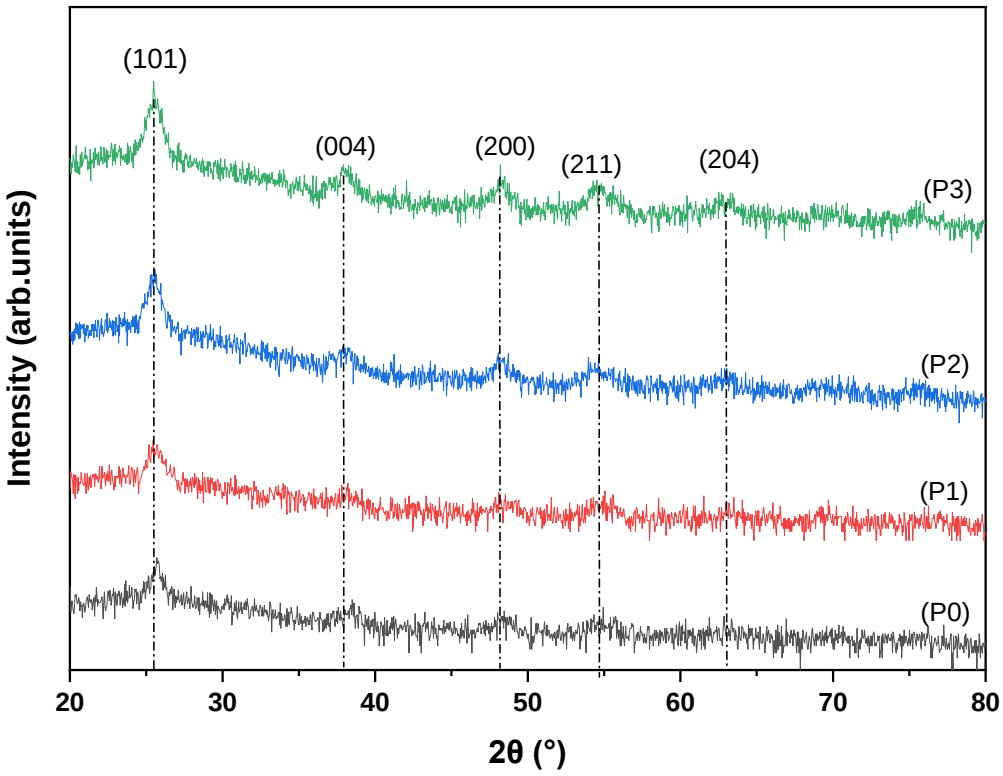


**Figure (IV.2):** X-ray diffraction patterns of $TiO_2$ thin films as a function of various $N_2$ gas flows.

The crystallite size and the microstrain values were estimated using the Scherrer formula (equations (III.1) and (III.2)). Figure (IV.3) displays the variation of the crystallite size and microstrain of pure $TiO_2$ thin film and $N_2$ plasma-treated $TiO_2$ films as a function of various $N_2$ gas flows.

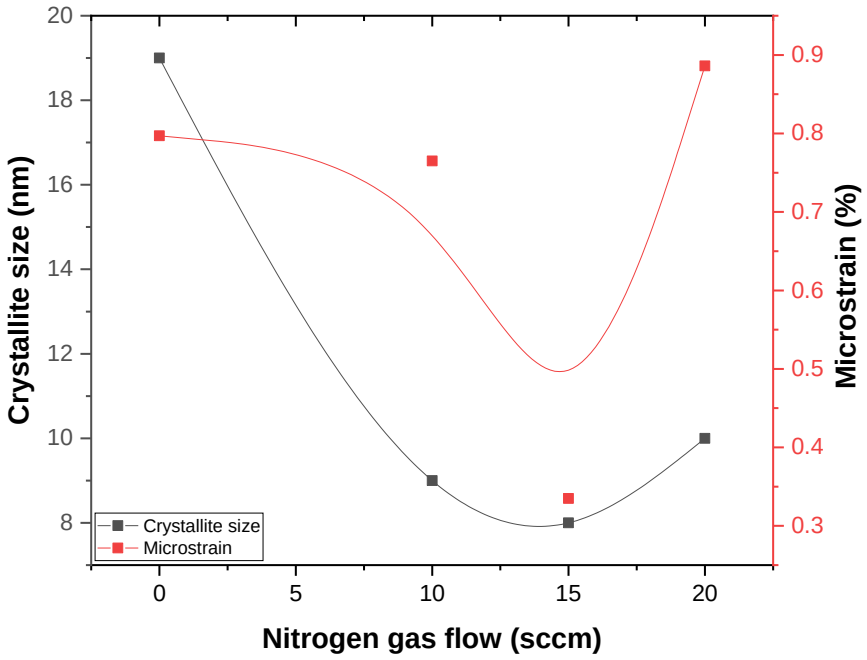


**Figure (IV.3):** Crystallite size and Microstrain values of $TiO_2$ thin films as a function of various $N_2$ gas flows.

We notice that when nitrogen working pressure is increased, the intensity and width of the XRD lines increase, indicating a reduction in the crystallite size and an increase in the microstrain. As for the P3 sample (20 sccm $N_2$ gas flow), the crystallite size decreases from 19 nm to 10 nm; on the other hand, the microstrain increases from 0.78% to 0.89%.

The experimental lattice parameters c/a ratio and the dislocation density of pure $TiO_2$ thin film and $N_2$ plasma-treated $TiO_2$ films were calculated using the equations (III.3) and (III.4). Table (IV.1**)** shows the dislocation density and the ratio of experimental lattice parameters c/a as a function of various $N_2$ gas flows. The lattice parameters (reported in table IV.1) showed a slight impact from the $N_2$ plasma treatment, and the experimental c/a ratio decreased from 2.53 to 2.51, which accords with the theoretical value of 2.48 [92]. The shift of the (101) diffraction line at a lower angle after the $N_2$ plasma treatment and the increase of dislocation density can be attributed to the relaxation of the residual stress induced by the nitrogen ions' bombardment of the films and their incorporation into the $TiO_2$ structure. The reduction in crystallite size and the increase in microstrain may impact the transport and recombination of charge carriers, which are essential factors in the photocatalytic activity. Additionally, the

changes in lattice parameters may affect the band gap energy, which is a critical factor in the photocatalytic activity of $TiO_2$.

**Table (IV.1):** Structural parameters of pure $TiO_2$ and $N_2$ plasma-treated $TiO_2$ thin films.

| Samples | Lattice parameters (Å) | $\frac{c}{a}$ | Crystallite size (nm) | Microstrain (%) | Dislocation density ($nm^{-2}$) |
|---|---|---|---|---|---|
| **P0** | a= 3.697 — c=9.384 | 2.53 | 19 | 0.797 | 0.002 |
| **P1** | a= 3.753 – – c=9.384 | 2.50 | 9 | 0.765 | 0.012 |
| **P2** | a= 3.718 – – c=9.360 | 2.51 | 8 | 0.335 | 0.015 |
| **P3** | a= 3.718 – – c=9.360 | 2.51 | 10 | 0.886 | 0.010 |

### 3.2. Morphological properties

To investigate the surface roughness and morphology of pure $TiO_2$ and $N_2$ plasma-treated $TiO_2$ films, we used atomic force microscopy (AFM). An AFM two-dimensional image of the deposited $TiO_2$ samples was recorded, and it is shown in figure (IV.4). We used Gwyddion software [109] in order to quantitatively characterize the surface roughness of pure $TiO_2$ thin film and $N_2$ plasma-treated $TiO_2$ films, the output data are presented in table (IV.2).

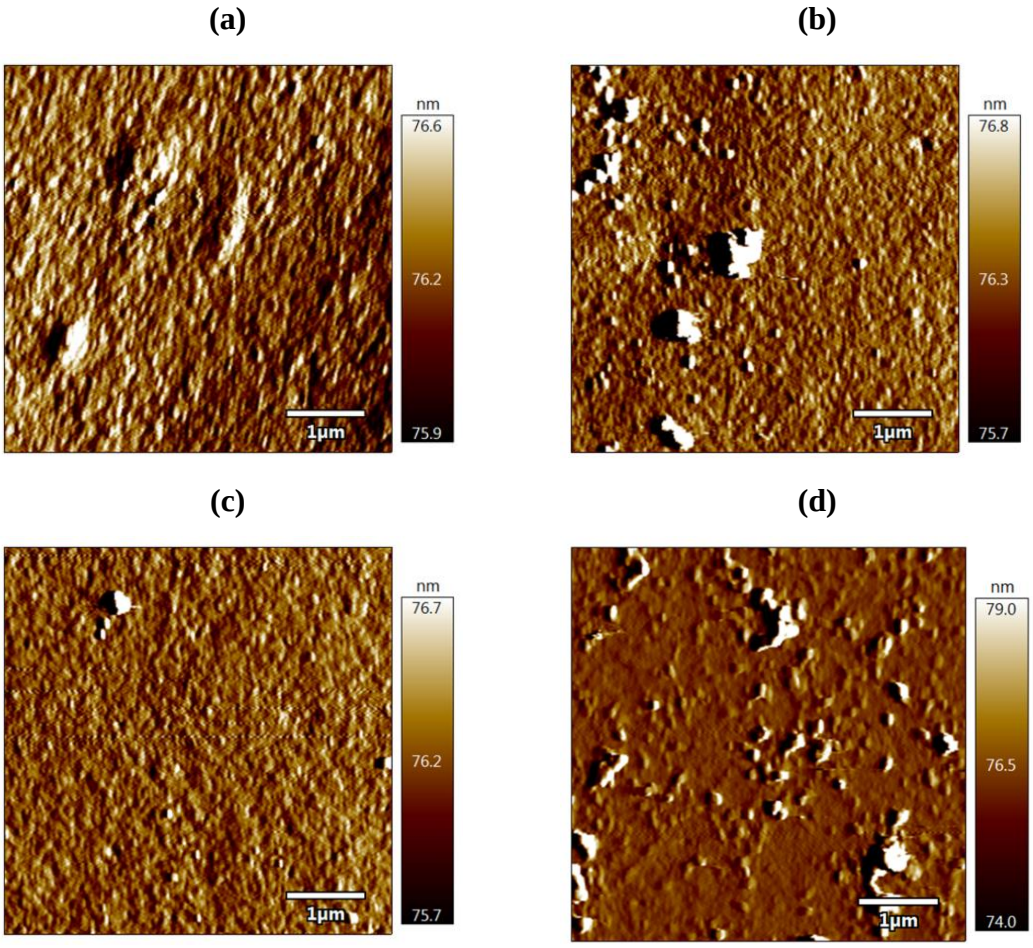


**Figure (IV.4):** AFM images of pure $TiO_2$ thin film (a) and $N_2$ plasma-treated $TiO_2$ films at different nitrogen gas flows, P1 (b), P2 (c) and P3 (d).

All the surfaces of pure $TiO_2$ thin film and $N_2$ plasma-treated $TiO_2$ films exhibited a smooth profile, with a root mean square (RMS) less than 4 nm. It can be observed from the AFM images that the $N_2$ plasma treatment has a substantial effect on the surface morphology of the $TiO_2$ samples. The AFM image analysis results showed that the $TiO_2$ film treated with low and high nitrogen gas flows (P1=10 sccm and P3=20 sccm) revealed a surface roughness of about 4 nm. In contrast, the P2 (15 sccm $N_2$ gas flow) sample showed the lowest roughness at around 1 nm.

The skewness values exhibited a notable difference. The pure film, P0, showed a positive skewness of 0.68, while the $N_2$ plasma-treated films (P1, P2, and P3) exhibited much higher positive skewness values, designating the presence of multiple peaks on the surface. Additionally, the kurtosis values revealed a significant increase when the $N_2$ plasma treatment occurred. The P2 sample has the highest kurtosis of about 110, followed by the P3 sample at about 37 and the P1 sample at 61.

On the other hand, the pure film P0 has a kurtosis value of 0.423, indicating a significantly smoother surface. The distinct nanostructure of the films, together with their roughness, may result in light scattering and modification of the surface wettability. As a result, these factors could affect the films' photocatalytic degradation properties by providing more catalytically active sites on the surface.

**Table (IV.2):** RMS, kurtosis, and skew values of $TiO_2$ thin films as a function of various $N_2$ gas flows.

| Samples | RMS (nm) | Kurtosis | Skew |
|---|---|---|---|
| **P0** | 2 | 0.42 | 0.68 |
| **P1** | 4 | 60 | 6.88 |
| **P2** | 1 | 110 | 6.22 |
| **P3** | 4 | 37 | 4.93 |

### 3.3. Optical properties

#### 3.3.1. Transmission and Reflection spectra

Figure (IV.5) illustrates the UV-visible transmission and reflection spectra of the deposited $TiO_2$ thin film and $TiO_2$ treated by $N_2$ plasma thin films. On all the spectra, two regions can be seen, a region of transparency and a region of strong absorption. In the transparency region the spectra have interference fringes due to various reflections between the film/air and film/substrate interfaces. These interferences fringes are linked to the thickness and the refractive index of the films.

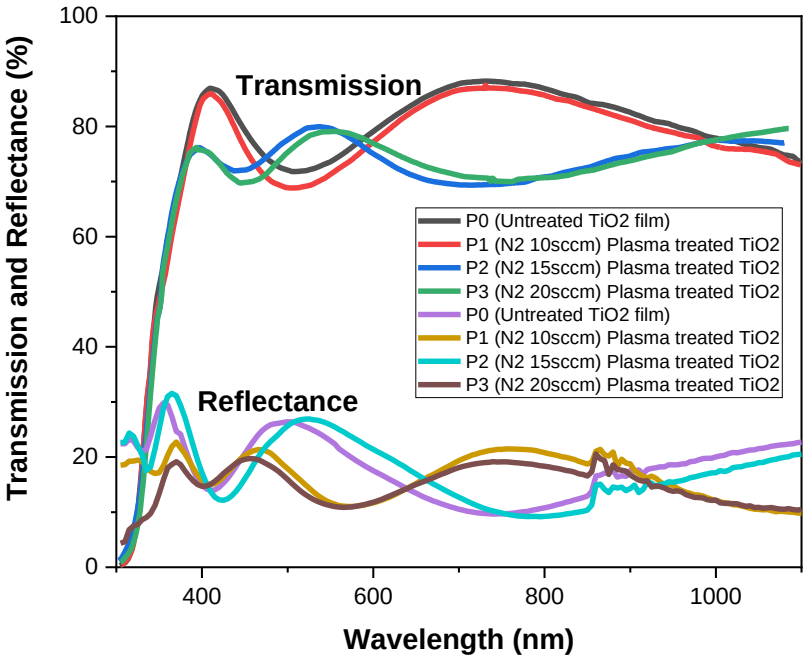


**Figure (IV.5):** UV-visible transmission and reflectance spectra of pure $TiO_2$ and $N_2$ plasma-treated $TiO_2$ thin films with a wavelength of 300-1100 nm.

We notice when the nitrogen flow reaches 20 sccm, the transmission of the sample decreases to 79% and the interferences fringes shift towards higher wavelengths. This shift mostly due to the incorporation of nitrogen atoms into the $TiO_2$ material, caused by the nitrogen' penetration into the films during the $N_2$ plasma treatment. The second region of strong absorption is observed at wavelengths below about 370 nm. In this region, the interference fringes vanishes and the transmission drops, this outcome can be attributed to various factors. One of them, the spacing between the grating lines becomes comparable to the wavelength of light, and making diffraction occurs in multiple directions. This leads to interference patterns becoming more complicated and eventually disappearing altogether. Additionally, the material of the grating may begin to absorb some of the light, leading to a decrease in transmission.

The thickness of the deposited pure $TiO_2$ and $N_2$ plasma-treated $TiO_2$ thin films were estimated using the envelope method and equations (III.6). The thickness variations as a function of the nitrogen gas flow are depicted in figure (IV.6).

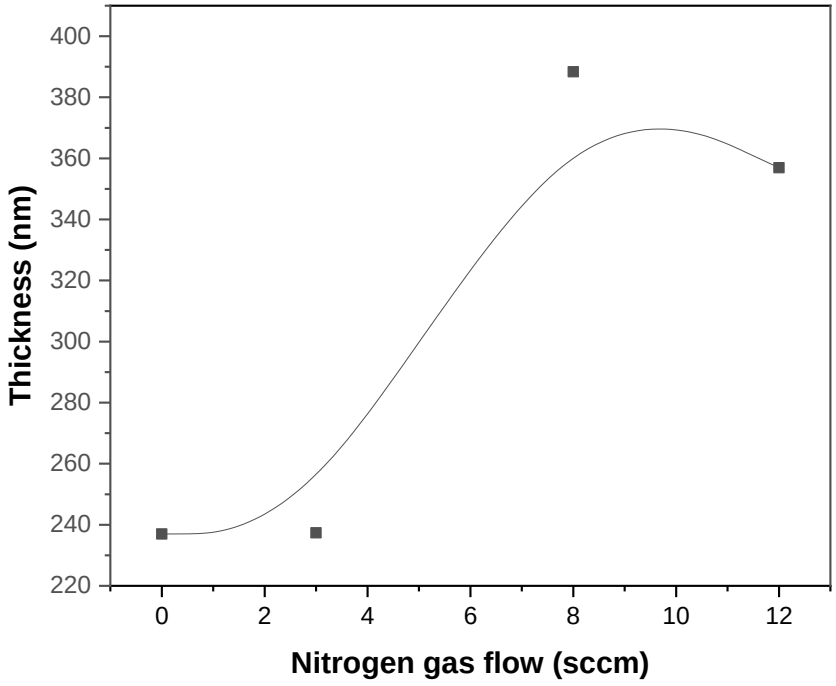


**Figure (IV.6):** Thickness values of $TiO_2$ thin films as a function of various $N_2$ gas flows.

We notice that $N_2$ plasma treatment caused an increase in the thickness of the films, likely due to the incorporation of additional nitrogen atoms during the plasma treatment.

### 3.3.2. Optical Bandgap Energy

The Tauc plot was utilized to determine the indirect band gap of the $TiO_2$ samples [110, 111]. The details of how to determine the band gap energy is mentioned in the previous chapter. Figure (IV.7) shows the band gap energy values of pure $TiO_2$ and $N_2$ plasma-treated $TiO_2$ thin films.

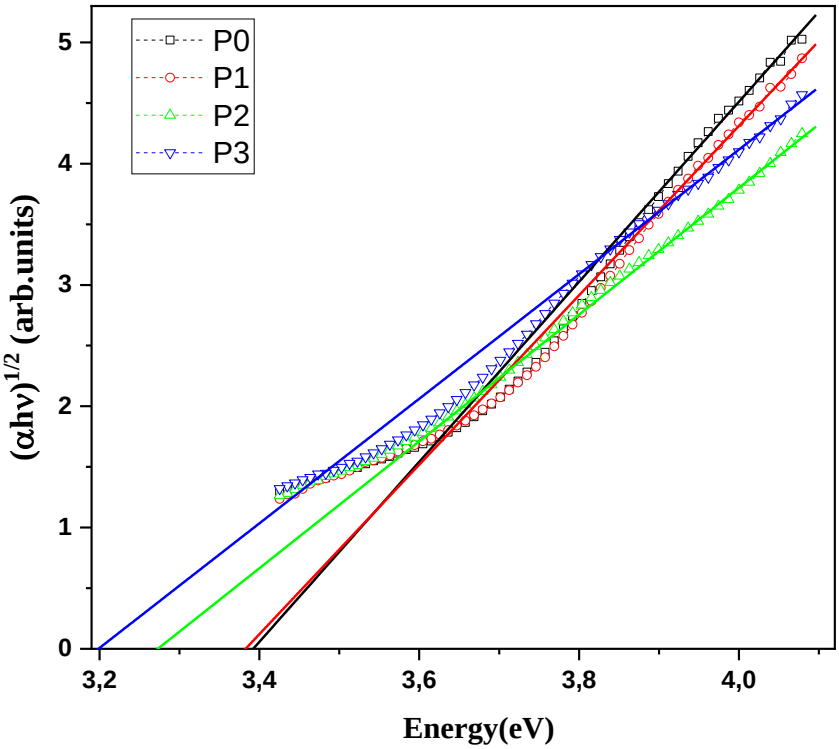


**Figure (IV.7):** Determining band gap of pure $TiO_2$ and $N_2$ plasma-treated $TiO_2$ thin films.

As can be seen, increasing the nitrogen gas flow reduces the band gap energy values from approximately 3.4 to 3.2 eV. This reduction in band gap energy could be attributed to incorporating nitrogen atoms into the $TiO_2$ film.

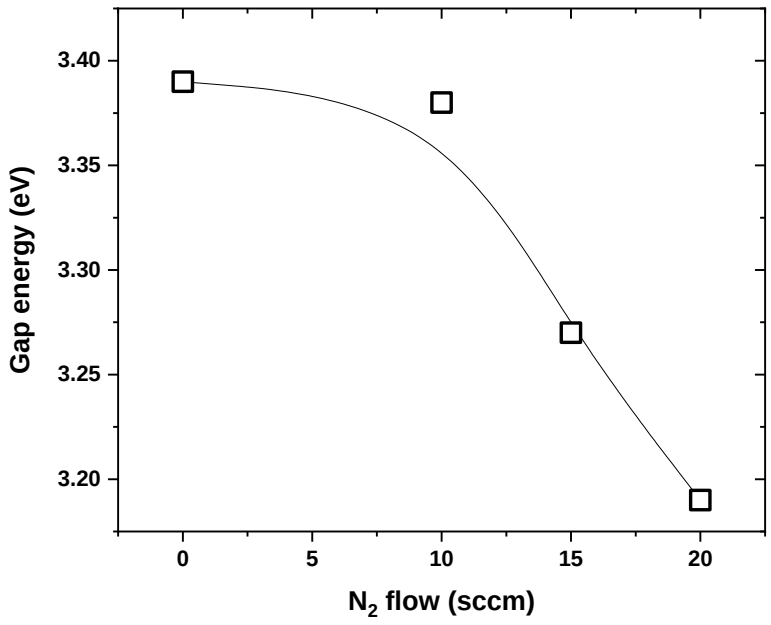


**Figure (IV.8):** Gap energy as a function of the nitrogen flow

### 3.3.3. Refractive Index *n* and Extinction Coefficient *k*

The variation of the refractive index (*n*) and that of the extinction coefficient (*k*) as a function of the wavelength of all the $TiO_2$ sample films are presented in figure (IV.9) and figure (IV.10).

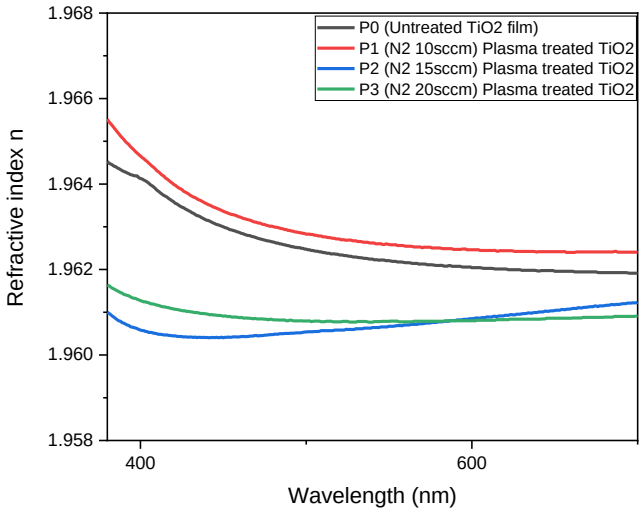


**Figure (IV.9):** Variation of the refractive index (n) versus wavelength of pure $TiO_2$ and $N_2$ plasma-treated $TiO_2$ thin films.

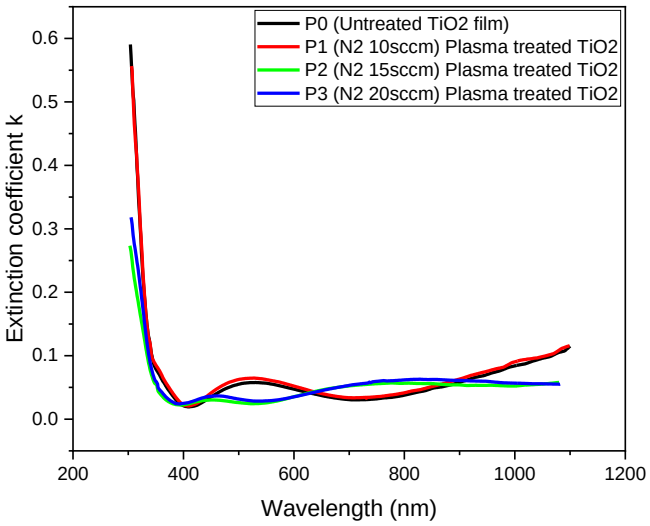


**Figure (IV.10):** Variation of the extinction coefficient (k) versus wavelength of pure $TiO_2$ and $N_2$ plasma-treated $TiO_2$ thin films.

Above 500 nm, the refractive index values become constant, and as we can see the $N_2$ plasma treatment did not affect the refractive index as it ranges between 1.96 and 1.97 (practically constant). The extinction coefficient did not exceed 0.1 in the transparency region this is attributed to the surface homogeneity of the deposited $TiO_2$ films, However, no significant effect by the $N_2$ plasma treatment on the extinction coefficient were observed.

### 3.4. Photoluminescence properties

The emission spectra of the pure $TiO_2$ thin film and the $N_2$ plasma-treated $TiO_2$ thin films are shown in figure (IV.11). These Photoluminescence spectra were captured at room temperature using an excitation wavelength of 290 nm [112], which corresponds to a photon energy of 4.27 eV, this value exceeds the band gap energy of the investigated $TiO_2$ films, as reported in literature [113]; This excitation results in the observation of emission in both the Ultra-violet and visible regions.

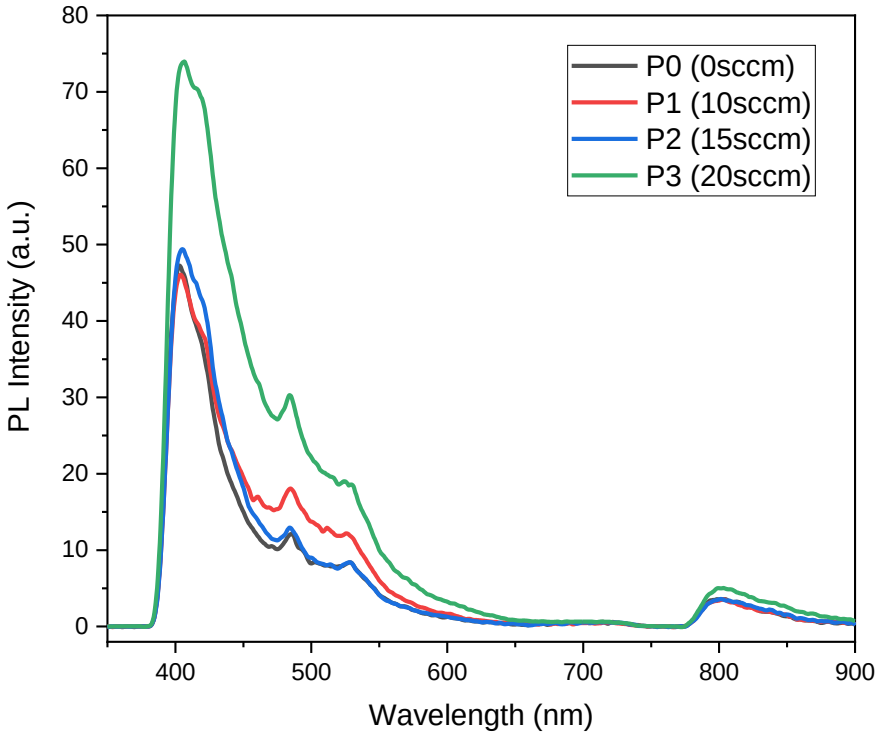


**Figure (IV.11):** Photoluminescence spectra of pure $TiO_2$ thin film and $N_2$ plasma-treated $TiO_2$ films.

Excited peaks in the spectra were seen at 403, 485, 528, and 798 nm, indicating multiple emission sources. Mainly, a high photoluminescence (PL) band is observed at 403 nm (3.08

eV) for the pure $TiO_2$ film (P0). This emission can be assigned to the indirect band-to-band recombination across the bandgap energy of the anatase $TiO_2$ thin films [114]. Additionally, a shift toward a higher wavelength (lower energy) was seen for the plasma-treated $TiO_2$ films (P1, P2, and P3), which is in agreement with the reduction in the optical band gap energy previously found by the optical measurements (figure (IV.8)). Furthermore, the three other observed peaks at 485 nm (2.55 eV), 528 nm (2.35 eV), and 798 nm (1.55 eV), corresponding to all the $TiO_2$ samples P0, P1, P2, and P3, these visible emissions are due to the movement of electrons from the defect states to the valence band of $TiO_2$ along with trapped holes [115], providing an emission in the visible region; Furthermore, the emission region at 480 nm is associated with an indirect recombination process involving defects [115].

The photoluminescence (PL) emission intensity in both the Ultraviolet and visible regions is more vital for the P3 $TiO_2$ sample, indicating an improved crystallization and increased crystallite size in the film. In contrast, the intensity is relatively lower for the $TiO_2$ untreated sample, suggesting that the lifetimes of excited electrons and holes within the $TiO_2$ film were greatly enhanced, potentially contributing to decomposition reactions with organics until the electrons and holes recombined [116]. This proposes a relationship between the photoluminescence emission intensity and the crystalline structure of the $TiO_2$ film, casting light on the potential applications of plasma treatment for improving the properties of thin films.

### 3.5. Electrical properties

To explore the effect of $N_2$ plasma treatment on the electrical properties of the $TiO_2$ thin films, we measured the average sheet resistivity values using four-probe measurements. Figure (IV.12) displays the variation of the average sheet resistivity versus nitrogen gas flow. We notice a decrease in average sheet resistivity values when nitrogen gas flow increases during plasma treatment. Specifically, the resistivity values decreased from 35 to 17 Ω.m, indicating an improved conductivity.

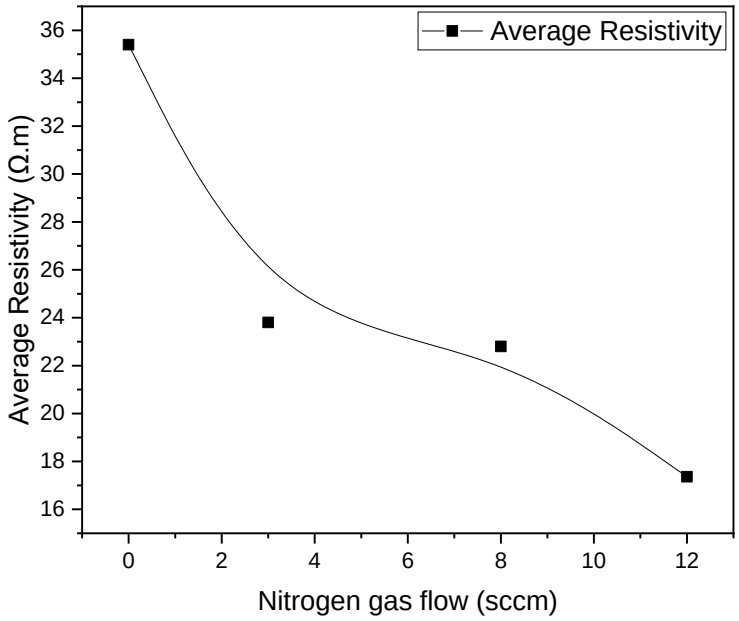


**Figure (IV.12):** Average sheet resistivity of $TiO_2$ thin films as a function of various $N_2$ gas flows.

This decrease in resistivity values can be attributed to incorporating nitrogen atoms into the $TiO_2$ films, which reduces the optical gap and enhances the conductivity. These results show the potential of $N_2$ plasma treatment as a technique for modifying the electrical properties of $TiO_2$ thin films.

### 3.6. Contact Angle

Contact angle measurements were performed on the pure $TiO_2$ films and the $N_2$ plasma-treated $TiO_2$ films to determine the effect of plasma treatment on the surface properties of $TiO_2$ thin films. The contact angle values were calculated using ImagJ software.

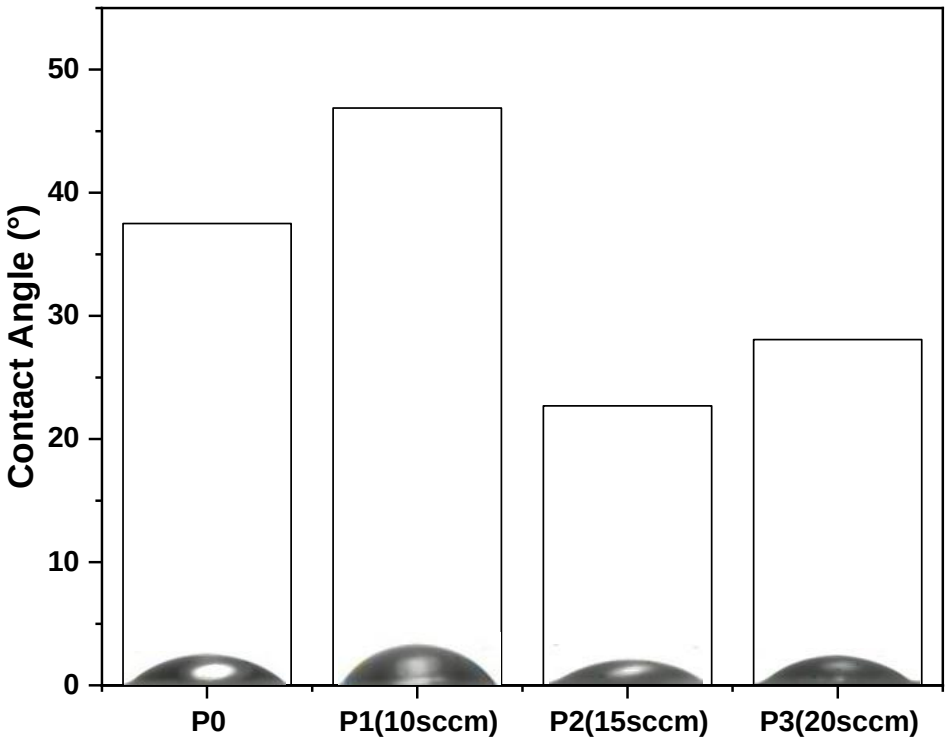


**Figure (IV.13):** Contact angle measurements of pure and $N_2$ plasma-treated $TiO_2$ thin films.

Figure (IV.13) illustrates the results of the contact angle measurements; the obtained data indicate that all $TiO_2$ samples exhibited hydrophilic properties, as indicated by the contact angles being lower than 90°. This is attributed to the high cohesive force between the water drop and the $TiO_2$ film surface [42]. The results presented in this study showed that the pure $TiO_2$ film has a more cohesive water drop shape when compared to the $N_2$ plasma-treated $TiO_2$ sample films. Consequently, the $N_2$ plasma-treated films were less wettable, as indicated by the higher contact angle of the $N_2$ plasma-treated $TiO_2$ films than the pure $TiO_2$ film.

### 4. Photocatalytic Activity

To determine the effect of $N_2$ plasma treatment on the photocatalytic activity of $TiO_2$ films, we studied the degradation of a methylene blue (MB) dye solution under visible light irradiation (figure IV.14). The photocatalytic activity measurement details were mentioned in the previous two chapters.

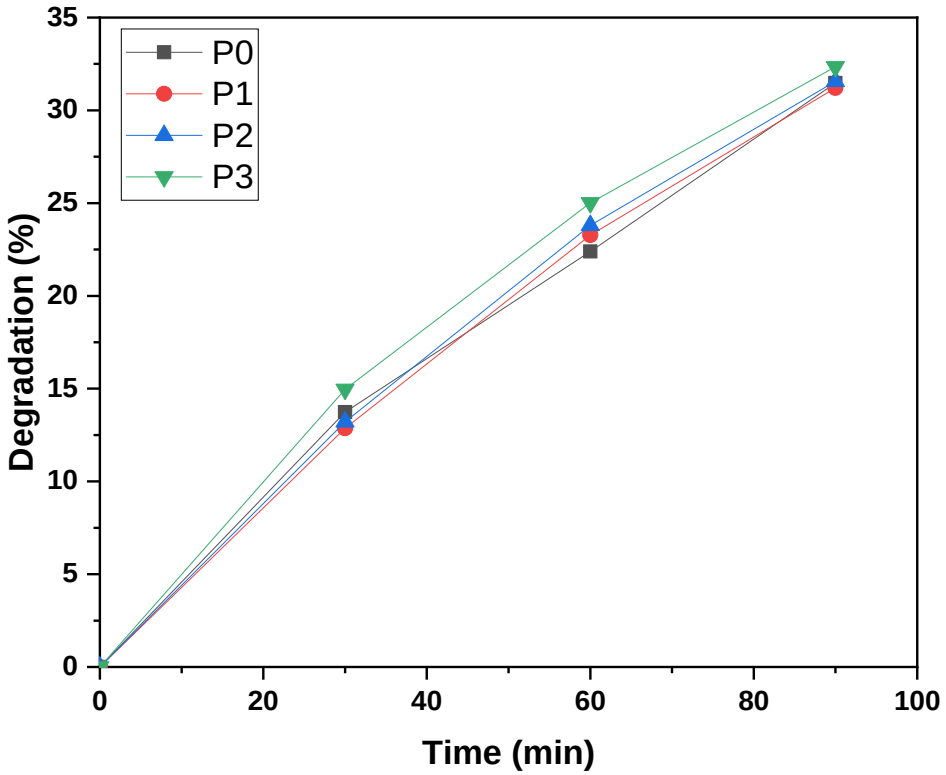


**Figure (IV.14):** Degradation of Methylene blue dye as a function of the Visible-light exposure time of pure $TiO_2$ thin film and $N_2$ plasma-treated $TiO_2$ films.

Throughout the irradiation period, we observed continuous decomposition of the MB solution for the pure and the $N_2$ plasma-treated $TiO_2$ thin films. Nevertheless, there is a slight improvement in the photodegradation of the MB dye solution for the $N_2$ plasma-treated $TiO_2$ films compared to the pure $TiO_2$ film. This shows that the $N_2$ plasma treatment affects the $TiO_2$ film, either by the incorporation of nitrogen atoms into the $TiO_2$ films or by modification of the surface morphology as confirmed by the AFM scans and the decrease of crystallite size and rises of boundary grain as confirmed by XRD analysis.

However, nitrogen atoms in the $TiO_2$ structure can cause a reaction between the nitrogen and the oxygen molecules, formatting nitric oxide (NO). The generation of NO arises when the excited electrons, produced by the absorption of photons from the $TiO_2$ valence band, migrate

to the nitrogen dopants and subsequently transfer to oxygen molecules, leading to NO formation. Since NO is a reactive molecule, it can compete with other ROS, such as hydroxyl radicals (OH•), in reacting with organic pollutants. This competition can reduce ROS concentration and decrease the overall rate of pollutant degradation [117]. The photocatalytic reaction rate constant ($k_{app}$) was determined through the pseudo-first order reaction equation (equation (III.12) [118]. The obtained $\ln\frac{C_0}{C_t}$ plots and $k_{app}$ values for pure $TiO_2$ thin film and $N_2$ plasma-treated $TiO_2$ films are displayed in figure (IV.15). It can be seen that the highest rate constant efficiency ($k_{app}$) is observed for $TiO_2$ sample P3 (20sccm) ($k_{app}$ =0.00433 $min^{-1}$), to neutralize the MB dye solution compared to the other $TiO_2$ samples P0(0sccm) ($k_{app}$ =0.00413 $min^{-1}$), P1(10sccm) ($k_{app}$ =0.00416 $min^{-1}$), and P2(15sccm) ($k_{app}$ =0.00423 $min^{-1}$).

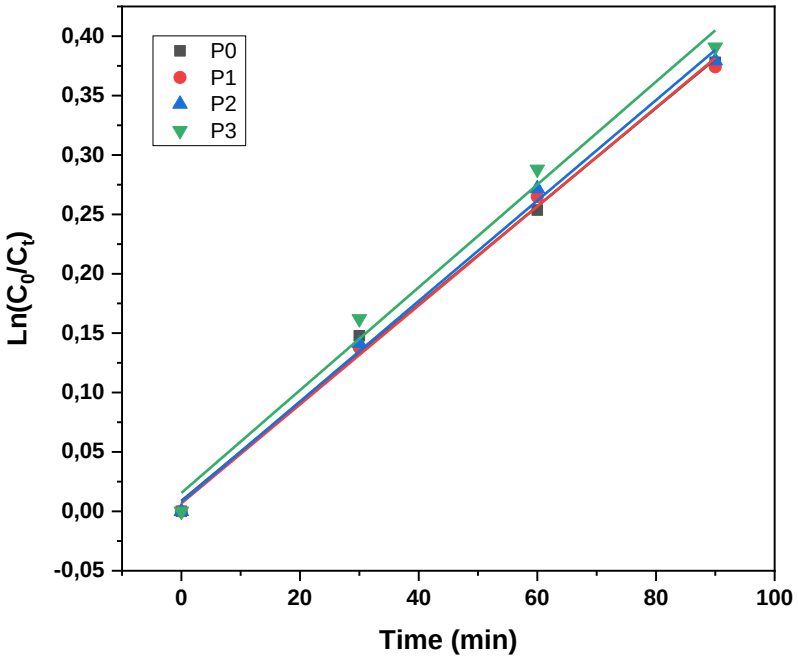


**Figure (IV.15):** Corresponding plots for reaction rate constant $k_{app}$ for pure $TiO_2$ thin film and $N_2$ plasma-treated $TiO_2$ films.

## 5. Conclusion

This chapter investigated the effects of surface $N_2$ plasma treatment on the $TiO_2$ thin films prepared via the spin-coating sol-gel technique. X-ray diffraction analysis confirmed the anatase phase of $TiO_2$ films, and crystallite size decreased as the nitrogen gas pressure increased. The AFM scans showed significant changes in the surface topography after the $N_2$ plasma treatment. Additionally, UV-visible analysis revealed a decrease in the band gap energy when increasing the nitrogen plasma pressure. Moreover, the nitrogen plasma treatment improved the photoluminescence properties of the titanium dioxide thin films. Furthermore, contact angle measurements revealed a less wettable surface formation on the nitrogen plasma-treated films, suggesting alterations in surface characteristics as confirmed by AFM scan images. However, despite these variations, only a slight enhancement in the photocatalytic activity of the $TiO_2$ films was observed when subjecting nitrogen plasma treatment, to address this resulted limitation caused by the formation of nitric oxide NO on the surface of the $TiO_2$ film, an alternative experimental approach is required to introduce nitrogen atoms into the $TiO_2$ lattice avoiding the surface treatment. In order to do that we suggest to do it inside the film by coupling TiN layer with $TiO_2$ layers, a concept we will explore in the next chapter.

# Chapter V

## *Impact of Glancing Angle Sputter Deposited TiN Thin Film on $TiO_2$ Layers*

## 1. Introduction

In the previous chapter, the photocatalytic activity results showed the low efficiency of the $N_2$ plasma treatment in introducing the nitrogen atoms into the $TiO_2$ lattice due to the formation of nitric oxides NO on the surface of the $TiO_2$ film. To address this concern in this chapter, we adopted a novel organization of bilayer TiN/$TiO_2$ thin films created by mixing two techniques, Sol-gel and DC reactive magnetron sputtering, in order to modify the surface morphology and incorporation of nitrogen atoms into the $TiO_2$ thin film lattice. The impact of the TiN layer on the physical properties and photocatalytic activity of $TiO_2$ films has been studied.

## 2. Samples preparation

The protocol for preparing the $TiO_2$ deposition solution was outlined in Chapter II. The $TiO_2$ thin film deposition was carried out using a dip-coating technique with a withdrawal speed adjusted at one mm/s, and the dipping number was 3 to control thickness. As for the preparation of the TiN/$TiO_2$ bilayer film, Firstly, we deposited the TiN layer using the D.C reactive magnetron sputtering technique on both commercial glass slides and silicon wafers inclined at tilt angle α=45° in function of the surface normal of the target. The power density on the titanium target was adjusted at 6 $W.cm^{-2}$. The power generator polarized the substrate port to achieve a polarization of -20 V. The inert gas (Ar) and the reactive gas ($N_2$) were brought into the chamber. The total working pressure was adjusted at P = 2 Pa, corresponding to 12 sccm of Ar and 3 sccm of $N_2$. The deposition was carried out at room temperature and took 5 minutes. After the TiN coating is deposited on the substrate, we deposited the $TiO_2$ layer above it by the dip-coating sol-gel processing (see figure (V.1)) ; the prepared monolayer $TiO_2$ and bilayer TiN/$TiO_2$ films were then annealed in an air furnace for 1 h at 450 °C to increase crystallization and obtain the anatase phase of $TiO_2$ material. The complete protocol of the experiments is illustrated in figure (V.2).

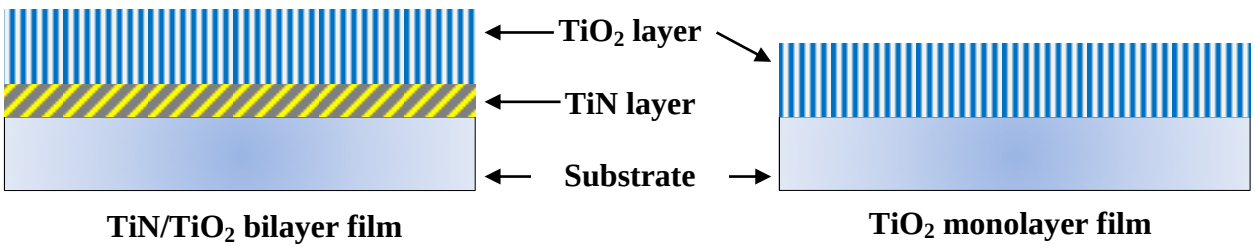


**Figure (V.1):** Description of monolayer $TiO_2$ and bilayer TiN/$TiO_2$ films.

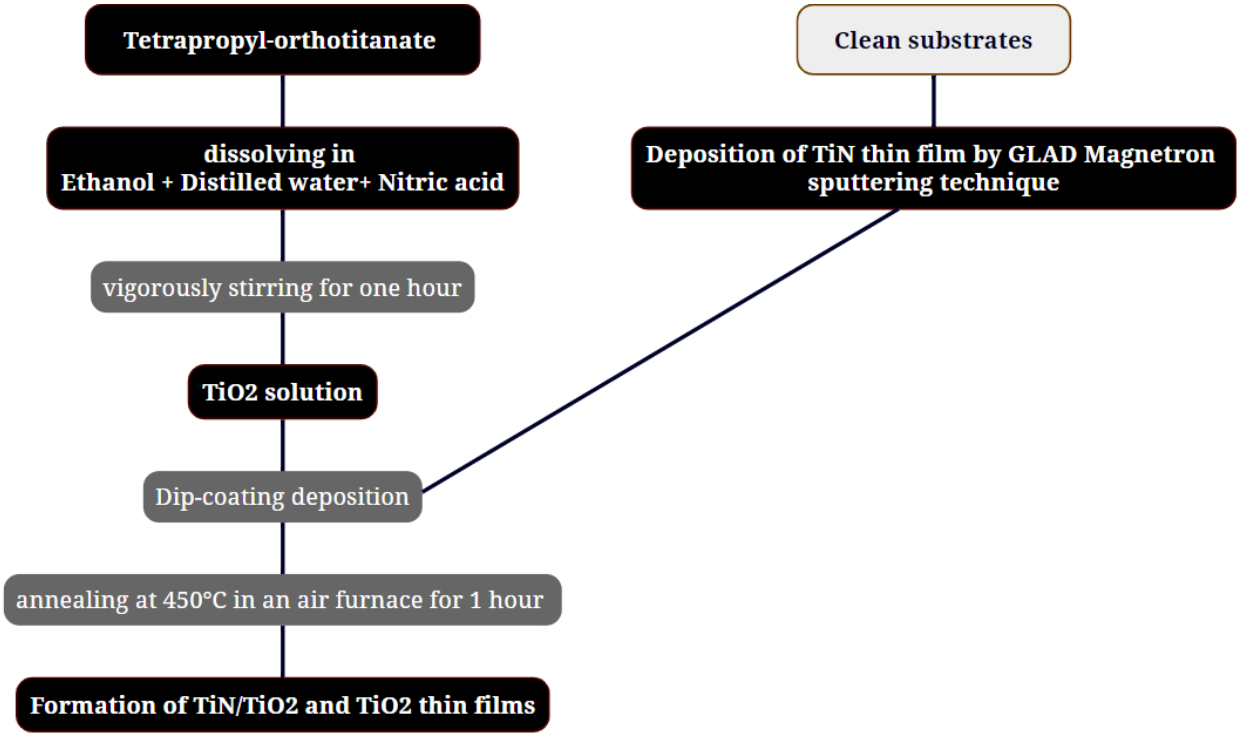


**Figure (V.2):** Flowchart of the experimental procedure of preparing monolayer $TiO_2$ and bilayer TiN/$TiO_2$ films.

## 3. Characterization of the Samples

### 3.1. Structural properties

Grazing Incidence XRD patterns of the TiN, the monolayer $TiO_2$, and the bilayer TiN/$TiO_2$ films are displayed in figure (V.3); the spotted diffraction peaks of TiN thin film were indexed to the phase cubic (Na-Cl type) structure of TiN associated with JCPDS card No. (38-1420). The TiN reflection peaks were observed at 2θ angles values of 36.6°, 42.56°, 61.73°, 74.03°, and 79.7°, which are assigned to (111), (200), (220), (311), and (222) plan reflection, respectively. For the monolayer $TiO_2$ and the bilayer TiN/$TiO_2$ films, only diffraction peaks of the anatase phase of $TiO_2$ were spotted, which is confirmed by the JCPDS card No. (21-1272). The $TiO_2$ diffraction peaks were indexed at diffraction angles 2θ values of 25.4°, 38.04°, 48.19°, 54.42°, 55.65°, 62.86°, and 75.29° which are assigned to (101), (004), (200), (105), (211), (204), and (215) reflections, respectively. We note that relatively sharp diffraction peaks of $TiO_2$ anatase grown on the TiN sub-layer compared to those deposited on soda lime glass, which means a decrease in the crystallite size. We notice no additional diffraction peaks corresponding to the nitrogen species in the bilayer TiN/$TiO_2$ film coating, which may be attributed to the low sub-layer thickness of TiN compared to the

$TiO_2$ film. The lattice parameters (a and c), the crystallite size, dislocation density, and microstrain values are evaluated based on the tetragonal structure of the $TiO_2$ anatase phase in the space group I41/amd (141) and it is shown in table (V.1).

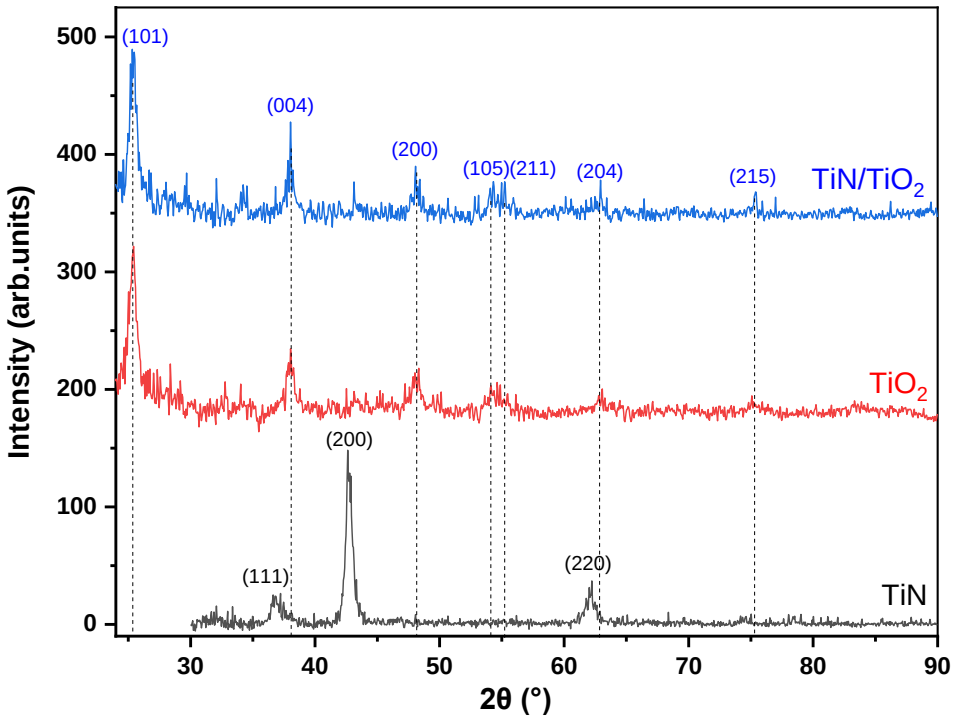


**Figure (V.3):** X-ray diffraction patterns of TiN, monolayer $TiO_2$ and bilayer TiN/$TiO_2$ films deposited on a soda-lime glass substrate [119].

As shown in table (V.1) the crystallite size decreases when depositing $TiO_2$ film on a TiN layer this outcome supports the discussion above, we notice that the calculated experimental c/a ratio of both monolayer $TiO_2$ and bilayer TiN/$TiO_2$ films in agreement with the theoretical c/a ratio of the anatase $TiO_2$ (2.48).

**Table (V.1):** Structural parameters of monolayer $TiO_2$ and bilayer TiN/$TiO_2$ films.

| Samples | Crystallite size (nm) | Microstrain (%) | Dislocation density ($10^{-3}$/nm²) | Lattice parameters (Å) | c/a |
|---|---|---|---|---|---|
| **Monolayer $TiO_2$ film** | 16.56 | 0.462 | 3.65 | a=3.7728<br>c=9.4852 | 2.514 |
| **Bilayer TiN/$TiO_2$ film** | 16.33 | 0.610 | 3.75 | a=3.77632<br>c=9.471 | 2.508 |

### 3.2. Morphological properties

The Atomic Force Microscope is used to analyze the surface topography and the roughness of the monolayer $TiO_2$, TiN and bilayer TiN/$TiO_2$ films. Accordingly, 2D (two dimensional) AFM images of the monolayer $TiO_2$, TiN and bilayer TiN/$TiO_2$ films are displayed in figure (V.4). The monolayer $TiO_2$ surface exhibits a smooth profile, with a root mean square (RMS= 1 nm) determined from the height image. The average roughness of TiN and bilayer TiN/$TiO_2$ films were 3 and 2 nm, respectively. Both films showed a homogeneous arrangement of grains. Meanwhile, its size increases with the elongated shape of the bilayer TiN/$TiO_2$ film in the range of 50-100 nm. The height images show that the surface topography of the $TiO_2$ film strongly depends on the morphological surface of the TiN sub-layer. Also, it can be seen that the surface skewness of the bilayer TiN/$TiO_2$ film is positive, which indicates the presence of numerous bumps when compared to the monolayer $TiO_2$ film. On the other hand, the surface kurtosis of the bilayer TiN/$TiO_2$ film is higher than that of the monolayer $TiO_2$ film, revealing its surface's peakedness [106]. This typical nanostructure of the bilayer TiN/$TiO_2$ film can directly influence its photocatalytic activity properties because it should positively affect the surface wettability.

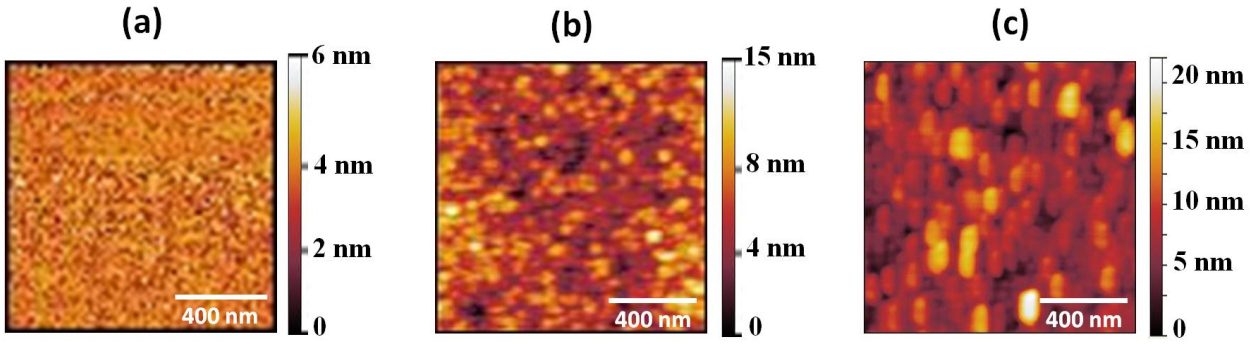


**Figure (V.4):** AFM images of (a) monolayer $TiO_2$, (b) TiN and (c) bilayer TiN/$TiO_2$ films [119].

### 3.3. Optical properties

#### 3.3.1. Transmission spectra

Figure (V.5) shows the optical transmittance of TiN, monolayer $TiO_2$, and bilayer TiN/$TiO_2$ thin films. The monolayer $TiO_2$ film showed high transmission at longer wavelengths with interference oscillations, with a sharp fall of transmittance around $\lambda$ = 325 nm toward smaller wavelengths. These interference oscillations are attributed to a good homogeneity of the films' thickness [120]. For the TiN film, we observe a lower transmission

than the monolayer $TiO_2$ and the bilayer TiN/$TiO_2$ thin films in the visible range; the high transmittance of the TiN/$TiO_2$ film compared to the sole TiN film at $\lambda$ = 362 nm can be allocated to the annealing of films at 450 °C. The transmission spectra of the bilayer TiN/$TiO_2$ film differ significantly from the monolayer $TiO_2$ film and showed a lower transmission at UV- and visible wavelengths. We observe a marked shift from the monolayer $TiO_2$ film to the visible range with the bilayer TiN/$TiO_2$ films.

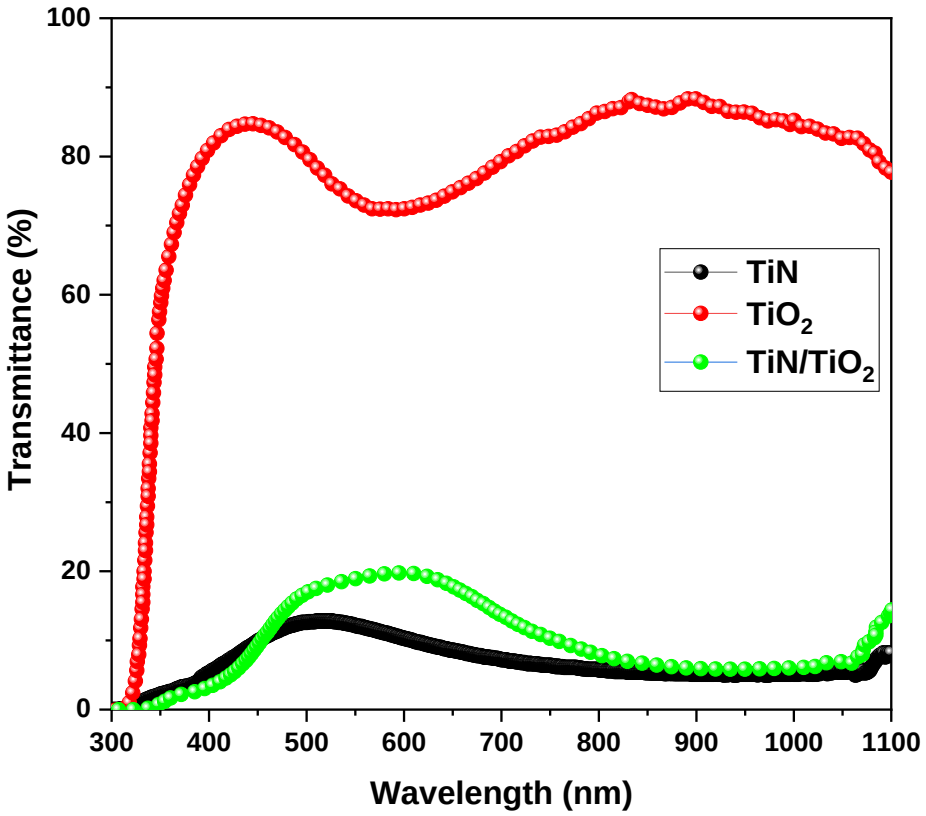


**Figure (V.5):** Transmittance spectra of TiN, monolayer $TiO_2$ and bilayer TiN/$TiO_2$ films deposited on a soda-lime glass substrate [119].

### 3.3.2. Optical Bandgap Energy

Semiconductor materials present direct or indirect bandgap energy, which their crystal structures can determine. Tauc suggests that crystalline materials tend to possess a direct bandgap energy, while non-crystalline materials often have an indirect transition nature. Sometimes, when the material exhibits a partial crystallinity or two phases, both transitions can co-exist [121, 122]. It is known that the $TiO_2$ thin films exhibits an indirect band gap, while the TiN thin films exhibits a direct band gap [123]. According to the limitation of

estimation of the band gap energy of semiconductors by the Tauc method [124], the optical properties of the films, TiN - TiN/$TiO_2$ with direct band gap and $TiO_2$ - TiN/$TiO_2$ with indirect band gap were determined using the Tauc method and equation [125] (Chapter III equation 5) then compared to the $TiO_2$ film's band gap. (see figures (V.6) and (V.7)).

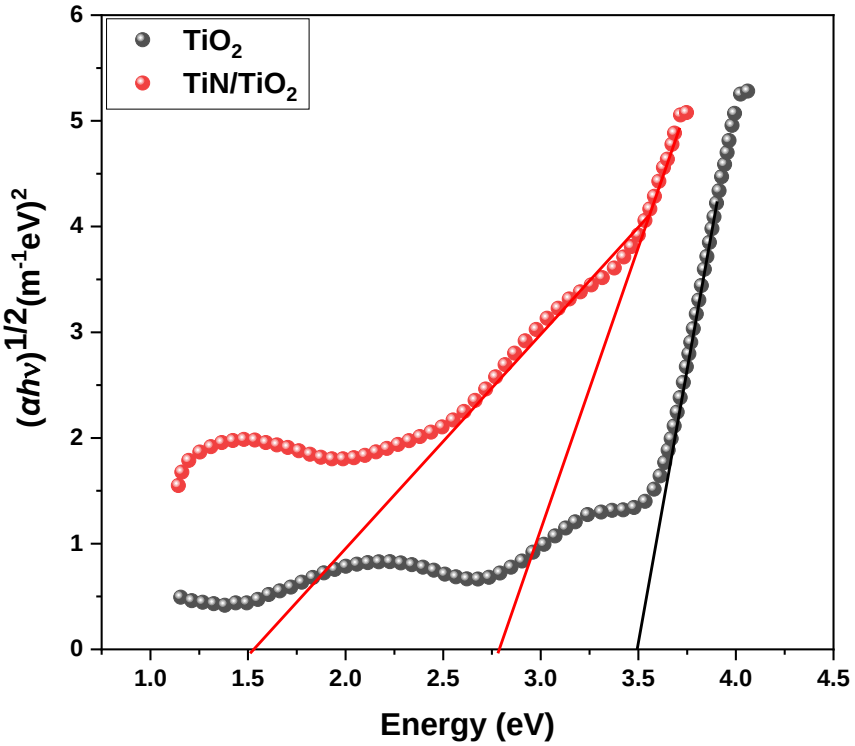


**Figure (V.6):** Tauc plot of monolayer $TiO_2$, bilayer TiN/$TiO_2$ films indirect band gaps [119].

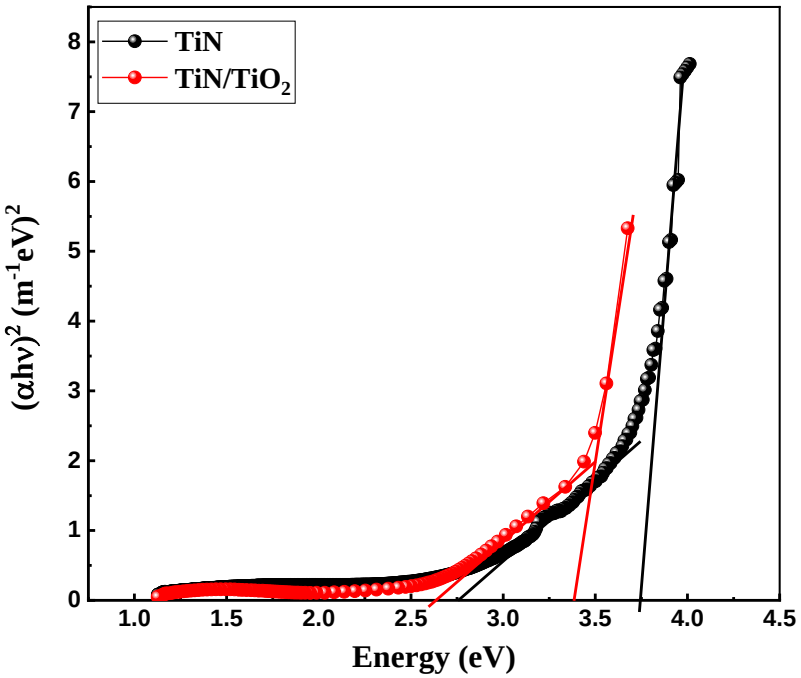


**Figure (V.7):** Tauc plot of TiN and bilayer TiN/$TiO_2$ films direct band gaps [119].

The monolayer $TiO_2$ film showed a band gap of $E_g$ = 3.45 eV, which accords with the experimental values reported in the literature for $TiO_2$ [126, 127]. The TiN film showed two band gaps, $E_{g1}$ = 3.74 eV and $E_{g2}$ = 2.73 eV, corresponding to stoichiometric TiN (see figure (V.7)). The primary distinguishing characteristic of stoichiometric TiN film is around 2.33 eV, which is associated with the electronic charge transfer between the Ti 3p and N 2s energy states. Using first-principal calculation [42], the TiN film band gap was ~2.68 eV. The observed value of $E_{g1}$ = 3.74 eV can be attributed to $TiN_x$, as found by Kavitha *et al.* [128] and Kiran *et al.*[129] for $TiN_x$ (0.4\x\0.5). The bilayer TiN/$TiO_2$ film exhibited two band gaps related to the $TiN_x$ because of the high absorption of TiN compared to $TiO_2$. The shift of these two band gap energies from $E_{g1}$ = 3.74 eV and $E_{g2}$ = 2.73 eV in the case of solo TiN film to $E_{g1}$ = 3.37 eV and $E_{g2}$ = 2.63 eV in the case of TiN/$TiO_2$ can be allocated to the annealing temperature (T=450 °C) of bilayer TiN/$TiO_2$ film which excited the N atoms to move to $TiO_2$ layer and change the stoichiometric of TiN.

The bilayer TiN/$TiO_2$ film exhibited a band gap energy lower than the $TiO_2$ film, showing energy close to $E_g$ = 2.9 eV. This reduction in the band gap energy may be due to the formation of an N-doped $TiO_2$ layer, which resulted from the interface between the TiN layer and the $TiO_2$ layer; N-doped $TiO_2$ has shown the potential to shift the absorption of $TiO_2$ from the Ultraviolet range to the visible range.

### 3.3.3. Thickness, Refractive Index *n*, and Extinction Coefficient *k*

The thickness of the TiN film was estimated using the average deposition rate of 5 nm/min determined from the cross-section images and the deposition time based on the work of Bouaouina *et al.* [130]. The deposition time was 5 minutes, resulting in a low thickness of 25 nm of the TiN film.

The envelope method was adopted to estimate the monolayer $TiO_2$ and the bilayer TiN/$TiO_2$ films' thickness along with some optical parameters [96] and equation (III.6). table (V.2) shows the obtained thickness values of the monolayer $TiO_2$, TiN and bilayer TiN/$TiO_2$ films. The estimation of the cross-section images of TiN film accords the obtained thickness of the bilayer TiN/$TiO_2$ film, since adding the thickness of TiN film to the thickness of the monolayer $TiO_2$ film approximately equals the thickness of the bilayer TiN/$TiO_2$ film.

**Table (V.2)** Estimated thickness values of monolayer $TiO_2$, TiN, and the bilayer TiN/$TiO_2$ films.

| Samples | Monolayer TiN film | $TiO_2$ film | Bilayer TiN/$TiO_2$ film |
|---|---|---|---|
| **Thickness (nm)** | **25** | **222 ±5** | **255.5 ±5** |

The variation of the refractive index (*n*) and the extinction coefficient (*k*) of the monolayer $TiO_2$ and the bilayer TiN/$TiO_2$ films were determined by using equation (III.7) [97] and equation (III.9) [98]. The results are presented in figures (V.8) and (V.9).

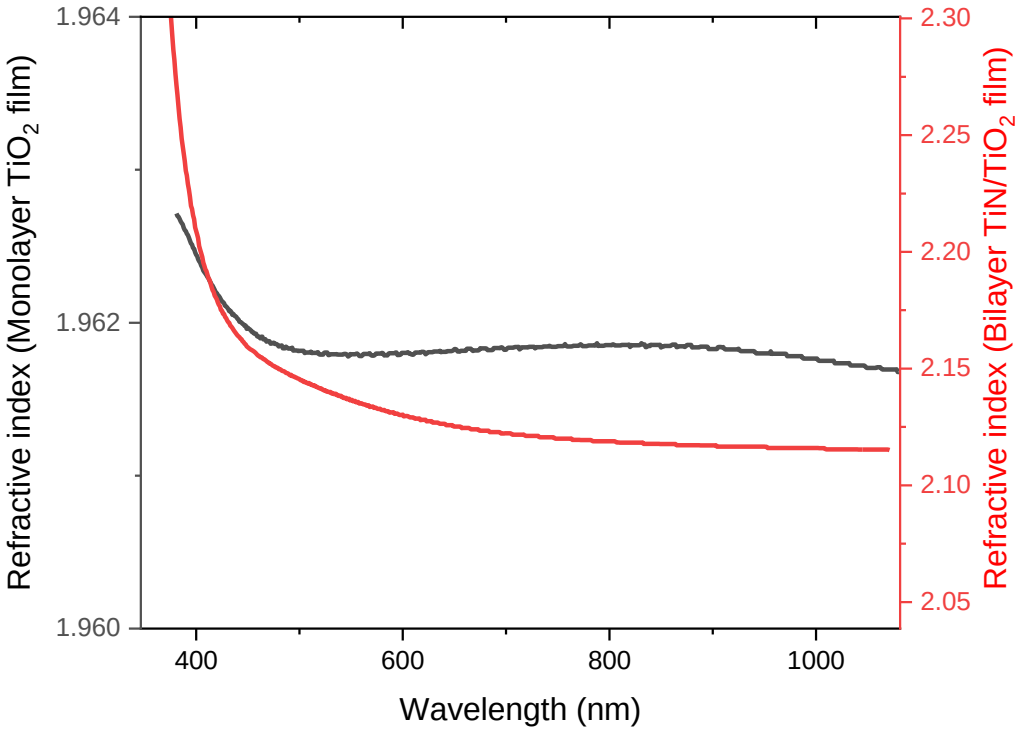


**Figure (V.8):** Variation of the refractive index (*n*) of monolayer $TiO_2$, and the bilayer $TiN/TiO_2$ films.

As can be observed, the bilayer $TiN/TiO_2$ film marks higher refractive index values than the refractive index values of monolayer $TiO_2$ films; above 800 nm, the refractive index ranges in 1.962 for monolayer $TiO_2$ film, and in 2.12 for the bilayer $TiN/TiO_2$ film.

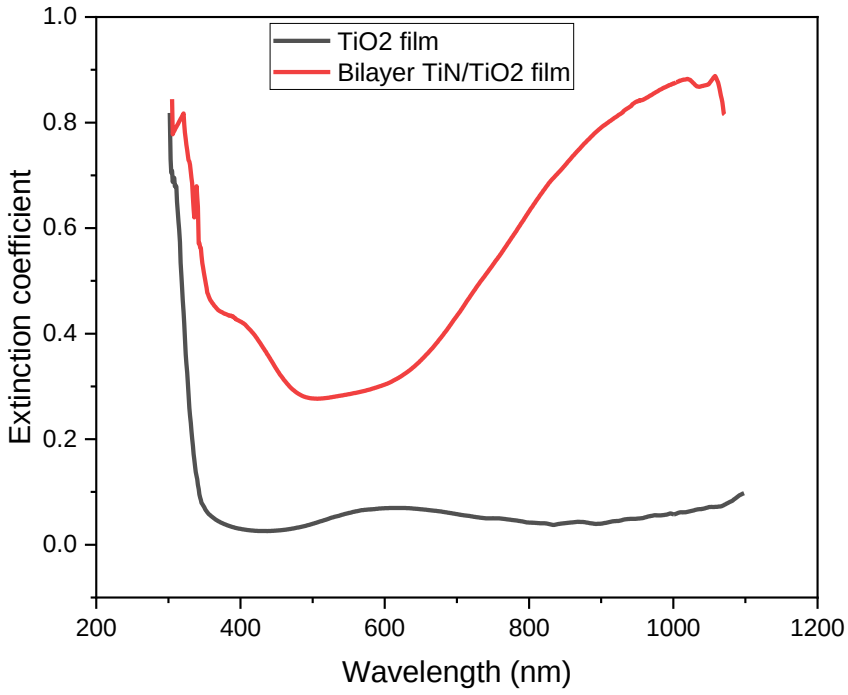


**Figure (V.9):** Variation of the extinction coefficient (*k*) of monolayer $TiO_2$, and the bilayer $TiN/TiO_2$ films.

We notice that the extinction coefficient does not exceed 0.1 in the transparency region for monolayer $TiO_2$ film, revealing its surface homogeneity. Conversely, the contrary for the bilayer $TiN/TiO_2$ film indicates its minor surface homogeneity and higher porosity.

### 3.4. Photoluminescence properties

The Photoluminescence emission spectra of the monolayer $TiO_2$ and the bilayer $TiN/TiO_2$ films are shown in figure (V.10). Photoluminescence spectra of the monolayer $TiO_2$ and bilayer $TiN/TiO_2$ films were recorded at room temperature with an excitation wavelength of 290 nm, corresponding to a photon energy of 4.27 eV, higher than the band gap energy of the investigated films, as reported elsewhere [113]. Emissions in both Ultraviolet and visible regions promote PL spectra. As shown in figure (V.10), we notice a very low intensity of the bilayer $TiN/TiO_2$ film compared to the monolayer $TiO_2$ films, which is attributed to the low transmission of the sample as shown by the transmission spectra.

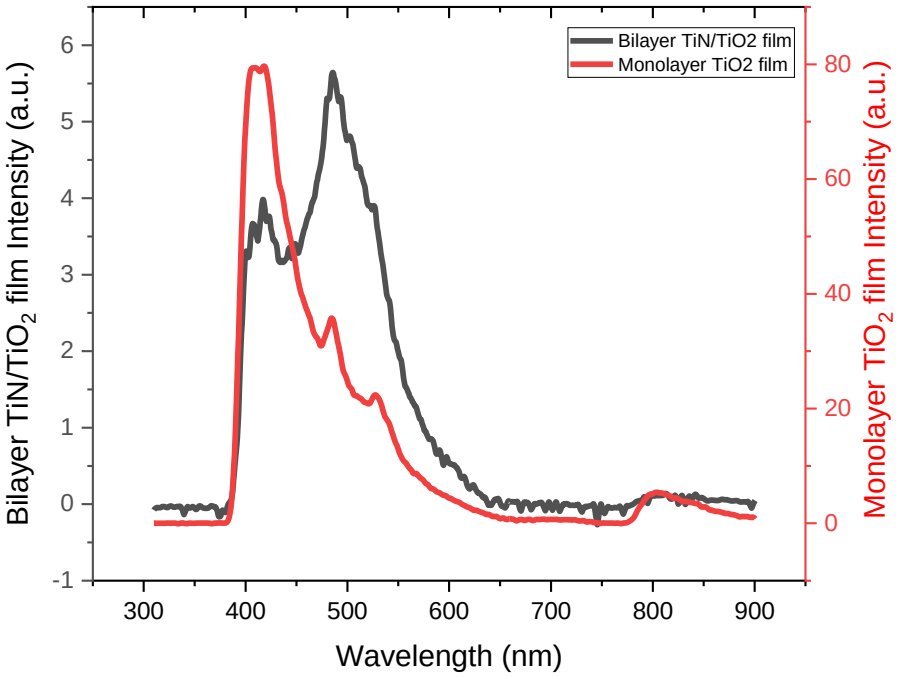


**Figure (V.10):** Photoluminescence (PL) spectra of the monolayer $TiO_2$ and the bilayer $TiN/TiO_2$ films.

As can be observed for the monolayer $TiO_2$ film, a strong PL band is detected at ~420 nm (2.95 eV), which can be attributed to the intrinsic emission of the anatase phase $TiO_2$ thin films. Another three peaks located at 484 nm (2.56 eV), 527 nm (2.37 eV), and 805 nm (1.54 eV) were also observed. These observed visible emissions are due to the intrinsic defect states within the crystal. Moreover, as for the bilayer $TiN/TiO_2$ film, a PL band is detected at ~420 nm (2.95 eV), not the higher peak like in the monolayer $TiO_2$ film, which is associated with an indirect recombination process involving defects [115]. Two higher peaks were also spotted at 484 nm (2.56 eV) and 527 nm (2.37 eV) were also seen which were caused by the intrinsic defect states within the crystal; we also noticed the disappearance of 805 nm (1.54 eV) peak when depositing $TiO_2$ layer on the TiN layer. This variation in the intensity after depositing the $TiO_2$ layer above the TiN layer is linked to a reduction in the optical band gap, and defects increase as the film's thickness increases.

### 3.5. Electrical properties

Electrical measurements using the four-probe method were conducted for the monolayer $TiO_2$ and the bilayer TiN/$TiO_2$ films. The average sheet resistivity of the samples was determined using the formula (II.6), and the results are shown in figure (V.11).

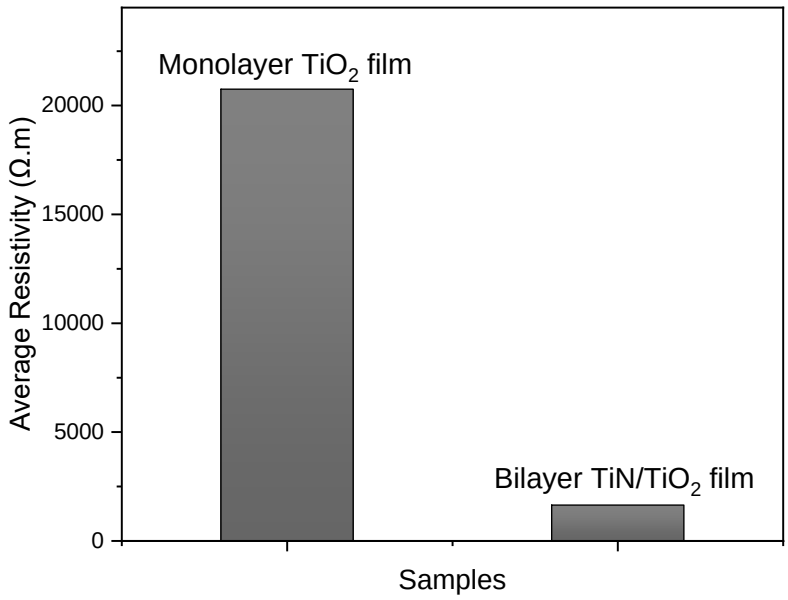


**Figure (V.11):** Average sheet resistivity of the monolayer $TiO_2$ and the bilayer TiN/$TiO_2$ films.

The average sheet resistivity of the bilayer TiN/$TiO_2$ film is much lower than that of the monolayer $TiO_2$ film. This fall of resistivity is attributed to the enhancement of the conductivity of the bilayer TiN/$TiO_2$ film due to the TiN layer and the rise of the nitrogen atom percentage in the film, contributing in the improvement of the electrical properties of the deposited film, showing the potential of coupling the TiN layer in modifying in the electrical properties.

### 3.6. Energy Dispersive X-ray Spectroscopy

Figure (V.12) shows EDX spectra for both the monolayer $TiO_2$ and the bilayer TiN/$TiO_2$ films we notice the existence of high content of Ti and O in the $TiO_2$ lattice for both samples with the existence of nitrogen content for the bilayer TiN/$TiO_2$ film sample due to the TiN layer, the high peak of Si atoms is due to the type of the substrate and the existence of C

atoms is due to the $TiO_2$ solution which was made using alcohol (contains a high percentage of carbon). The quantitative analysis and the atomic percentage of the compositional elements of the monolayer $TiO_2$ and the bilayer TiN/$TiO_2$ films indicate a suitable stoichiometry of the $TiO_2$ film and a considerable amount of nitrogen in bilayer TiN/$TiO_2$ film.

Monolayer $TiO_2$ film

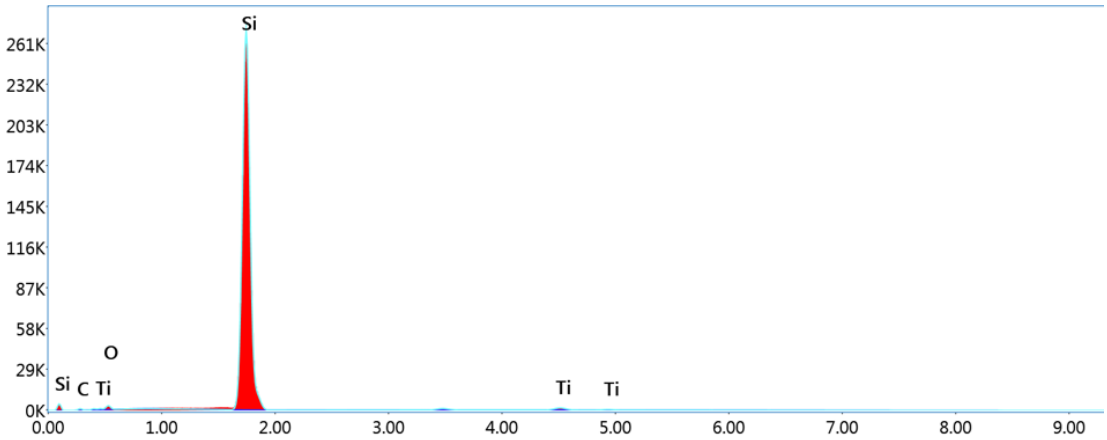


Bilayer TiN/$TiO_2$ film

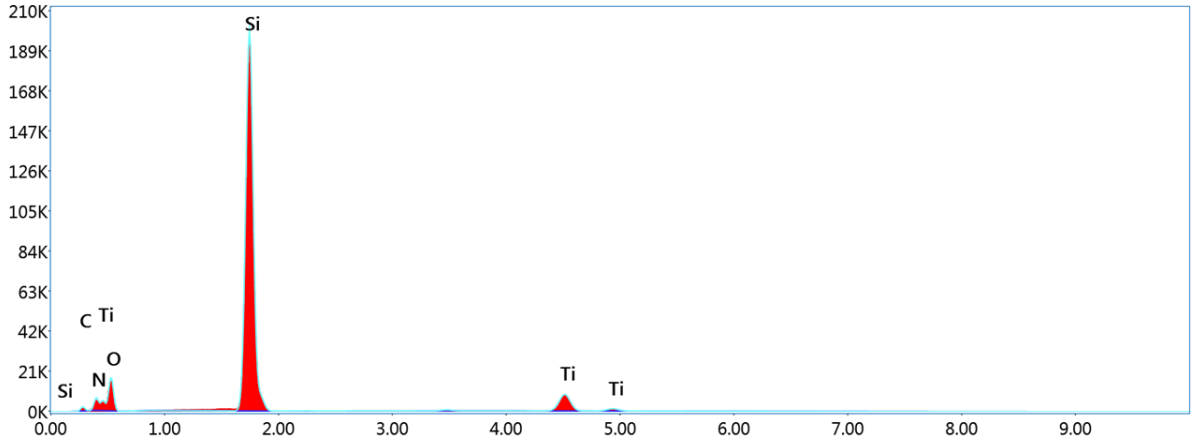


**Figure (V.12):** EDX spectrums of monolayer $TiO_2$ and bilayer TiN/$TiO_2$ films.

### 4. Photocatalytic Activity

The photocatalytic activity of the monolayer $TiO_2$ film and the bilayer TiN/$TiO_2$ film in the UV light was evaluated based on the details mentioned in Chapter III. The schematic diagram of the photocatalytic activity measurement is displayed in figure (V.13). As can be seen, the methylene blue dye solution decomposes continuously during the irradiation time for both samples. After 4 hours, the photocatalytic removal efficiency of the monolayer $TiO_2$

film reaches 51% of the initial MB dye solution concentration, and the bilayer TiN/$TiO_2$ film reaches 55% of the initial MB dye solution concentration.

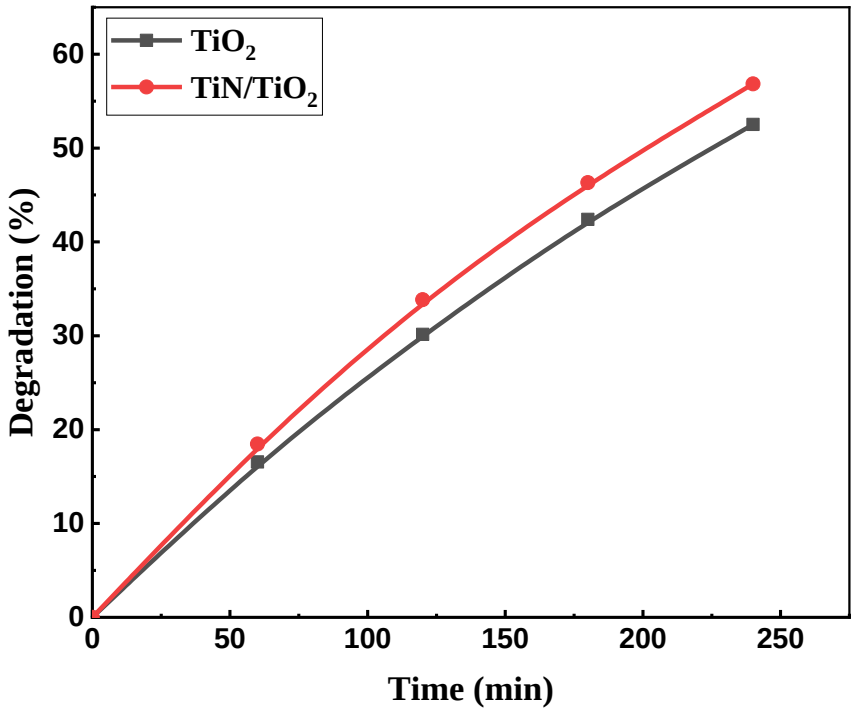


**Figure (V.13):** Degradation of Methylene blue dye as a function of the UV-light exposure time for the monolayer $TiO_2$ and the bilayer TiN/$TiO_2$ films [119].

The photocatalytic reaction rate constant ($k_{app}$) was determined by replotting the photodegradation ratio according to the following pseudo-first order reaction equation [118], as mentioned before (Chapter III).

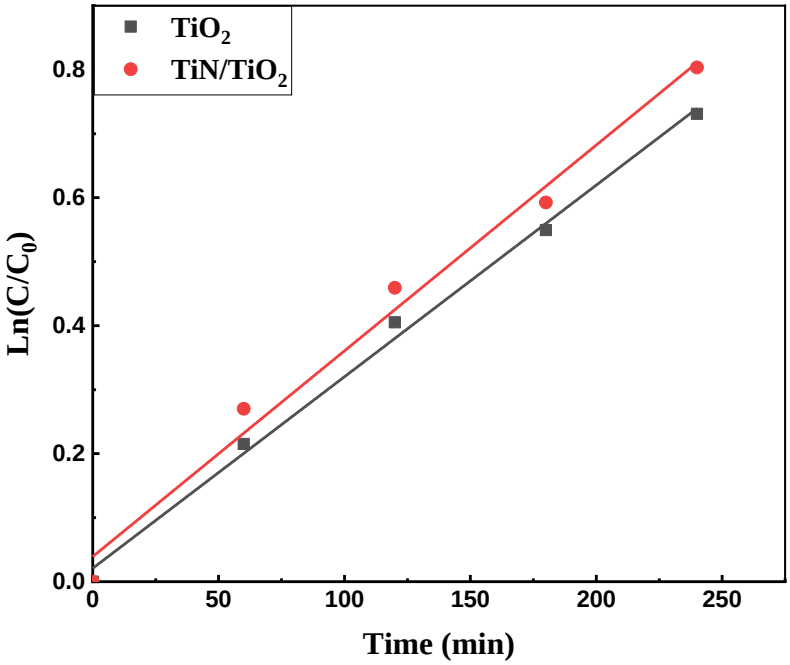


**Figure (V.14):** Plots for reaction rate constant $k_{app}$ as a function of the UV-light exposure time for the monolayer $TiO_2$ and the bilayer TiN/$TiO_2$ films [119].

As can be noticed in figure (V.14) the highest rate constant efficiency ($k_{app}$) is observed for the bilayer TiN/$TiO_2$ film ($k_{app}$ =0.00334 $min^{-1}$), which indicates more neutralization of MB dye solution compared to the monolayer $TiO_2$ film ($k_{app}$ =0.00304 $min^{-1}$) with a good correlation coefficients, $R^2 = 0.99776$ for the $TiO_2$ film, and $R^2 = 0.99356$ for the TiN/$TiO_2$ film samples. The improvement of photocatalytic degradation of MB dye solution with the bilayer TiN/$TiO_2$ film can be attributed to the modification of the surface morphology caused by the TiN oblique angle deposited as sub-layer, making this film exhibiting a height and sharp nano-clusters, which increases its specific surface area [119]. Nevertheless, the observed enhancement of MB dye solution photodegradation could be attributed to nitrogen diffusion to the $TiO_2$ film forming of the N-doped $TiO_2$ layer and oxygen vacancy defects in the interface, which induced the photocatalytic degradation [131, 132].

It should be noted that both samples in this experiment are deposited onto soda-lime glass (SLG). When performing the annealing process of the films, an amount of sodium (Na) diffuses from SLG into the $TiO_2$ layer, inducing the formation of electron-hole recombination centers, which causes a drastic decrease in the photocatalytic degradation rate of MB dye solution [133, 134]. The bilayer TiN/$TiO_2$ film interface with TiN as a sub-layer may provide

a diffusion barrier of Na atoms into the $TiO_2$ layer and contribute in the improvement of the photocatalytic degradation [119].

## 5. Conclusion

In this Chapter, a monolayer $TiO_2$ and a bilayer $TiN/TiO_2$ films were deposited by mixing two deposition techniques; the sol-gel dip-coating technique deposited the $TiO_2$ layers, and the TiN layer was deposited by the glancing angle deposition using reactive magnetron sputtering at $\alpha=45°$. Structural analysis revealed typical peaks of the $TiO_2$ anatase phase and cubic (Na-Cl type) structure of the TiN. A roughness value of 3 nm was obtained for the bilayer $TiN/TiO_2$ film with a rise and elongated grain size. It was found that the optical band gap decreases after coupling the TiN layer, which is attributed to incorporating N atoms into the $TiO_2$ structure. The hetero-interface and the surface morphology of the bilayer $TiN/TiO_2$ film contributed to the enhancement in the photocatalytic activity.

# General conclusion

In this study, we investigated the structural, optical, and photocatalytic properties of titanium dioxide ($TiO_2$) thin films doped with nitrogen atoms through three different experimental approaches:

1. Nitrogen Source Precursor Method: Nitrogen atoms were introduced during the deposition process by incorporating a nitrogen source precursor into the $TiO_2$ solution.
2. $N_2$ Plasma Treatment: The surface of the deposited $TiO_2$ films was treated with $N_2$ plasma.
3. TiN Layer Coupling: A TiN layer was coupled with the $TiO_2$ layer, allowing nitrogen atoms to diffuse from the TiN layer into the $TiO_2$ layer during thermal annealing.

Our investigation focused on the influence of these nitrogen doping methods on the physical properties of the $TiO_2$ film.

- Crystal Structure: X-ray diffraction analyses revealed that both pure and nitrogen-doped $TiO_2$ thin films crystallized exclusively in the anatase structure. Notably, no nitrogen species or related oxides were observed, which we attribute to the reactivity of nitrogen atoms.
- Optical Transparency: UV-visible analysis demonstrated that all thin films were transparent in the visible region but opaque in the UV region. This behavior was consistent across both pure and nitrogen-doped $TiO_2$ films. However, the TiN/$TiO_2$ bilayer film exhibited lower transmission due to the opaque TiN layer.
- Band Gap Energy: Calculations of the band gap energy for the $TiO_2$ thin layers indicated a decrease upon nitrogen doping in all methods, confirming successful doping.
- Surface Morphology: Atomic force microscopy (AFM) observations revealed that the surface morphology and roughness of the films were influenced by nitrogen doping.
- Photocatalytic Efficiency: The photocatalytic characteristics of the pure and nitrogen-doped $TiO_2$ thin films:

- Nitrogen Source Precursor Method: This method showed a lower yield compared to the pure $TiO_2$ samples, attributed to the use of a soda lime glass substrate, causing Na ions to diffuse into the deposited film.
- Nitrogen Plasma Surface Treatment Method: This method showed a slight improvement in photocatalytic activity compared to pure $TiO_2$ samples, attributed to the formation of nitric oxide (NO) on the surface of the $TiO_2$ film.
- TiN Layer Coupling: This method significantly enhanced the photocatalytic activity.

The obtained results highlight the potential of surface modification of $TiO_2$ layers for improved photocatalytic efficiency, particularly in addressing environmental challenges associated with increasing pollution rates.

# Perspectives

1. Investigate the effect of other nitrogen source precursors on nitrogen doping in $TiO_2$ films.
2. Explore various plasma treatment parameters (e.g., power density, treatment time, and gas flow rate) to optimize $TiO_2$ thin film properties and photocatalytic activity.
3. Study the impact of TiN film thickness and the GLAD (glancing angle deposition) angles on the physical properties and photocatalytic performance of bilayer TiN/$TiO_2$ films.

# References


[1] N. Mahato, A. Banerjee, A. Gupta, S. Omar, and K. Balani, "Progress in material selection for solid oxide fuel cell technology: A review," *Progress in Materials Science,* vol. 72, pp. 141-337, 2015.

[2] W. Li, Z. Wu, J. Wang, A. A. Elzatahry, and D. Zhao, "A perspective on mesoporous TiO2 materials," *Chemistry of materials,* vol. 26, pp. 287-298, 2014.

[3] H. Zhang, G. Chen, and D. W. Bahnemann, "Photoelectrocatalytic materials for environmental applications," *Journal of Materials Chemistry,* vol. 19, pp. 5089-5121, 2009.

[4] M. Houmard, D. Riassetto, F. Roussel, A. Bourgeois, G. Berthome, J. Joud, *et al.*, "Morphology and natural wettability properties of sol–gel derived TiO2–SiO2 composite thin films," *Applied Surface Science,* vol. 254, pp. 1405-1414, 2007.

[5] Y. Daiko, H. Yajima, and T. Kasuga, "Preparation of porous titanium phosphate glass-ceramics for NH3 gas adsorption with self-cleaning ability," *Journal of the European Ceramic Society,* vol. 28, pp. 267-270, 2008.

[6] B. Yu, K. M. Leung, Q. Guo, W. M. Lau, and J. Yang, "Synthesis of Ag–TiO2 composite nano thin film for antimicrobial application," *Nanotechnology,* vol. 22, p. 115603, 2011.

[7] A. Hagfeldt and M. Graetzel, "Light-induced redox reactions in nanocrystalline systems," *Chemical reviews,* vol. 95, pp. 49-68, 1995.

[8] K.-i. Iuchi, Y. Ohko, T. Tatsuma, and A. Fujishima, "Cathode-separated TiO2 photocatalysts applicable to a photochromic device responsive to backside illumination," *Chemistry of materials,* vol. 16, pp. 1165-1167, 2004.

[9] G. Banfi, V. Degiorgio, and D. Ricard, "Nonlinear optical properties of semiconductor nanocrystals," *Advances in Physics,* vol. 47, pp. 447-510, 1998.

[10] Y. Yan, S. R. Chaudhuri, and A. Sarkar, "Synthesis, characterizations, and optical properties of stacked porous thin films derived from sol–gel process," *Journal of the American Ceramic Society,* vol. 79, pp. 1061-1065, 1996.

[11] C. Garzella, E. Comini, E. Tempesti, C. Frigeri, and G. Sberveglieri, "TiO2 thin films by a novel sol–gel processing for gas sensor applications," *Sensors and Actuators B: Chemical,* vol. 68, pp. 189-196, 2000.

[12] O. K. Varghese, D. Gong, M. Paulose, K. G. Ong, and C. A. Grimes, "Hydrogen sensing using titania nanotubes," *Sensors and Actuators B: Chemical*, vol. 93, pp. 338-344, 2003.

[13] K. Rajeshwar, "Hydrogen generation at irradiated oxide semiconductor–solution interfaces," *Journal of Applied Electrochemistry*, vol. 37, pp. 765-787, 2007.

[14] A. Wolcott, W. A. Smith, T. R. Kuykendall, Y. Zhao, and J. Z. Zhang, "Photoelectrochemical water splitting using dense and aligned TiO2 nanorod arrays," *Small*, vol. 5, pp. 104-111, 2009.

[15] S. Z. Islam, A. Reed, D. Y. Kim, and S. E. Rankin, "N2/Ar plasma induced doping of ordered mesoporous TiO2 thin films for visible light active photocatalysis," *Microporous and Mesoporous Materials*, vol. 220, pp. 120-128, 2016.

[16] X. P. Cao, D. Li, W. H. Jing, W. H. Xing, and Y. Q. Fan, "Synthesis of visible-light responsive C, N and Ce co-doped TiO 2 mesoporous membranes via weak alkaline sol–gel process," *Journal of Materials Chemistry*, vol. 22, pp. 15309-15315, 2012.

[17] A. A. Ismail and D. W. Bahnemann, "Mesoporous titania photocatalysts: preparation, characterization and reaction mechanisms," *Journal of Materials Chemistry*, vol. 21, pp. 11686-11707, 2011.

[18] S. Bingham and W. A. Daoud, "Recent advances in making nano-sized TiO 2 visible-light active through rare-earth metal doping," *Journal of Materials Chemistry*, vol. 21, pp. 2041-2050, 2011.

[19] K. A. McDonnell, N. J. English, M. Rahman, and D. P. Dowling, "Influence of doping on the photoactive properties of magnetron-sputtered titania coatings: Experimental and theoretical study," *Physical Review B*, vol. 86, p. 115306, 2012.

[20] M. Lan, X. Peng, and W. Peinan, "Experimental study on the bandgap narrowings of $TiO_2$ films calcined under $N_2$ or $NH_3$ atmosphere," *Applied Surface Science*, vol. 255, 2008.

[21] A. Ghicov, J. M. Macak, H. Tsuchiya, J. Kunze, V. Haeublein, S. Kleber, *et al.*, "TiO2 nanotube layers: Dose effects during nitrogen doping by ion implantation," *Chemical Physics Letters*, vol. 419, pp. 426-429, 2006.

[22] A. Ghicov, J. M. Macak, H. Tsuchiya, J. Kunze, V. Haeublein, L. Frey, *et al.*, "Ion implantation and annealing for an efficient N-doping of TiO2 nanotubes," *Nano Letters*, vol. 6, pp. 1080-1082, 2006.

[23] J. Ananpattarachai, P. Kajitvichyanukul, and S. Seraphin, "Visible light absorption ability and photocatalytic oxidation activity of various interstitial N-doped TiO2

prepared from different nitrogen dopants," *Journal of hazardous materials,* vol. 168, pp. 253-261, 2009.

[24] S. Hu, F. Li, Z. Fan, and J. Gui, "Improved photocatalytic hydrogen production property over Ni/NiO/N–TiO2− x heterojunction nanocomposite prepared by NH3 plasma treatment," *Journal of Power Sources,* vol. 250, pp. 30-39, 2014.

[25] J. Barksdale, "Titanium, its occurrence, chemistry, and technology," *Soil Science,* vol. 70, p. 414, 1950.

[26] Gázquez, M.J., Bolívar, J.P., García-Tenorio García-Balmaseda, R. y Vaca, F. A review of the production cycle of titanium dioxide pigment. Scientific Research, 5 (7), 441-458, 2014.

[27] V. Augugliaro, M. Bellardita, V. Loddo, G. Palmisano, L. Palmisano, and S. Yurdakal, "Overview on oxidation mechanisms of organic compounds by TiO2 in heterogeneous photocatalysis," *Journal of Photochemistry and Photobiology C: Photochemistry Reviews,* vol. 13, pp. 224-245, 2012.

[28] S. Malato, P. Fernández-Ibáñez, M. I. Maldonado, J. Blanco, and W. Gernjak, "Decontamination and disinfection of water by solar photocatalysis: recent overview and trends," *Catalysis Today,* vol. 147, pp. 1-59, 2009.

[29] M. Kitano, M. Matsuoka, M. Ueshima, and M. Anpo, "Recent developments in titanium oxide-based photocatalysts," *Applied Catalysis A: General,* vol. 325, pp. 1-14, 2007.

[30] I. N. Martyanov and K. J. Klabunde, "Comparative study of TiO2 particles in powder form and as a thin nanostructured film on quartz," *Journal of Catalysis,* vol. 225, pp. 408-416, 2004.

[31] F. Peng, Y. Liu, H.-j. Wang, H. Yu, and J. Yang, "Synthesis and characterization of novel N-doped TiO2 photocatalyst with visible light active," *Chinese Journal of Chemical Physics,* vol. 23, pp. 437-441, 2010.

[32] C. Giolli, F. Borgioli, A. Credi, A. Di Fabio, A. Fossati, M. M. Miranda, *et al.*, "Characterization of TiO2 coatings prepared by a modified electric arc-physical vapour deposition system," *Surface and Coatings Technology,* vol. 202, pp. 13-22, 2007.

[33] I. A. Alhomoudi and G. Newaz, "Residual stresses and Raman shift relation in anatase TiO2 thin film," *Thin Solid Films,* vol. 517, pp. 4372-4378, 2009.

[34] F. Bensouici, "Caractérisation des couches minces d'oxyde de titane obtenues par le procédé sol-gel," Université M'hamed Bougara de Boumerdès, Doctoral thesis ,Département physique, 2014.

[35] M. Landmann, E. Rauls, and W. Schmidt, "The electronic structure and optical response of rutile, anatase and brookite TiO2," *Journal of physics: condensed matter,* vol. 24, p. 195503, 2012.

[36] D. A. Hanaor and C. C. Sorrell, "Review of the anatase to rutile phase transformation," *Journal of Materials science,* vol. 46, pp. 855-874, 2011.

[37] P. G. Wahlbeck and P. W. Gilles, "Reinvestigation of the phase diagram for the system titanium–oxygen," *Journal of the American Ceramic Society,* vol. 49, pp. 180-183, 1966.

[38] J. Goodenough, A. Hammett, G. Huber, F. Hulliger, M. Leiss, S. Ramasesha, *et al.*, "Landolt-Börnstein III/17g," ed: Springer Verlag, Berlin, 1984.

[39] F. Bregani, C. Casale, L. Depero, I. Natali-Sora, D. Robba, L. Sangaletti, *et al.*, "Temperature effects on the size of anatase crystallites in Mo-TiO2 and W-TiO2 powders," *Sensors and Actuators B: Chemical,* vol. 31, pp. 25-28, 1996.

[40] J. Muscat, V. Swamy, and N. M. Harrison, "First-principles calculations of the phase stability of TiO 2," *Physical Review B,* vol. 65, p. 224112, 2002.

[41] S. J. Smith, R. Stevens, S. Liu, G. Li, A. Navrotsky, J. Boerio-Goates, *et al.*, "Heat capacities and thermodynamic functions of TiO2 anatase and rutile: Analysis of phase stability," *American Mineralogist,* vol. 94, pp. 236-243, 2009.

[42] A. Fujishima and K. Honda, "Electrochemical photolysis of water at a semiconductor electrode," *nature,* vol. 238, pp. 37-38, 1972.

[43] M. Grätzel, "Photoelectrochemical cells," *nature,* vol. 414, pp. 338-344, 2001.

[44] O. Masson, R. Guinebretière, and A. Dauger, "Reflection asymmetric powder diffraction with flat-plate sample using a curved position-sensitive detector (INEL CPS 120)," *Journal of applied crystallography,* vol. 29, pp. 540-546, 1996.

[45] J. Livage, "revue verre, vol 5, n 6,«," *Les procédés sol-gel,* pp. 206-5, 2000.

[46] C. J. Brinker and G. W. Scherer, *Sol-gel science: the physics and chemistry of sol-gel processing*: Academic press, 2013.

[47] C. Sanchez and F. Ribot, "Design of hybrid organic-inorganic materials synthesized via sol-gel chemistry," *New journal of chemistry,* vol. 18, pp. 1007-1047, 1994.

[48] A. San Paulo and R. García, "High-resolution imaging of antibodies by tapping-mode atomic force microscopy: attractive and repulsive tip-sample interaction regimes," *Biophysical Journal,* vol. 78, pp. 1599-1605, 2000.

[49] I. Horcas, R. Fernández, J. Gomez-Rodriguez, J. Colchero, J. Gómez-Herrero, and A. Baro, "WSXM: A software for scanning probe microscopy and a tool for nanotechnology," *Review of scientific instruments,* vol. 78, 2007.

[50] A. V. Emeline, V. N. Kuznetsov, V. K. Rybchuk, and N. Serpone, "Visible-light-active titania photocatalysts: the case of N-doped s—properties and some fundamental issues," *International Journal of Photoenergy,* vol. 2008, 2008.

[51] A. Zaleska, "Doped-TiO2: a review," *Recent patents on engineering,* vol. 2, pp. 157-164, 2008.

[52] M. Batzill, E. H. Morales, and U. Diebold, "Surface studies of nitrogen implanted TiO2," *Chemical Physics,* vol. 339, pp. 36-43, 2007.

[53] R. Asahi, T. Morikawa, T. Ohwaki, K. Aoki, and Y. Taga, "Visible-light photocatalysis in nitrogen-doped titanium oxides," *science,* vol. 293, pp. 269-271, 2001.

[54] C. Di Valentin, G. Pacchioni, and A. Selloni, "Origin of the different photoactivity of N-doped anatase and rutile TiO 2," *Physical review B,* vol. 70, p. 085116, 2004.

[55] H. Tong, S. Ouyang, Y. Bi, N. Umezawa, M. Oshikiri, and J. Ye, "Nano-photocatalytic materials: possibilities and challenges," *Advanced materials,* vol. 24, pp. 229-251, 2012.

[56] H. Irie, Y. Watanabe, and K. Hashimoto, "Nitrogen-concentration dependence on photocatalytic activity of TiO2-x N x powders," *The Journal of Physical Chemistry B,* vol. 107, pp. 5483-5486, 2003.

[57] P. Romero-Gomez, S. Hamad, J. González, A. Barranco, J. Espinós, J. Cotrino, *et al.*, "Band gap narrowing versus formation of electronic states in the gap in N− TiO2 thin films," *The Journal of Physical Chemistry C,* vol. 114, pp. 22546-22557, 2010.

[58] H. Abdullber Fakhouri, "Thin film deposition of pure and doped TiO2 by RF magnetron sputtering for visible light photocatalytic and optoelectronic applications,",Doctoral thesis, Paris 6, 2012.

[59] T. Ihara, M. Miyoshi, Y. Iriyama, O. Matsumoto, and S. Sugihara, "Visible-light-active titanium oxide photocatalyst realized by an oxygen-deficient structure and by nitrogen doping," *Applied Catalysis B: Environmental,* vol. 42, pp. 403-409, 2003.

[60] C. Di Valentin, G. Pacchioni, A. Selloni, S. Livraghi, and E. Giamello, "Characterization of paramagnetic species in N-doped TiO2 powders by EPR spectroscopy and DFT calculations," *The Journal of Physical Chemistry B,* vol. 109, pp. 11414-11419, 2005.

[61] S. Lee, I.-S. Cho, D. K. Lee, D. W. Kim, T. H. Noh, C. H. Kwak, *et al.*, "Influence of nitrogen chemical states on photocatalytic activities of nitrogen-doped TiO2 nanoparticles under visible light," *Journal of Photochemistry and Photobiology A: Chemistry,* vol. 213, pp. 129-135, 2010.

[62] F. Dong, W. Zhao, Z. Wu, and S. Guo, "Band structure and visible light photocatalytic activity of multi-type nitrogen doped TiO2 nanoparticles prepared by thermal decomposition," *Journal of Hazardous Materials,* vol. 162, pp. 763-770, 2009.

[63] S.-H. Lee, E. Yamasue, K. N. Ishihara, and H. Okumura, "Photocatalysis and surface doping states of N-doped TiOx films prepared by reactive sputtering with dry air," *Applied Catalysis B: Environmental,* vol. 93, pp. 217-226, 2010.

[64] H. Shen, L. Mi, P. Xu, W. Shen, and P.-N. Wang, "Visible-light photocatalysis of nitrogen-doped TiO2 nanoparticulate films prepared by low-energy ion implantation," *Applied Surface Science,* vol. 253, pp. 7024-7028, 2007.

[65] C. Di Valentin, E. Finazzi, G. Pacchioni, A. Selloni, S. Livraghi, M. C. Paganini, *et al.*, "N-doped TiO2: Theory and experiment," *Chemical Physics,* vol. 339, pp. 44-56, 2007.

[66] J. Wang, D. N. Tafen, J. P. Lewis, Z. Hong, A. Manivannan, M. Zhi, *et al.*, "Origin of photocatalytic activity of nitrogen-doped TiO2 nanobelts," *Journal of the American Chemical Society,* vol. 131, pp. 12290-12297, 2009.

[67] Z. Zhang, J. B. Goodall, D. J. Morgan, S. Brown, R. J. Clark, J. C. Knowles, *et al.*, "Photocatalytic activities of N-doped nano-titanias and titanium nitride," *Journal of the European Ceramic Society,* vol. 29, pp. 2343-2353, 2009.

[68] K. Sunada, T. Watanabe, and K. Hashimoto, "Studies on photokilling of bacteria on TiO2 thin film," *Journal of Photochemistry and Photobiology A: Chemistry,* vol. 156, pp. 227-233, 2003.

[69] A. Fujishima, X. Zhang, and D. A. Tryk, "TiO2 photocatalysis and related surface phenomena," *Surface science reports,* vol. 63, pp. 515-582, 2008.

[70] A. Fujishima, T. N. Rao, and D. A. Tryk, "Titanium dioxide photocatalysis," *Journal of photochemistry and photobiology C: Photochemistry reviews*, vol. 1, pp. 1-21, 2000.

[71] N. Serpone and A. Salinaro, "Terminology, relative photonic efficiencies and quantum yields in heterogeneous photocatalysis. Part I: Suggested protocol," *Pure and Applied Chemistry*, vol. 71, pp. 303-320, 1999.

[72] S. Braslavsky and K. Houk, "Glossary of terms used in photochemistry (Recommendations 1988)," *Pure and Applied Chemistry*, vol. 60, pp. 1055-1106, 1988.

[73] J. Verhoeven, "Glossary of terms used in photochemistry (IUPAC Recommendations 1996)," *Pure and Applied Chemistry*, vol. 68, pp. 2223-2286, 1996.

[74] I. Sayah, "Etude de revêtements photocatalytiques à base de dioxyde de titane nanostructuré élaborés par pulvérisation cathodique magnétron en condition réactive," Belfort-Montbéliard, 2014.

[75] J.-M. Herrmann, "Heterogeneous photocatalysis: fundamentals and applications to the removal of various types of aqueous pollutants," *Catalysis today*, vol. 53, pp. 115-129, 1999.

[76] D. F. Ollis and H. Al-Ekabi, *Photocatalytic purification and treatment of water and air: proceedings of the 1st International Conference on TiO2 Photocatalytic Purification and Treatment of Water and Air, London, Ontario, Canada, 8-13 November, 1992*: Elsevier Science Ltd, 1993.

[77] H. Gerischer and A. Heller, "Photocatalytic oxidation of organic molecules at TiO2 particles by sunlight in aerated water," *Journal of the Electrochemical Society*, vol. 139, pp. 113-118, 1992.

[78] D. T. Sawyer and J. S. Valentine, "How super is superoxide?," *Accounts of Chemical Research*, vol. 14, pp. 393-400, 1981.

[79] F. Bensouici, M. Bououdina, A. Iratni, M. Toubane, and R. Tala-Ighil, "Effect of thickness on photocatalytic activity of TiO 2 thin films," *Progress in Clean Energy, Volume 1: Analysis and Modeling*, pp. 763-776, 2015.

[80] B. Bouaouina, "Dépôt et caractérisation des nitrures de molybdène et MoN/CrN en multicouches par pulvérisation cathodique magnétron," Université M'hamed Bougara de Boumerdès, Doctoral thesis, Département Physique, 2017.

[81] J. A. M. Meza, "Propriétés structurelles et électroniques du graphène sur SiC (0001) étudiées par microscopie combinée STM/AFM," Université Paris Sud-Paris XI; Université nationale d'ingénierie (Lima), 2013.

[82] I. Sokolov, M. E. Dokukin, and N. V. Guz, "Method for quantitative measurements of the elastic modulus of biological cells in AFM indentation experiments," *Methods,* vol. 60, pp. 202-213, 2013.

[83] A. Yahia, "Optimization of indium oxide thin films properties prepared by sol gel spin coating process for optoelectronic applications," University Mohamed Khider of Biskra, 2020.

[84] H. E. Swanson and E. Tatge, "Standard X-ray diffraction patterns," *Journal of Research of the National Bureau of Standards,* vol. 46, p. 318, 1951.

[85] B. E. Warren, *X-ray Diffraction*: Courier Corporation, 1990.

[86] D. Nunes, A. Pimentel, L. Santos, P. Barquinha, E. Fortunato, and R. Martins, "Photocatalytic TiO2 nanorod spheres and arrays compatible with flexible applications," *Catalysts,* vol. 7, p. 60, 2017.

[87] J. Yan, G. Wu, W. Dai, N. Guan, and L. Li, "Synthetic design of gold nanoparticles on anatase TiO2 {001} for enhanced visible light harvesting," *ACS Sustainable Chemistry & Engineering,* vol. 2, pp. 1940-1946, 2014.

[88] D. Georgescu, L. Baia, O. Ersen, M. Baia, and S. Simon, "Experimental assessment of the phonon confinement in TiO2 anatase nanocrystallites by Raman spectroscopy," *Journal of Raman Spectroscopy,* vol. 43, pp. 876-883, 2012.

[89] M. S. Hossain and S. Ahmed, "Synthesis of nano-crystallite gypsum and bassanite from waste Pila globosa shells: crystallographic characterization," *RSC advances,* vol. 12, pp. 25096-25105, 2022.

[90] M. Dahnoun, "Preparation and characterizationof Titanium dioxide and Zinc oxide thin films via Sol-Gel (spin coating) technique for optoelectronicapplications," University Mohamed Khider Biskra, 2020.

[91] Y. Zhao and J. Zhang, "Microstrain and grain-size analysis from diffraction peak width and graphical derivation of high-pressure thermomechanics," *Journal of applied Crystallography,* vol. 41, pp. 1095-1108, 2008.

[92] W. Wong-Ng, H. McMurdie, C. Hubbard, and A. D. Mighell, "JCPDS-ICDD research associateship (cooperative program with NBS/NIST)," *Journal of research of the National Institute of Standards and Technology,* vol. 106, p. 1013, 2001.

[93] D. Bao, X. Wu, L. Zhang, and X. Yao, "Preparation, electrical and optical properties of (Pb, Ca) TiO3 thin films using a modified sol-gel technique," *Thin Solid Films,* vol. 350, pp. 30-37, 1999.

[94] V. Etacheri, C. Di Valentin, J. Schneider, D. Bahnemann, and S. C. Pillai, "Visible-light activation of TiO2 photocatalysts: Advances in theory and experiments," *Journal of Photochemistry and Photobiology C: Photochemistry Reviews,* vol. 25, pp. 1-29, 2015.

[95] Y. Gao, Y. Masuda, Z. Peng, T. Yonezawa, and K. Koumoto, "Room temperature deposition of a TiO 2 thin film from aqueous peroxotitanate solution," *Journal of materials chemistry,* vol. 13, pp. 608-613, 2003.

[96] J. Manifacier, J. Gasiot, and J. Fillard, "A simple method for the determination of the optical constants n, k and the thickness of a weakly absorbing thin film," *Journal of Physics E: Scientific Instruments,* vol. 9, p. 1002, 1976.

[97] C. Manoharan, M. Jothibas, S. J. Jeyakumar, and S. Dhanapandian, "Structural, optical and electrical properties of Zr-doped In2O3 thin films," *Spectrochimica Acta Part A: Molecular and Biomolecular Spectroscopy,* vol. 145, pp. 47-53, 2015.

[98] N. Fellahi, M. Addou, A. Kachouane, M. El Jouad, and Z. Sofiani, "Optical properties of undoped and tin-doped nanostructured In2O3 thin films deposited by spray pyrolysis," *The European Physical Journal Applied Physics,* vol. 74, p. 24611, 2016.

[99] B. Houng, C. C. Liu, and M. T. Hung, "Structural, electrical and optical properties of molybdenum-doped TiO2 thin films," *Ceramics International,* vol. 39, pp. 3669-3676, 2013.

[100] A. Manole, M. Dobromir, M. Girtan, R. Mallet, G. Rusu, and D. Luca, "Optical properties of Nb-doped TiO2 thin films prepared by sol–gel method," *Ceramics International,* vol. 39, pp. 4771-4776, 2013.

[101] F. He and A. Becker, "Coherent control of electron localization in a dissociating hydrogen molecular ion," *Journal of Physics B: Atomic, Molecular and Optical Physics,* vol. 41, p. 074017, 2008.

[102] Y. Li, M. Ma, X. Wang, and Z. Li, "Preparation of cerium-doped titania macroporous films by a sol–gel spin coating using polypropylene glycol (PPG) as pore-creating agent: Effects of Ce ions, PPG and calcination on photocatalytic activity," *Surface and Coatings Technology,* vol. 204, pp. 1353-1358, 2010.

[103] D.-J. Won, C.-H. Wang, H.-K. Jang, and D.-J. Choi, "Effects of thermally induced anatase-to-rutile phase transition in MOCVD-grown TiO2 films on structural and optical properties," *Applied Physics A,* vol. 73, pp. 595-600, 2001.

[104] B. Avasarala and P. Haldar, "Electrochemical oxidation behavior of titanium nitride based electrocatalysts under PEM fuel cell conditions," *Electrochimica Acta,* vol. 55, pp. 9024-9034, 2010.

[105] H. Matsui, H. Tabata, N. Hasuike, H. Harima, and B. Mizobuchi, "Epitaxial growth and characteristics of N-doped anatase TiO2 films grown using a free-radical nitrogen oxide source," *Journal of applied physics,* vol. 97, 2005.

[106] F. Bensouici, M. Bououdina, A. Dakhel, T. Souier, R. Tala-Ighil, M. Toubane, *et al.*, "Al doping effect on the morphological, structural and photocatalytic properties of TiO2 thin layers," *Thin Solid Films,* vol. 616, pp. 655-661, 2016.

[107] T. Watanabe, S. Fukayama, M. Miyauchi, A. Fujishima, and K. Hashimoto, "Photocatalytic activity and photo-induced wettability conversion of TiO2 thin film prepared by sol-gel process on a soda-lime glass," *Journal of Sol-Gel Science and Technology,* vol. 19, pp. 71-76, 2000.

[108] Z. Wang, Y. Wang, W. Zhang, Z. Wang, Y. Ma, and X. Zhou, "Fabrication of TiO2 (B)/anatase heterophase junctions at high temperature via stabilizing the surface of TiO2 (B) for enhanced photocatalytic activity," *The Journal of Physical Chemistry C,* vol. 123, pp. 1779-1789, 2019.

[109] D. Nečas and P. Klapetek, "Gwyddion: an open-source software for SPM data analysis," *Open Physics,* vol. 10, pp. 181-188, 2012.

[110] N. M. Ahmed, Z. Sauli, U. Hashim, and Y. J. I. J. N. M. Al-Douri, "Investigation of the absorption coefficient, refractive index, energy band gap, and film thickness for Al0. 11Ga0. 89N, Al0. 03Ga0. 97N, and GaN by optical transmission method," vol. 2, p. e195, 2009.

[111] M. Saadati, O. Akhavan, and H. Fazli, "Single-layer MoS2-MoO3-x heterojunction nanosheets with simultaneous photoluminescence and co-photocatalytic features," *Catalysts,* vol. 11, p. 1445, 2021.

[112] T. H. Kim, G.-M. Go, H.-B. Cho, Y. Song, C.-G. Lee, and Y.-H. Choa, "A novel synthetic method for N-doped TiO2 nanoparticles through plasma-assisted electrolysis and photocatalytic activity in the visible region," *Frontiers in Chemistry,* vol. 6, p. 458, 2018.

[113] W. Naffouti, T. B. Nasr, A. Mehdi, and N. Kamoun-Turki, "Effect of sprayed solution flow rate on the physical properties of anatase TiO 2 thin films," *Journal of electronic materials*, vol. 43, pp. 4033-4040, 2014.

[114] A. Saha, A. Moya, A. Kahnt, D. Iglesias, S. Marchesan, R. Wannemacher, *et al.*, "Interfacial charge transfer in functionalized multi-walled carbon nanotube@ TiO 2 nanofibres," *Nanoscale*, vol. 9, pp. 7911-7921, 2017.

[115] Z. Bielan, S. Dudziak, A. Sulowska, D. Pelczarski, J. Ryl, and A. Zielińska-Jurek, "Preparation and characterization of defective TiO2. The effect of the reaction environment on titanium vacancies formation," *Materials*, vol. 13, p. 2763, 2020.

[116] M. Pawar, V. Nimbalkar, M. Gaonar, A. Khajone, and R. Taywade, "Effect of Nitrogen Doping on Photocatalytic Activity of TiO 2," *Journal of Nanoscience and Technology*, pp. 918-923, 2020.

[117] A. Pustovalova, E. Boytsova, D. Aubakirova, M. Bruns, S. Tverdokhlebov, and V. Pichugin, "Formation and structural features of nitrogen-doped titanium dioxide thin films grown by reactive magnetron sputtering," *Applied Surface Science*, vol. 534, p. 147572, 2020.

[118] H. S. Fogler and S. H. Fogler, *Elements of chemical reaction engineering*: Pearson Educación, 1999.

[119] L.-A. Naas, B. Bouaouina, F. Bensouici, K. Mokeddem, and S. E. Abaidia, "Effect of TiN thin films deposited by oblique angle sputter deposition on sol-gel coated TiO2 layers for photocatalytic applications," *Thin Solid Films*, vol. 793, p. 140275, 2024/03/02/ 2024.

[120] R. Swanepoel, "Determination of surface roughness and optical constants of inhomogeneous amorphous silicon films," *Journal of Physics E: Scientific Instruments*, vol. 17, p. 896, 1984.

[121] E. Shalaan, E. Ibrahim, F. Al-Marzouki, and M. J. A. P. A. Al-Dossari, "Observation of mixed types of energy gaps in some II–VI semiconductors nanostructured films: towards enhanced solar cell performance," vol. 126, pp. 1-16, 2020.

[122] F. Bensouici, M. Bououdina, A. Dakhel, R. Tala-Ighil, M. Tounane, A. Iratni, *et al.*, "Optical, structural and photocatalysis properties of Cu-doped TiO2 thin films," vol. 395, pp. 110-116, 2017.

[123] M. Solovan, V. Brus, E. Maistruk, and P. Maryanchuk, "Electrical and optical properties of TiN thin films," *Inorganic materials*, vol. 50, pp. 40-45, 2014.

[124] P. Makuła, M. Pacia, and W. Macyk, "How to correctly determine the band gap energy of modified semiconductor photocatalysts based on UV–Vis spectra," vol. 9, ed: ACS Publications, 2018, pp. 6814-6817.

[125] J. Tauc, "Optical Properties of Non-Crystalline Solids, F. Abele's edn," ed: North-Holland Publishing Co., Amsterdam, 1972.

[126] A. J. González and S. G. Santiago, "Structural and optoelectronic characterization of TiO2 films prepared using the sol–gel technique," *Semiconductor science and technology,* vol. 22, p. 709, 2007.

[127] E. Radha, D. Komaraiah, R. Sayanna, and J. Sivakumar, "Photoluminescence and photocatalytic activity of rare earth ions doped anatase TiO2 thin films," *Journal of Luminescence,* vol. 244, p. 118727, 2022.

[128] A. Kavitha, R. Kannan, P. Sreedhara Reddy, and S. J. J. o. M. S. M. i. E. Rajashabala, "The effect of annealing on the structural, optical and electrical properties of Titanium Nitride (TiN) thin films prepared by DC magnetron sputtering with supported discharge," vol. 27, pp. 10427-10434, 2016.

[129] M. Kiran, M. G. Krishna, and K. J. A. S. S. Padmanabhan, "Growth, surface morphology, optical properties and electrical resistivity of ε-TiNx ($0.4< x\leq 0.5$) films," vol. 255, pp. 1934-1941, 2008.

[130] B. Bouaouina, C. Mastail, A. Besnard, R. Mareus, F. Nita, A. Michel, *et al.*, "Nanocolumnar TiN thin film growth by oblique angle sputter-deposition: Experiments vs. simulations," *Materials & Design,* vol. 160, pp. 338-349, 2018.

[131] C. Foo, Y. Li, K. Lebedev, T. Chen, S. Day, C. Tang, *et al.*, "Characterisation of oxygen defects and nitrogen impurities in TiO2 photocatalysts using variable-temperature X-ray powder diffraction," *Nature Communications,* vol. 12, p. 661, 2021.

[132] A. K. Rumaiz, J. Woicik, E. Cockayne, H. Lin, G. H. Jaffari, and S. I. Shah, "Oxygen vacancies in N doped anatase TiO 2: Experiment and first-principles calculations," *Applied Physics Letters,* vol. 95, p. 262111, 2009.

[133] M. Benyakhlef, F. Bensouici, M. Bououdina, A. Dakhel, R. Tala-Ighil, and M. Toubane, "Surface, structural and optical properties dependence of Fe-doped TiO2 films deposited onto soda–lime–glass," *Surfaces and Interfaces,* vol. 21, p. 100682, 2020.

[134] T. Watanabe, S. Fukayama, M. Miyauchi, A. Fujishima, and K. Hashimoto, "Photocatalytic activity and photo-induced wettability conversion of TiO2 thin film

prepared by sol-gel process on a soda-lime glass," *Journal of Sol-Gel Science and Technology,* vol. 19, pp. 71-76, 2000.